8-2018

Tuning Thermal Transport in Thin Films

Yuqiang Zeng
Purdue University

TUNING THERMAL TRANSPORT IN THIN FILMS

by

Yuqiang Zeng

A Dissertation

Submitted to the Faculty of Purdue University

In Partial Fulfillment of the Requirements for the degree of

Doctor of Philosophy

School of Mechanical Engineering

West Lafayette, Indiana

August 2018

THE PURDUE UNIVERSITY GRADUATE SCHOOL
STATEMENT OF COMMITTEE APPROVAL

Dr. Amy Marconnet, Chair
School of Mechanical Engineering

Dr. Xiulin Ruan
School of Mechanical Engineering

Dr. Xianfan Xu
School of Mechanical Engineering

Dr. Ali Shakouri
School of Electrical and Computer Engineering

Approved by:

Dr. Jay P. Gore
Head of the Graduate Program

Dedicated to my parents

ACKNOWLEDGMENTS

I would first like to thank my advisor, Professor Amy Marconnet, for her wonderful guidance and support in the past five years. She always goes above and beyond my expectation for an advisor. I am very fortunate as her first PhD student. It's a valuable and memorable experience being an early member in MTEC lab. Additionally, I want to thank Profs. Xiulin Ruan, Ali Shakouri, and Xianfan Xu for serving in my dissertation committee. Thanks for their insightful and precise feedback during the course of this dissertation.

I am very grateful to my research collaborators who have made my research possible. I learned a lot from the interesting discussions with them. I would like to thank Dr. Tian Li and Prof. Liangbing Hu (RGO films); Andrea Pickel and Prof. Chris Dames (thermal conductivity measurement at high temperature); and Chun-li Lo and Prof. Zhihong Chen (2D materials). I want to thank all of my fellow group members for their support and encouragement. In particular, I would like to thank Collier Miers, Yu Han, and Zihao Zhang for their help when I built the platform for electrothermal measurements. I would like to thank Dr. Quan Yuan, Shouyuan Huang, and Yeerui Koh for their help to my research. I want to thank staff members and users at Birck for helping micro/nanofabrication. Also, I would like to thank the financial support from the Kirck fund for micro/nanofabrication.

I want to thank all my friends at Purdue outside of lab. I do appreciate the continuing friendship and support of friends at HUST. My life at Purdue would have been a lot less fun without them. Finally, I am very grateful for my girlfriend, Jiaqin Li, my sister Yuling, and my parents. I would not have had been able to finish a PhD without their encouragement and support. I look forward to spending more time with them in the future.

TABLE OF CONTENTS

LIST OF FIGURES

ABSTRACT

Author: Zeng, Yuqiang. PhD
Institution: Purdue University
Degree Received: August 2018
Title: Tuning Thermal Transport in Thin Films
Major Professor: Amy Marconnet

Decades of research have enabled new understanding of thermal transport at the nanoscale. Leveraging this new understanding to tune heat conduction in thin films (TFs) is of significant interest for both fundamental and applications. This work explores tuning thermal conduction in TFs by structuring, strain engineering, and annealing. Specifically, three approaches are interrogated: 1) nanostructuring to achieve significant in-plane thermal conduction anisotropy in TFs; 2) strain engineering of thermal conductivity (k) of a basic structure in flexible electronics, Au-on-polyimide films, and a representative 2D material, graphene; and 3) high temperature annealing of reduced graphene oxide (RGO) films to enhance k.

Nanostructuring is well known as an efficient method to modulate thermal conductivity. Extending beyond previous studies, this work investigates the directional dependence of the thermal conductivity introduced by anisotropic boundaries. Specifically, thickness modulators are introduced in TFs to structurally impact the thermal conduction anisotropy. Simulations, based on the phonon Boltzmann Transport Equation (BTE), demonstrate the ability to tune the in-plane thermal anisotropy ratio across an order of magnitude via modulating the thickness of the thin films. To predict the thermal conductivity of nanostructures, simplified Monte Carlo (MC) methods have been developed considering the expensive computational cost of solving the full BTE. We reevaluate the simplified MC methods and the applicability of these methods is evaluated.

Beyond structural engineering, this dissertation explores strain engineering of thermal conductivity in nanostructured materials including flexible TFs and 2D materials. Past experimental study on the impact of strain on thermal conductivity is very limited due to the challenges of measuring k of thin films under controlled strain. This work develops fully suspended devices on flexible substrate for strain control and evaluation of strain-dependent k using a new electrothermal measurement method. By extending conventional electrothermal approaches, the new method allows accurate thermal conductivity measurements with minimal assumptions.

Finally, this dissertation investigates annealing as an effective method to tune thermal transport in RGO films. Both the electrical and thermal conductivity increases significantly as the annealing (or reduction) temperature increases. The measured electrical and thermal conductivity are analyzed using a 3D Mott variable range hopping model and a thermal conductivity integral model, respectively. Further, the application of RGO films for high temperature thermoelectrics and extreme temperature sensing is discussed based on the measured electrical and thermal conductivity across a wide temperature range (10 K - 3000 K).

Key contributions of this dissertation include new understanding of engineering thermal conduction in TFs and characterization of thermal conductivity in strained TFs. The high in-plane thermal anisotropy ratio by nanostructuring is promising for directing heat flow in modern applications. Tuning thermal conductivity by strain control is of significant interest for modern devices with stress/strain such as flexible electronics and other devices with extreme thermomechanical stresses. For materials with an extremely high melting point, annealing at extreme temperatures by Joule heating suspended films enables additional modulation of the thermal conductivity. In summary, this dissertation enhances the understanding of tuning thermal transport with structuring, strain, and annealing through experimental and computational efforts.

1. INTRODUCTION

1.1 Overview

Experimental, theoretical, and computational efforts over the past several decades have enabled new understanding of thermal transport at nanoscale, especially in crystalline semiconductor thin films and low-dimensional materials. Lattice vibrations (phonons) are main heat carriers in these systems. Experimental results, combined with atomistic simulations, have advanced our knowledge of phonon transport. The spectral dependence and mean free path distribution of the energy carriers are critical to understand nanoscale heat conduction phenomena such as size effects, interface resistance, and ballistic transport. Nanostructuring significantly impacts the thermal conductivity due to the interaction of phonons and boundaries with length scales comparable to the phonon wavelengths and/or mean free paths. Nanowires and nanofilms generally have a significantly reduced thermal conductivity compared to the corresponding bulk materials, while extremely high thermal conductivity is observed in low-dimensional materials such as graphene and carbon nanotubes. Thermal conductivity anisotropy, specifically in terms of the in-plane k compared to cross-plane k, is observed in thin films due to the difference of the conduction paths.

In addition to progress in fundamental thermal transport, thermal property data, enabled by newly developed thermal metrology,[1,2] for materials with nanoscale features has enabled more effective thermal design and management in micro/nano-electromechanical systems (MEMS/NEMS). Numerous thermal conductivity measurement techniques have been developed including electro-, optics-, and acoustic- based methods. However, existing thermal conductivity data shows large variations partly due to unavoidable sample-to-sample variations in nanostructured samples. In addition to the sample-to-sample variations, accurate thermal metrology is challenging and comparison studies of different techniques are limited.

Despite such advances, thermal management in modern electronic devices is still challenging. Significant gaps remain between the new understanding of nanoscale thermal transport and improvement of thermal performance in electronic devices. Modern applications require unique thermal properties such as extreme thermal conductivity for heat removal and thermoelectrics and high thermal anisotropy for directing heat flow. Leveraging this new

understanding to engineer materials and obtain unique thermal properties, not naturally existing, could enable solutions to existing thermal challenges.

1.2 Organization

This work explores tuning thermal conduction in TFs by structuring, strain engineering, and annealing in three sets of studies: 1) anisotropic structuring that leads to a tunable in-plane thermal anisotropy ratio across an order of magnitude via modulating the thickness of the TFs; 2) strain engineering of thermal conductivity of a basic structure used in flexible electronics (polymer-supported metal films) and a representative 2D material (graphene); and 3) high temperature annealing which results in a significant increase in the thermal conductivity for reduced graphene oxide (RGO) films.

As a basis for the experiments in all studies, Chapter 2 develops a simple, direct differential method based on electrothermal metrology for measuring thermal conductivity of thin films by extending conventional electrothermal approaches. The new method allows accurate thermal conductivity measurements with minimal assumptions. The effectiveness of this differential measurement technique is demonstrated by measuring thermal conductivity of a 200 nm silicon layer. The accuracy of conventional electrothermal approaches for extracting thermal conductivity is investigated by comparing to this new method. Further, a thermo-mechanical metrology platform is developed for studying strain dependent thermal transport taking advantage of strain control through flexible substrate. This metrology platform enables strain-dependent thermal characterization of micro/nanostructures.

Past research proves nanostructuring as an efficient method to modulate thermal conductivity, but little work has looked at inducing anisotropy within the in plane directions of thin films. Chapter 3 investigates the directional dependence of thermal conductivity introduced by anisotropic boundaries. Specifically, thickness modulators are introduced in TFs to structurally impact the thermal conduction anisotropy. Simulations based on the phonon Boltzmann Transport Equation demonstrate a tunable in-plane thermal anisotropy ratio across an order of magnitude via modulating the thickness of the thin films. Moreover, the proposed structure is experimentally feasible and is promising for directing the heat flow pathways in modern applications including thermal management of electronic devices. For predicting thermal conductivity of nanostructures, simplified Monte Carlo methods have been developed as solving the full BTE is computationally

expensive. Chapter 4 reevaluates two main types of simplified Monte Carlo methods, and the applicability of these methods is evaluated.

Beyond structural engineering, chapter 5 explores strain engineering of the thermal conductivity of polymer-supported metal films and multi-layer graphene films. Suspended samples on a flexible substrate combined with a custom-built mechanical stage enables strain dependent thermal conductivity characterization using the electrothermal method. Characterization of the strain-dependent thermal conductivity of materials enables us to probe the underlying thermal transport physics. Additionally, understanding thermal transport in strained micro/nanostructured materials is critical for applications related to flexible electronics and other devices with significant thermomechanical stresses.

Chapter 6 investigates annealing as an effective method to tune thermal transport in RGO films. A unique two-step annealing process is applied to reduce the graphene oxide films. A considerable increase of electrical and thermal conductivity is observed for RGO films as the reduction temperature increases. The measured electrical and thermal conductivity are analyzed with a 3D Mott variable range hopping model and a thermal conductivity integral model, respectively. Further, the application of RGO films for high temperature thermoelectrics and extreme temperature sensing is discussed.

Chapter 7 summarizes the dissertation work and suggests future work extending from this dissertation.

2. THERMAL CONDUCTIVITY MEASUREMENT METHODOLOGY[1]

2.1 Background

Nanostructured materials have attracted broad interest in last two decades due to their unique properties not naturally available in bulk materials. For example, past work shows the extension of both the upper and lower limits of thermal conductivity (k) by introducing nanostructures: nanoporous silicon exhibits extremely low thermal conductivity,[3–6] while thermal conductivity of graphene and carbon nanotube is surprisingly high.[7,8] Measurements of thermal conductivity at the micro/nanoscale are challenging in part due to the lack of a standard "four-probe" method for thermal metrology, which is readily available for electrical conductivity measurements. Numerous methods for measuring thermal conductivity have been developed including suspended electrothermal methods, thermoreflectance techniques, Raman spectroscopy, and other new measurement techniques.[9–14]

Despite the immense progress in thermal metrology in micro/nanoscale over the past decades, accurate thermal measurements are still challenging. Existing thermal conductivity data for nanostructured samples shows large variations, but it is not yet clear whether variations are solely due to sample-to-sample variations or discrepancies between measurement techniques.[2,15] A widely investigated example is silicon thin films (TFs).[16–20] The standard silicon-on-insulator (SOI) technology provides a high quality, ultrathin silicon device layer. Therefore, sample-to-sample variations are typically expected to be negligible in silicon TFs, but large variations in existing thickness-dependent thermal conductivity data still exist.[2]

In addition to the variation from sample-to-sample, uncertainty from the measurement techniques needs to be considered. As an example, in a conventional nano/microscale electrothermal thermal measurement technique,[5,21] referred to here as the *composite beam method*, a long, suspended, rectangular sample (*e.g.* a strip of thin film silicon) is coated with a dielectric layer (for electrical insulation) and a metal layer that serves as both the heater and thermometer for the measurement. Joule heating in the composite beam elevates the temperature increasing the electrical resistance. Fitting the electrothermal response (*i.e.* the change in resistance

[1] This section reproduced with permission from Y. Zeng and A. Marconnet, Rev. Sci. Instrum. **88**, 44901 (2017). Copyright 2017 American Institute of Physics

with increased current) to the solution extracted from the heat diffusion equation yields the thermal conductance of the composite beam structure. The thermal conductivity, *k*, of the sample film can be extracted from the measured conductance if the thermal conductivities of the dielectric and metal layers are estimated or known from measurement of a reference sample consisting of the metal and dielectric alone. However, several sources of error arise from the interfacial effects and the parallel heat conduction pathways. Furthermore, in the widely used *suspended heater-thermometer measurement technique* first developed by Shi and colleague[9], a sample is suspended between two platforms that serve as heaters and thermometers to quantify thermal conductivity. Although this requires more extensive fabrication, the sample itself is fully suspended and does not require any coating of dielectric or metal layers. In addition to typical assumptions about contact resistances between the sample and the platforms and neglecting radiation heat losses, the thermal conductances of the support beams are typically assumed to be identical. One method to indirectly verify this assumption is to measure *k* twice: first using one of the suspended platforms as the heater and the other as the sensor, and then to reverse the orientation of the heat flow. The variation in the measured *k* in these two measurements demonstrates the nonuniformity of these two suspended platforms.[22] Even more importantly, in general, there is no way to quantify these nonuniformities and their impact on the thermal measurement *a priori*. Finally, a set of techniques involving free-standing membranes combined with contactless *optothermal thermal conductivity measurement methods* are promising to avoid the issue encountered in electrothermal methods. Recent optothermal measurements of free standing silicon thin films from Chávez *et al.*[23] and Cuffe *et al.*[24] provide new thermal conductivity data across a large range of thicknesses (from ~10 nm to ~1 micron), without the presence of any additional metal or dielectric films avoiding any impact of interfaces and parallel heat conduction pathways. But the variation in the measured data still exceeds the expected uncertainty of the measurement techniques.

2.2 The Direct Differential Electrothermal Measurement Approach

Here, we develop and validate a simple direct differential electrothermal measurement of thermal conductivity for suspended thin films. Specifically, to extract thermal conductivity of the sample, we develop a cross-beam structure similar to the T-type measurements previously used for fibers and nanotubes,[25,26] in which the bare sample extends at a right angle from the center

of a composite heating beam (see Figure 2.1 (b)). A two-step measurement, first of the cross-beam structure, then of the cross-beam structure with the sample removed by Focused Ion Beam (FIB) (see Figure 2.1 (c)), enables extraction of the sample thermal conductivity from a single sample. Removing the sample beam from the heater beam in the cross-beam structure via FIB makes this second measurement identical to the composite beam approach described above. This composite heater beam can be directly measured as a whole to determine an effective thermal conductance of the silicon plus coating layers, and the sample itself is free of any coating layers for direct measurement of the sample thermal conductivity. There is no need to assume fabrication uniformity or neglect interfacial effects for the sample in the new method. In addition to validating the new measurement technique, we use the data to interrogate assumptions applied for two conventional methods. Specifically, we (i) extract the sample thermal conductivity from the composite beam measurement alone to evaluate the assumption of negligible interfacial effects and assumed material properties, and (ii) extract the sample thermal conductivity from the cross-beam measurement approach assuming the thermal conductance of the independent composite heater beam is the same as that of the heater in the cross-beam configuration since they are fabricated simultaneously. This second approach allows evaluation of the impact of assumed fabrication uniformity applied in previous electrothermal methods.[10,15,19] The effectiveness of the direct differential method is validated by measuring k of 200 nm silicon TF. Finally, we compare the measured thermal conductivity with previous literature results and with a kinetic theory model for thermal conductivity.

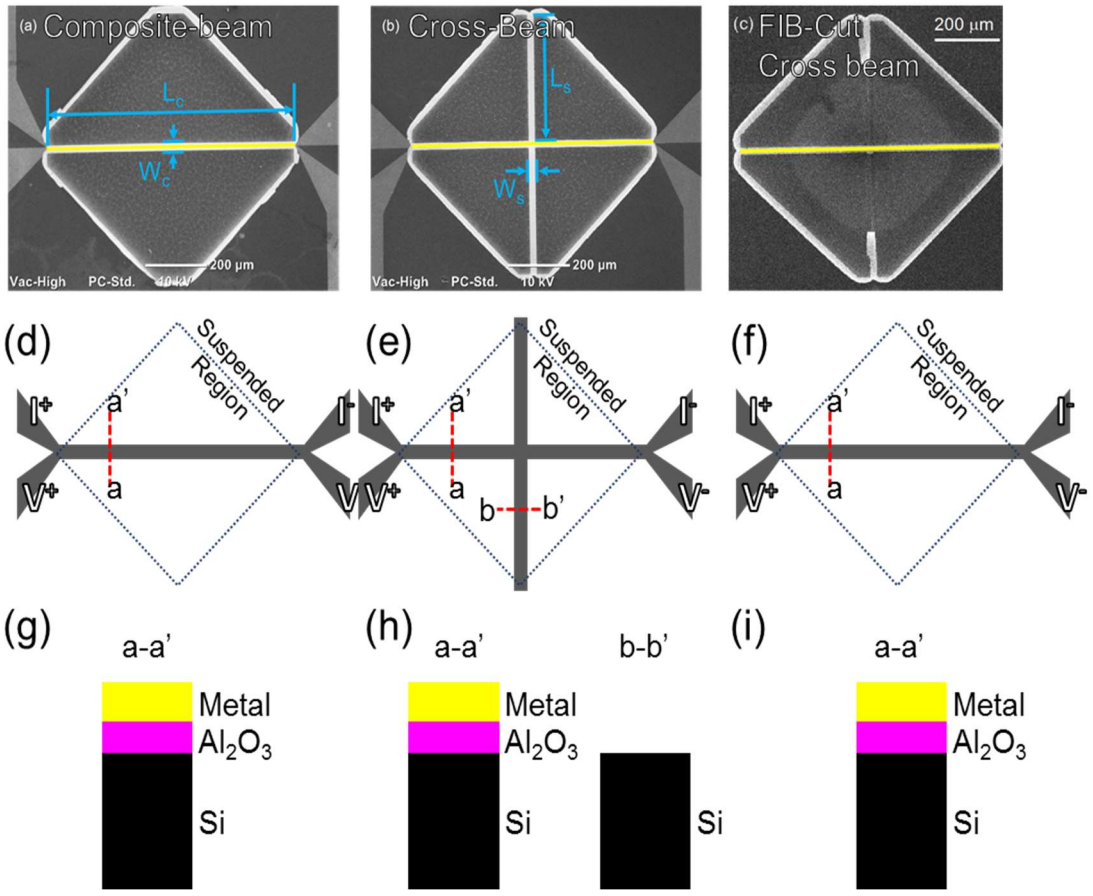

Figure 2.1: Top-view (a-c) SEMs and (d-f) schematics of the three measurement devices, as well as (g-i) cross-sections of the suspended beams in each measurement device. Each sample is configured with a standard four-probe electrical measurement configuration for the heater beam. The composite heater beam region in each of the suspended structures is false colored yellow in the SEM images. The diamond shape in each SEM indicates the edge of the suspended region. (a,d,g) The composite-beam structure of width W_c and length L_c consists of a single silicon beam coated with dielectric and metal layers. (b,e,h) The cross-beam structure has two additional sample beams of width W_s and length L_s extending at right angles from the center of the composite heater beam. These cross-beam samples have no additional layers of Al_2O_3 or metal as shown in the cross-section schematic. (c,f,i) The cross-beam structure after the sample beam is detached using FIB has a structure identical to the composite beam sample. The detached sample beam curls up at the top and bottom of the suspended region due to the unbalanced strain after the cut. In each SEM, the scale bar is 200 µm.

2.2.1 Sample Fabrication

Starting from a silicon-on-insulator (SOI) wafer, a standard lift-off process is used to define four-probe electrodes of 50 nm Cr/Pt (for the heater/thermometer) with 50 nm aluminum oxide (as an electrically insulating layer between the silicon and the metal). Then, the composite and cross beam structures are patterned by photolithography, and the Si and SiO_2 layers are etched away by

Reactive Ion Etching using SF_6 and CF_4, respectively. After removing photoresist (PR), a conformal parylene layer is coated on the wafer to protect the front side in the following release step. A release window is defined by photolithography and the pattern is transferred to the parylene layer via oxygen plasma. XeF_2 gas is then used to isotropically etch the Si substrate (suspending the measurement structures) and then the buried oxide layer is removed using a wet buffered HF etch. Finally, any remaining PR and parylene is etched away using oxygen plasma. For the direct differential electrothermal measurement, the sample beams in the cross-beam structures are detached using FIB after the initial electrothermal measurement. SEM pictures of fabricated composite-beam structure and cross-beam structure before and after the cut are shown in Figure 2.1 (a-c).

Note that for other potential sample films deposited on Si substrates with high etch selectivity over Si, the fabrication process can be greatly simplified. Devices can simply be released using XeF_2 etch after the composite and cross beam definition.

2.2.2 Measurement

2.2.2.1 Composite Beam Structure

First, consider Joule heating in the composite beam structure (a rectangular thin film sample, coated with a dielectric insulating layer and metal heater/thermometer layer). Current I flow through the metal layer generates heat which conducts to the ends of the beam, which are connected to the substrate that acts as a heat sink maintained at temperature T_o. The governing equation for one-dimensional heat conduction in this composite-beam structure and the relevant boundary conditions are given by

$$G_c \frac{d^2T}{dy^2} + \frac{I^2 R(T)}{L_c} = 0 \tag{2.1}$$

$$T(y = \pm L_c / 2) = T_0 \tag{2.2}$$

where k_c, A_c, L_c, and $G_c = k_c A_c$ are the effective thermal conductivity, total cross-section area, length, and thermal conductance of the composite beam, respectively. The temperature coefficient of resistance, α_m, is assumed to be constant in the temperature range of interest (40K – 320K) such that the resistance is given by

$$R(T) = R(T_0)\left[1 + \alpha_m (T - T_0)\right] \tag{2.3}$$

where $R(T_0)$ is the resistance at a reference temperature T_0. The analytical solution to the temperature profile can be determined:

$$T = T_0 + \frac{1}{\alpha_m}\left[\frac{\cos(I\gamma_c y)}{\cos(I\gamma_c L_c/2)} - 1\right] \tag{2.4}$$

where $\gamma_c^2 = \alpha_m R(T_0)/G_c L_c$. Then, the electrical resistance of the composite beam for a given applied current can be determined from

$$\overline{R} = R(T_0)\left[\tan(I\gamma_c L_c/2)/(I\gamma_c L_c/2)\right] \tag{2.5}$$

Thus, γ_c, which is directly related to the effective composite beam thermal conductance G_c, can be extracted by fitting experimental data for the increase in resistivity with applied current, provided that α_m is determined using electrical resistance measured with low applied current. Geometrical dimensions are measured with a series of SEMs after the electrothermal measurement. All samples are configured with four-probe electrical connections to measure the average resistance of the sample as a function of applied heater current.

2.2.2.2 Cross-Beam Structure

Now, extending to the cross-beam structure, the heater beam and associated governing equation is identical to the composite beam case (Eq. (2.1)), but heat generated in the composite beam can also be dissipated through the sample located at the center of the composite beam. With the 1D approximation, the boundary condition at the center of the heater beam (y=0) becomes an energy balance

$$G_c \left.\frac{\partial T}{\partial y}\right|_{y=0} = \frac{G_s}{L_s}(T(y=0) - T_0) \tag{2.6}$$

where L_s, k_s, A_s, and $G_s = k_s A_s$ are the length, thermal conductivity, cross-sectional area, thermal conductance of the sample film, respectively. The temperature profile in the heater beam is very sensitive to the thermal conductance of the sample beam as shown in Figure 2.2 (a), which allows accurate extraction of the thermal conductivity in sample beams in the measurement. With the 1D approximation, the electrical resistance of the cross-beam for a given applied current can be determined from

$$\overline{R} = R(T_0)\frac{\frac{2L_s}{L_c}\sin(I\gamma_c L_c/2)+\frac{4G_s}{I\gamma_c G_c L_c}(1-\cos(I\gamma_c L_c/2))}{I\gamma_c L_s\cos(I\gamma_c L_c/2)+\frac{G_s}{G_c}\sin(I\gamma_c L_c/2)} \tag{2.7}$$

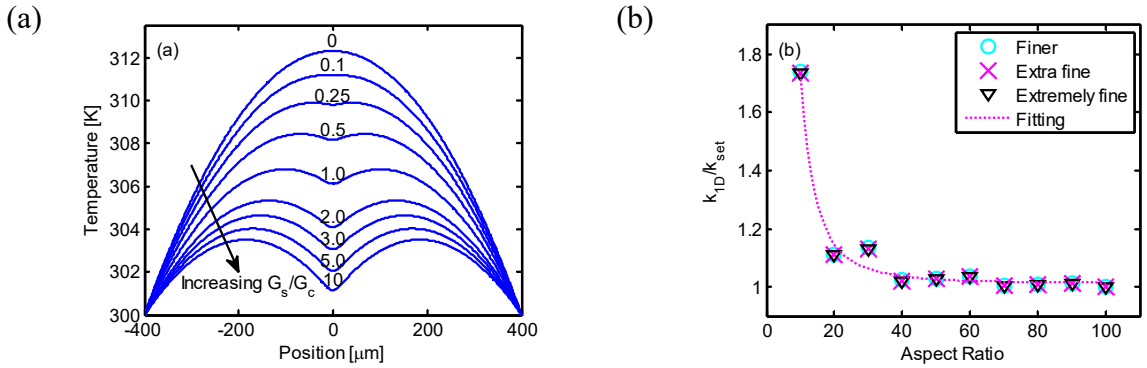

Figure 2.2: (a) Temperature profile in the heater beam as a function of the ratio of the sample thermal conductance to the heater beam thermal conductance. Note that for increasing sample thermal conductance, the centerline temperature and the average temperature decrease. (b) Ratio of thermal conductivity extracted using 1D model (k_{1D}) to the input value of thermal conductivity (k_{set}) used in the 3D COMSOL model varying the aspect ratio of the heater beam. Note that as the aspect ratio increases, the extracted thermal conductivity k_{1D} approaches the input value. Above an aspect ratio of 40, the error is less than 2.5%. A convergence test of the 3D model is completed by increasing the number of mesh elements. Three pre-defined COMSOL mesh options are evaluated (finer, extra fine, and extremely fine, which correspond to 10014, 53513, and 122336 mesh elements for an aspect ratio of 100, respectively) and no significant variation in the result with varying mesh sizes verifies the convergence of the numerical simulation.

Note that the sample beam does not have any metal or dielectric layers, thus the effective conductivity of the composite beam and the conductivity of the sample beam may not be identical.

A full three-dimensional (3D) COMSOL model verifies accuracy of applying the one-dimensional (1D) model to extract the sample thermal conductivity as a function of the aspect ratio (AR) of the heater beam (AR = L_c/W_c) for a sample conductivity of 100 W/(m K). Note that in this work the sample and heater beams have the same width and the length of the heater beam is twice the length of each sample beam (see Figure 2.1). As shown in Figure 2.2 (b), results extracted using 1D model are within 2.5% of the input value of thermal conductivity if the aspect ratio is greater than 40.

2.2.3 Experimental Configuration

To extract thermal conductivity, a four-probe I-V sweep is performed with the applied heater current between -348 μA and +348 μA (in which the average temperature rise within the sample does not exceed ~10 K such that radiation losses are negligible). Joule heating in the beam increases the temperature of the metal film corresponding to an increase in the measured electrical resistance with increasing applied current as shown in below At each current level, the voltage acquisition starts 10 seconds after the current is applied, which is sufficient to ensure the steady state, and five measurements are recorded at 2-second intervals to confirm that steady state has been achieved. In practice, I-V sweeps can be performed simultaneously in several composite and cross beam structures. After the measurement of the cross-beam structure, the sample beams are detached using FIB. Then, another I-V sweep is applied for the modified structure. With the two-step measurement of the cross-beam structure, we are able to extract the sample thermal conductivity using the direct differential method. In addition, the sample thermal conductivity can be estimated from the complete cross-beam measurement without the FIB cut when assumptions about material properties are introduced (see Section III.D.).

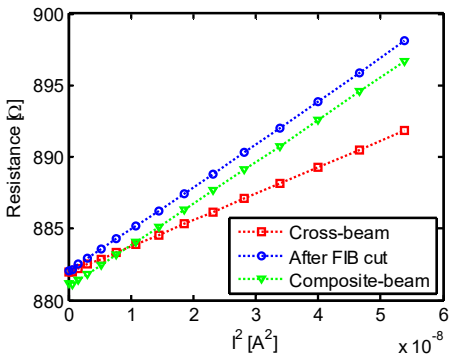

Figure 2.3: Measured increase in electrical resistance as a function of the square of the current for a cross-beam structure before (red squares) and after (blue circles) the FIB cut compared to that of a composite-beam structure (green triangles). For the cross-beam measurements, the change in the slope of this curve after the FIB cut is due to the removal of the sample beams and the corresponding increase in the thermal resistance of the structure. The variation in the fitted resistance at zero current, R0, between the composite- and cross-beam structures is due, in part, to fabrication nonuniformity.

Here, the temperature is varied from 40 K to 320 K in ~10 K increments. All electrothermal measurements (*i.e.* the I-V sweeps) are performed in a Janis CCS - 150 cryostat with vacuum levels on the order of 1×10^{-4} Torr. The sample temperature is controlled and measured using a Lakeshore

model 325 temperature controller. It generally takes 25 - 30 minutes for the system to stabilize at each temperature. To ensure accurate temperature-dependent measurement, two temperature sensors, one on the cold finger and one on the sample stage, are used for control and measurement accuracy.[27] Two sensors are needed in order to perform accurate electrothermal measurements as the temperature coefficient of resistivity plays a key role in extracting thermal conductivity data. Deviations in the temperature readings between two sensors across the temperature range are always less than 1 K, as shown in Figure 2.4.

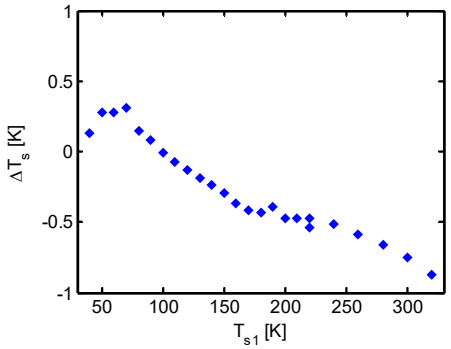

Figure 2.4: Deviation in the measured temperatures between two sensors. The varying deviation implies the associated measurement error when only one sensor is used for temperature control and measurement.

The electrical conductivity and the temperature coefficient of resistance are determined from the resistance measured at low current, where Joule heating is negligible. The electrical conductivity of the metal layer is calculated from the measured electrical resistance and geometrical dimensions measured using SEMs. From the electrical data, the thermal conductivity of the metal layer is estimated using Wiedemann-Franz law: $k_m = L\sigma T$, where L is the Lorenz number and σ is the electrical conductivity. Thus, the thermal conductance of the metal layer is $G_m(T) = LL_cT/R(T)$, where L_c is the length of the composite beam. The temperature coefficient of resistance is obtained by fitting Eq. (2.3) to the low-current experimental data. Considering the slight non-linearity of measured *R(T)*, an estimate of the uncertainty in α is determined by fitting low-current electrical resistances around each reference temperature. That is, we calculate the temperature coefficient of resistance using electrical resistances at each sample temperature in three ways: (i) considering data points within ±10°C of the measurement temperature, (ii) considering the data points between the measurement temperature T_0 and T_0+20°C, and (iii)

considering just the data points T_0 -20°C and T_0. From these three values, the range of uncertainty in the temperature coefficient of resistance α is determined to be on the order of 1%.

2.2.4 Extracting Thermal Conductivity

With the cross-beam measurements before and after the FIB cut, we extract the sample thermal conductivity using the direct differential method. In addition, the sample thermal conductivity can be determined from one-step measurement of the composite and cross beam structures when conventional assumptions are introduced. The composite beam measurements require assumed properties of the metal and dielectric layers and neglecting any interfacial effects. Evaluating the thermal conductivity of the cross-beam measurement without a FIB cut of the sample requires measurement of a composite heater beam fabricated simultaneously in the same process, and the assumption that the thermal conductance is identical to the heater beam in the cross-beam structure. By comparing the data to that measured with the direct differential method (*i.e.* the cross-beam before and after the FIB cut of the sample), the validity of these assumptions can be evaluated as no such assumptions are required in the developed new method. Thus, in this work, the direct differential method is developed to extract the intrinsic thermal conductivity of the silicon sample film and investigate the validity of these conventional assumptions. Three sets of data are presented here: (i) k_{s1} is the silicon thermal conductivity extracted from the composite beam measurement alone assuming metal and dielectric thermal conductivity and neglecting any interfacial effects; (ii) k_{s2} is the silicon thermal conductivity from the cross beam measurement assuming the thermal conductance from a simultaneously fabricated composite beam; and (iii) k_{s3} is the silicon thermal conductivity from the direct differential cross beam measurement using the thermal conductance of the heater beam of the cross-beam structure itself (*i.e.* after the FIB cut). Note that k_{s3} is extracted from the direct differential measurement, while several assumptions are introduced to determine k_{s1} and k_{s2}.

First, the silicon conductivity is extracted from the composite beam structure alone. From the measured thermal conductance G_{c1}, the thermal conductivity of the sample layer (k_{S1}) can be obtained if we assume negligible interfacial effects and estimate the thermal conductivity of the metal and dielectric layers:

$$G_c = k_s A_s + k_m A_m + k_d A_d \tag{2.8}$$

where k_m and k_d are the thermal conductivity of the metal and dielectric layers, and A_m, and A_d are the cross-sectional areas of the metal and dielectric layers, respectively. Here, the thermal conductivity of the dielectric layer is taken from literature,[28] while that of the metal layer is estimated based on Wiedemann–Franz law. Generally, this method is most accurate when conduction in the sample layer dominates over conduction in the metal and dielectric layers.

In the second approach, we extract the silicon thermal conductivity (k_{s2}) from the cross beam measurement using the thermal conductance from the composite beam measurement. Here, we assume that, since the composite-beam and cross-beam structures are fabricated in the same run and from the same SOI wafer with the same masks and dimensions, the composite beam thermal conductance will match that of the heater beam in the cross-beam structure. Although the thermal conductivity can be extracted in this way, the accuracy of this method relies greatly on the fabrication uniformity. Variations in thickness across the wafer and uniformity of post-fabricated dimensions critically impact the results.

Finally, the silicon thermal conductivity (k_{S3}) is determined from the developed direct differential method eliminating the need to make assumptions about fabrication uniformity, interfacial effects, or estimated material properties. After the initial electrothermal measurement, we cut the sample beams from the cross-beam structure using FIB, leaving a structure nearly identical to the original composite beam structure as shown in Figure 2.1 (c). An example plot of I^2 vs. R in the cross-beam structure before and after the cut is shown in Figure 2.3. Using the same approach as described for the original composite beam, we directly measure the thermal conductance of the heater beam (G_{c2}). Thus, the thermal conductivity of the sample beams can be extracted using this thermal conductance G_{c2}, which has the fewest assumptions in the analysis. Further, there is no need to consider interfacial effects as thermal conductance of the composite beam is measured as a whole and the sample itself is free of any coating layers.

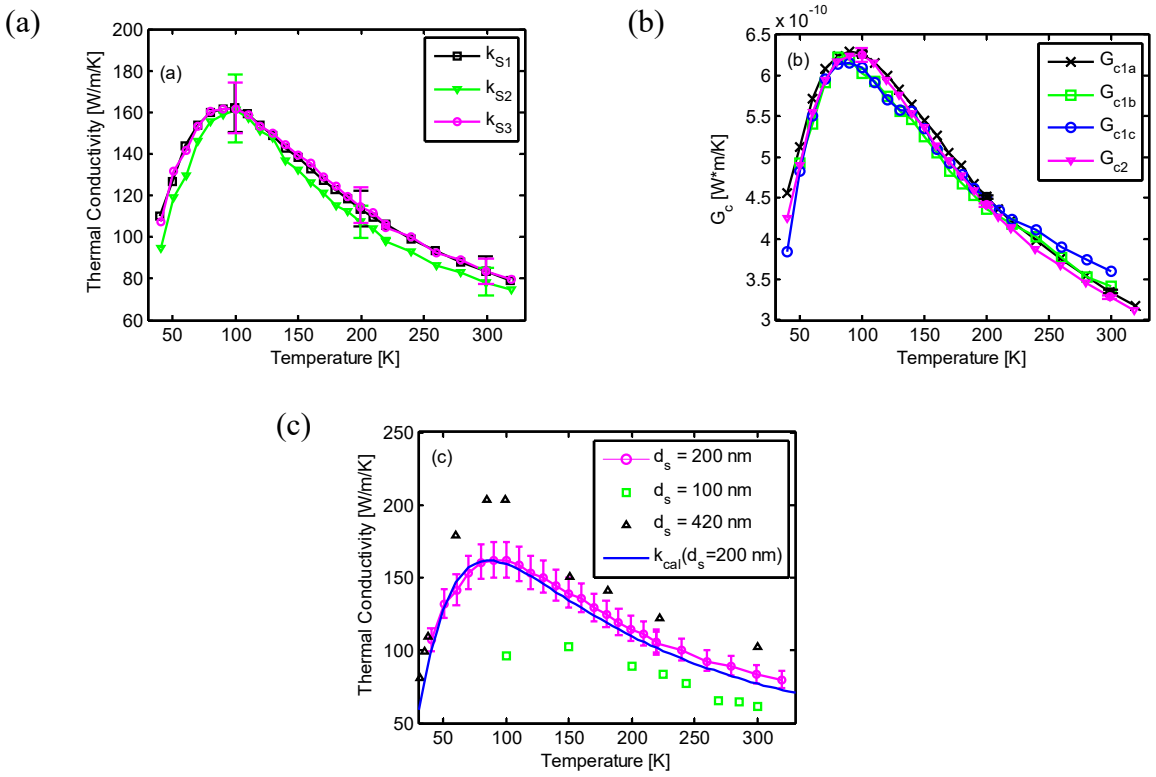

Figure 2.5: (a) Temperature-dependent thermal conductivity of a 200 nm thick silicon sample measured with the three measurement approaches. k_{S1} refers to the measurement from the composite beam alone, k_{S2} refers to the cross-beam data extraction assuming the thermal conductance from the composite beam, and k_{S3} refers to the data extracted using the direct differential method. Representative error bars are shown at 100, 200, and 300 K. (b) Temperature-dependent thermal conductance of the heater beam in composite-beam (G_{c1a}, G_{c1b}, and G_{c1c}) and cross-beam (G_{c2}) structures. Sample G_{c1a} is the composite beam fabricated on the wafer closest to the cross-beam sample, while the additional composite-beam structures (G_{c1b} and G_{c1c}) are farther away from the cross-beam structure and demonstrate the sample-to-sample variation of G_c. Representative error bars for G_{c1a} and G_{c2} are shown at 100, 200, and 300 K. (c) Temperature-dependent thermal conductivity of 200 nm thick silicon film from the direct differential measurement, in comparison to 100 and 420 nm thick silicon thin films from literature[19,29]. The calculated thermal conductivity k_{cal} (blue line) based on kinetic theory agrees well with temperature-dependent thermal conductivity measured in the present work.

In short, the two-step, direct differential measurement of the cross beam structure before and after the FIB cut allows efficient, accurate, and direct extraction of sample thermal conductivity. In addition, comparison of measured k enables evaluation of the assumptions typically applied in micro/nanoscale thermal measurements.

2.2.5 Results

2.2.5.1 Validation of the Experimental Method with 200 nm Thick Silicon

The thermal conductivity and thermal conductance of a 200 nm thick silicon layer obtained from the direct differential method are shown in Figure 2.5. To evaluate the measured temperature-dependent thermal conductivity, we analyze the thermal conductivity using the Callaway-Holland model:[30,31]

$$k = \frac{1}{6\pi^2}\sum_j \int_q C_j(q,T)\, v_j(q)^2\, \tau_j(q,T)\, q^2 dq \tag{2.9}$$

where $C_j(q, T)$, $v_j(q)$, and $\tau_j(q, T)$ are the specific heat, group velocity, and relaxation time for phonon branch j, respectively. Group velocity is calculated using a fourth-order polynomial fit to the phonon dispersion relationship in the [001] direction.[32] The relaxation time for phonons in bulk silicon is determined by fitting to bulk silicon thermal conductivity data[33–35] and Matthiessen's rule is used to calculate the relaxation time phonons in silicon TFs:

$$\tau_{j,bulk}^{-1}(q,T) = \tau_{j,Umklapp}^{-1} + \tau_{j,impurity}^{-1} + \tau_{j,boundary}^{-1} \tag{2.10}$$

where $\tau_{j,Umlapp}^{-1} = AT\omega_j(q)^2 \exp(-\theta/T)$, $\tau_{j,impurity}^{-1} = B\omega_j(q)^4$, and $\tau_{j,boundary}^{-1} = v_j(q)/C$. A, B, C, and θ are fitting parameters detemrmined by fitting to temperature dependent thermal conductivity of bulk silicon. Here, we use the same fitting parameters in the group velocity and relaxation time for bulk silicon as in Hopkins *et al*[34,35]. Calculated bulk silicon thermal conductivity agrees well with experimental data from Ho *et al*,[33] which confirms the selection of these fitting parameters. The reduced relaxation time due to boundary scattering is calculated based on the Fuchs-Sondheimer model:[36,37]

$$\tau_j(q,T) = F\left(\frac{d_s}{\Lambda_{j,bulk}(q,T)}, p\right)\tau_{j,bulk}(q,T) \tag{2.11}$$

$$\tau_j(q,T) = F\left(\frac{d_s}{\Lambda_{j,bulk}(q,T)}, p\right)\tau_{j,bulk}(q,T) \tag{2.12}$$

where $\Lambda_{j,bulk}(q,T)$ is the phonon mean free path and p is the boundary specularity parameter. The reduction function for in-plane phonon transport is well defined as:[36,37]

$$F\left(\delta=\frac{ds}{\Lambda},p\right)=1-\frac{3(1-p)}{2\delta}\int_1^{\infty}\left(\frac{1}{\xi^3}-\frac{1}{\xi^5}\right)\frac{1-\exp(-\delta\xi)}{1-p\exp(-\delta\xi)}d\xi \tag{2.13}$$

Good agreement is achieved for the measured silicon thin films using this kinetic theory model, as shown in Figure 2.5 (c). In addition, a comparison with temperature-dependent thermal conductivity of silicon thin films (d_s = 100 nm and 420 nm) from previous measurements[19,29] is shown in Figure 2.5 (c). Note the peak in thermal conductivity shifts to higher temperatures with decreased film thickness.

2.2.5.2 Evaluation of Conventional Methods

As k_{S3} is obtained directly from the differential measurement before and after the FIB cut, the accuracy of the other approaches at extracting thermal conductivity are investigated by comparison to k_{S3}. Specifically, the comparison sheds light on the validity of assumptions in the other approaches.

For the specific sample tested here, the measurement from the composite beam alone agrees well with direct differential method. There is no measureable difference between thermal conductivity of 200 nm silicon film with and without coating layers, which verifies the accuracy of the negligible interfacial effects assumption in this case. In part, this is because the thermal conductance of the silicon layer dominates the thermal conductance of the composite beam ($k_{Si}A_{Si} \gg (k_mA_m + k_dA_d)$) across the entire temperature range of interest. It is noteworthy that this method is based on estimation of the metal and dielectric properties, not direct measurements. Thus, its reliability should be evaluated case by case and is particularly suspect when the conductances are comparable. In addition, the thermal conductivity extracted using this method should be specified as k of the sample layer with coating layers. Thermal conductivity of sample films with and without coatings can be significantly different in some materials. An example is that thermal conductivity of suspended 2D materials, such as graphene, is generally higher than that of encapsulated or on-substrate graphene.[10,15]

As for the assumption of fabrication uniformity, relatively large variation exists between the directly measured k_{S3} and indirectly extracted k_{S2} with the assumption that the composite beam and the heater within the cross-beam are identical. That indicates the inappropriateness of the assumption of uniformity in some cases. The difference of measured thermal conductance of the heater beam from three composite-beam (G_{c1a}-G_{c1c}) structures and one cross-beam (G_{c2}) structure,

as shown in Figure 2.5 (b), can explain the deviation of measured thermal conductivity of the sample film. Further, the deviation in the low current electrical resistance between the composite- and cross-beam structures (see Figure 2.3 (b)) confirms some fabrication nonuniformity. Even though these structures are designed to be identical and fabricated simultaneously, variation in the fabricated structures are present and, thus, it is not reliable to assume identical G_c here. To confirm that, data from two additional composite-beam structures (G_{c1b} and G_{c1c}) farther away from the cross-beam structure demonstrate the relatively large variation of G_c across the wafer.

These results highlight the importance of the direct differential measurement using the cross-beam heater thermal conductance rather than via indirect measurement or approximations.

2.2.5.3 Uncertainty Quantification

Uncertainty in the measured thermal conductivity is analyzed by evaluating the fitting of $\bar{R}(I)$ considering the variations in the different input parameters. Figure 2.6 shows uncertainty contributions of temperature coefficient of resistance, geometrical dimensions, *etc*. Experimental uncertainty arising from the temperature coefficient of resistance and geometrical dimensions can be significant. For dimensions measured using SEMs, the length, width, and thickness are assumed to be accurate within ±0.1%, ±1.0% and ±5.0%, respectively, based on multiple measurements within the sample structure. In addition, we estimate ±15% uncertainty in the thermal conductivity of the metal layer calculated using Wiedemann-Franz law and ±1% uncertainty in the temperature coefficient resistance. In both the composite- and cross-beam measurement, geometrical dimensions are the main source of uncertainty due to the nonuniformity of samples.

The uncertainty contribution of temperature coefficient of resistance is generally small as $R(T)$ for Pt/Cr is sufficiently linear throughout the experimental temperature range. In the composite-beam measurement, the uncertainty as a result of using estimated thermal conductivity of metal and dielectric layers increases with temperature. Here, the uncertainty due to this estimation is generally small as silicon layer carries most of the heat at 200 nm thickness. In other words, the composite-beam measurement is accurate when G of the sample layer is significantly higher than that of the metal and dielectric layers. However, its reliability needs to be reevaluated as the metal and dielectric layers carry more heat or the interface resistance is significant. To highlight this, the impact of the estimated metal thermal conductivity on the composite-beam measurement accuracy is analyzed analytically assuming that the thermal conductance of the metal

layer is half of the total thermal conductance G_{c1}. as shown in Figure 2.6 (g-i), the uncertainty as a result of using estimated thermal conductivity of metal and dielectric layers is significantly higher than for the thick silicon case (see Figure 2.6 (a-c)) as the metal thermal conductance is now half of the total thermal conductance. In these cases, the composite-beam measurement loses its accuracy due to its reliance on this estimation, while the direct differential cross-beam measurement approach does not.

Furthermore, the thermal conductivity of 1.5 μm SiO_2 deposited on Si substrate using plasma enhanced chemical vapor deposition (PECVD) is measured (see Figure 2.7) for verification of this analysis as the thermal conductances of the metal and sample layer are of the same order of magnitude. For the composite-beam measurement, it is important to design the structure with small thermal conductance of the metal and dielectric layers, compared with that of the sample layer.

Note that in all measurements, the uncertainty in geometrical parameters (L_c, L_s, W and d) dominates over the uncertainty from other parameters in the data analysis. To reduce the uncertainty, samples should be prepared with good uniformity and thus with decreased uncertainty in geometrical dimensions. However, it is challenging to ensure excellent uniformity in micro/nanoscale fabrication.

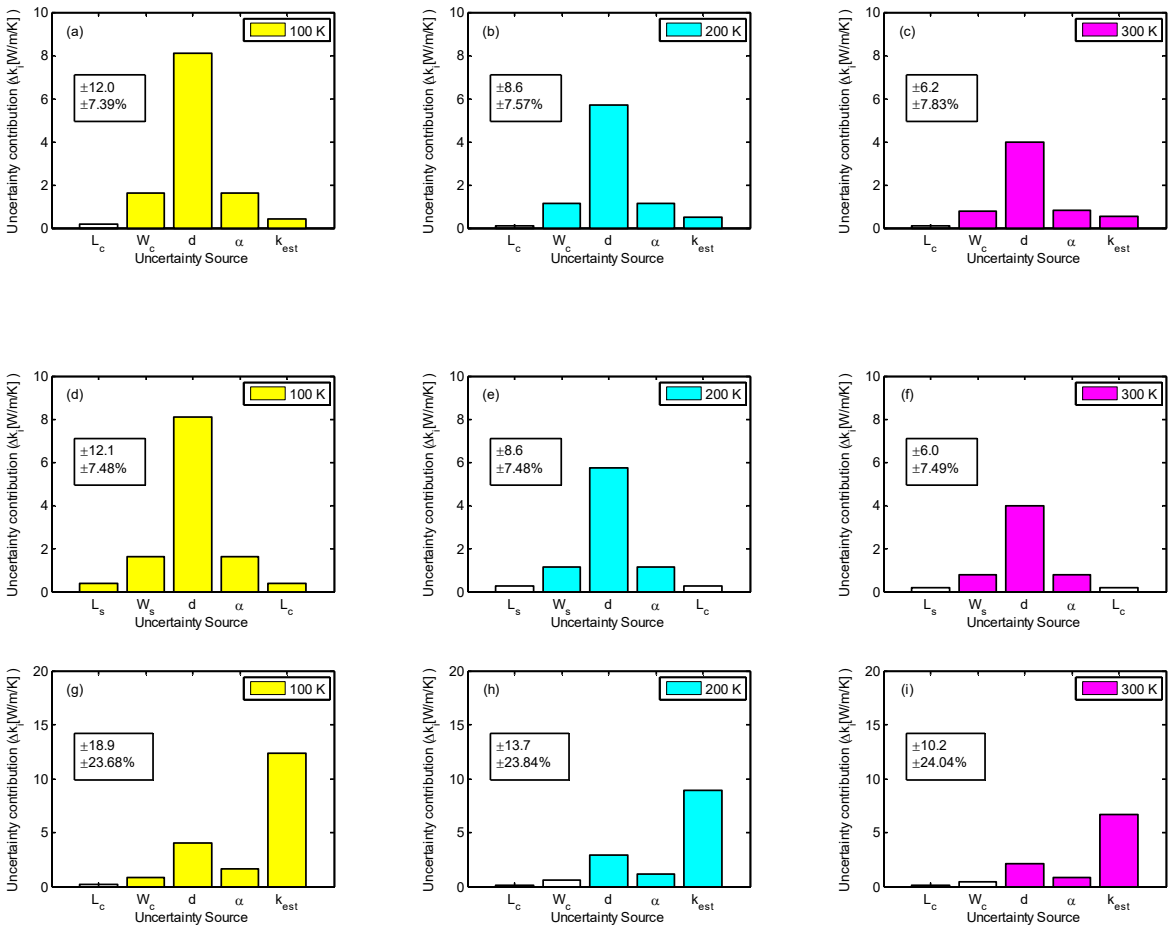

Figure 2.6: Uncertainty contributions from various sources in (a - c) the composite-beam measurement and (d -f) the cross-beam measurement of 200 nm thick films at 100 K, 200 K, and 300 K. Note that in these cases the uncertainty in geometrical parameters (L_c, L_s, W and d) dominates over uncertainty from other parameters in the data analysis. (g - i) Uncertainty contributions from various sources in the composite-beam measurement at 100 K, 200 K, and 300 K, respectively, assuming the metal thermal conductance is half of the total thermal conductance (as it would be for an ultrathin silicon sample). For this case, the uncertainty due to the estimated thermal conductivity of metal and dielectric layers dominates over uncertainty in geometrical parameters. The boxed numbers in each panel are the total absolute and relative uncertainty, respectively, for that measurement technique and temperature.

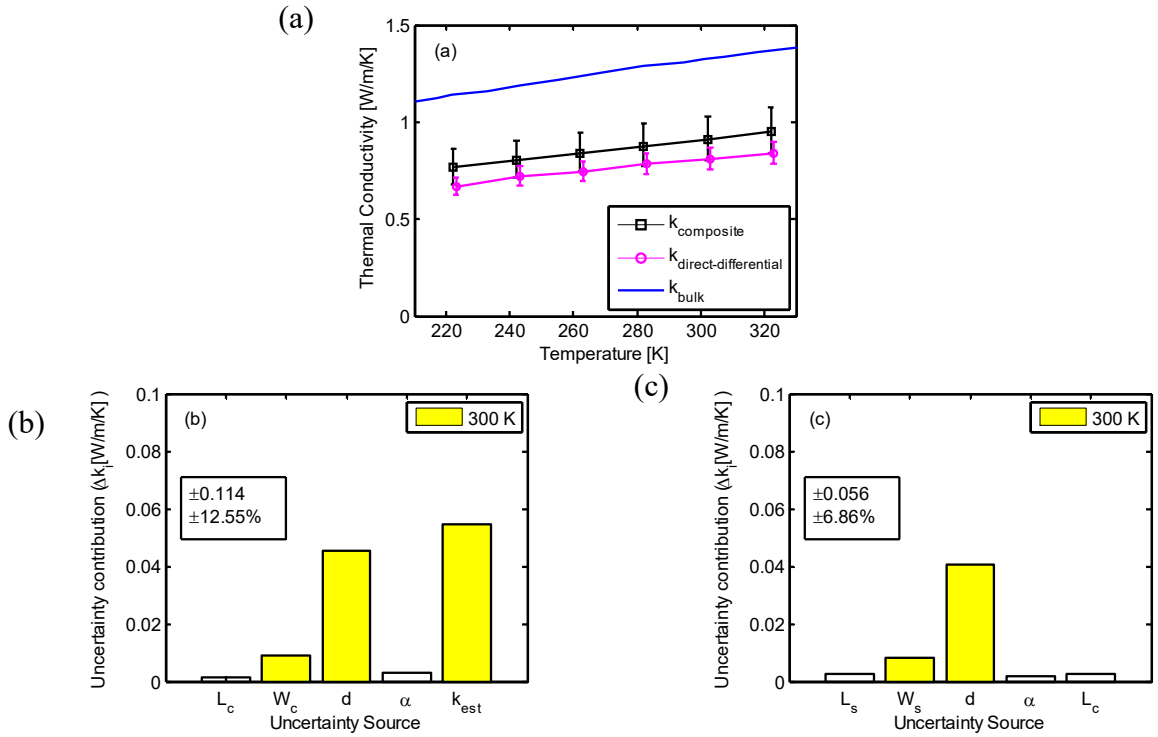

Figure 2.7: (a) Thermal conductivity of 1.5 μm SiO_2 prepared by PECVD. In this case, the direct differential method is more accurate than the composite beam method, as shown in the error bars. Uncertainty contributions from various sources in (b) the composite-beam measurement and (c) the cross-beam measurement are analyzed. The boxed numbers in panel (b) and (c) are the total absolute and relative uncertainty, respectively, for that measurement technique and temperature. As thermal conductances of the metal and sample layer are of the same order of magnitude, uncertainty due to estimation of the metal thermal conductance becomes significant in the composite beam method and thus its uncertainty increases. Uncertainty contribution due to the estimation can be much larger as the metal carries most of the heat in the composite beam, which is common in characterization of ultrathin samples. The cross-beam measurements with FIB allow direct determination of sample thermal conductivity, which is not limited by the estimation accuracy. Further, the thermal conductivity obtained from the composite beam method is higher than that from the direct differential method, which implies the inaccuracy of the estimation. The thermal conductivity of PECVD SiO_2 measured in this work is compared to thermal conductivity of bulk amorphous SiO_2.[38] The thermal conductivity of PECVD SiO_2 is generally lower than that of bulk oxide mainly due to its larger porosity.[39]

2.2.5.4 Summary

In this work, we demonstrate the effectiveness of a simple direct differential electrothermal measurement of thermal conductivity based on a cross-beam measurement structure with FIB. Comparison to the directly measured *k*, the accuracy of two conventional methods is investigated and the validity of related assumptions are discussed. These results highlight the advantages of the

direct differential method for accurate measurements of the thermal conductivity of nanostructures such as TFs due to the variations from sample-to-sample. This approach is broadly applicable to the measurement of the thermal conductivity of other micro- and nanostructures including nanowires and 2D materials.

2.3 Extension for Combined Strain Control & Thermal Metrology

A thermo-mechanical metrology platform is developed for studying strain dependent thermal transport taking advantage of strain control through flexible substrate. This method leverages electrothermal heaters/temperature sensors to measure thermal conductivity and builds on our past work with the cross-beam structures. An overview of the sample structure is shown in Figure 2.8. The patterned thin metal films act as a heater or resistive temperature sensor. In the measurement, using one of the metal beams as the heater and the other as the sensor. The temperature in the heating beam is parabolic and heat loss through the sample film impacts the temperature profile. Both the heater and sensor leverage the temperature-dependent electrical resistance of the metal to measure the spatially averaged temperature of the beam.

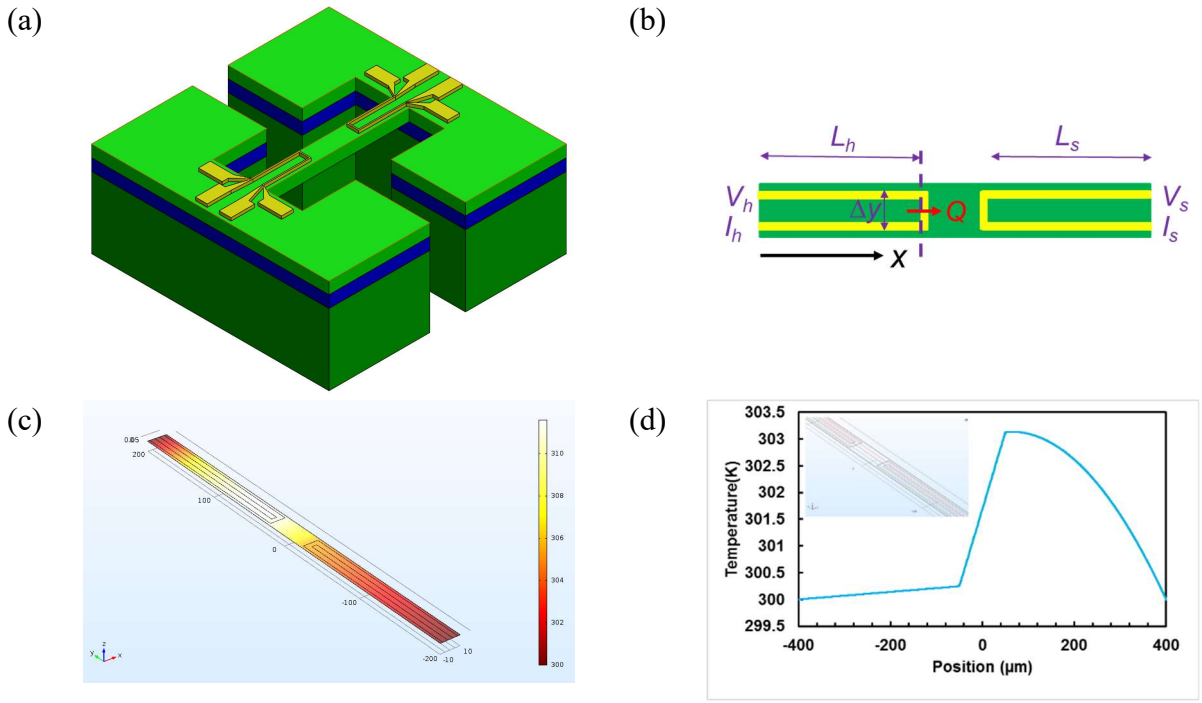

Figure 2.8: (a) Fully suspended electrothermal measurement device with patterned metal lines (yellow) on the sample layer (bright green), buried oxide layer (blue), and thin silicon substrate (dark green). The oxide layer is not necessary for sample layers with high etch selectivity compared to the substrate. (b) Geometry of the patterned metal lines on the suspended sample layer. (c) Heat conduction analysis of the suspended beam using COMSOL and (d) Temperature profile along several axial cutlines along the beam verifying one-dimensional heat transfer as the temperature are identical.

Heat conduction in the heating beam is governed by the steady-state 1D heat diffusion equation:

$$-k_c \frac{\partial^2 \Delta T_h}{\partial x^2} = q_h, \tag{2.14}$$

$$\Delta T_{h,x=0} = 0, \tag{2.15}$$

$$(L_h \cdot \overline{\Delta T_h} + \frac{\Delta y_h}{2} \cdot \Delta T_{h,x=L_h}) / (L_h + \frac{\Delta y_h}{2}) = \frac{V_h}{\alpha_h I_h R_{h,0}} - \frac{1}{\alpha_h}, \text{ and} \tag{2.16}$$

$$I_h^2 R_h = k_c A_c \left. \frac{d\Delta T_h}{dx} \right|_{x=0} + \frac{k_c A_c}{L_s} \cdot (\frac{V_s}{\alpha_s I_s R_{s,0}} - \frac{1}{\alpha_s}) \cdot \frac{2L_s + \Delta y_s}{L_s + \Delta y_s}, \tag{2.17}$$

where ΔT_h (ΔT_s) and $\Delta \bar{T}_h$ ($\Delta \bar{T}_s$) are the temperature rise and the average temperature rise of the heating (sensing) beam from 0 to L_h (L_s), respectively. For thermal analysis, the heating (sensing)

beam is divided into two parts of length L_h (L_s) and Δy_h (Δy_s) as shown in Figure 2.9 (b). k_c and A_c are the thermal conductivity and cross-section area of the composite heating and sensing beams, respectively. V_h (V_s), I_h (I_s), α_h (α_s), and $R_{h,0}$ ($R_{s,0}$) are the voltage, applied current, temperature coefficient of resistance, and resistance at the base temperature of the heating (sensing) beam, respectively, and $q_h = I_h^2 R_h/(L_h A_c)$ is the volumetric heat generation rate of the heating beam from 0 to L_h. Based on the linear temperature dependence of the resistance, the average temperature rise of the heating and sensing beam are $(V_h/I_h\text{-}R_{h,0})/\alpha_h R_{h,0}$ and $(V_s/I_s\text{-}R_{s,0})/\alpha_s R_{s,0}$. In the sensing beam, the applied current is small enough to ensure negligible Joule heating and a linear temperature profile along the beam. Thus, the temperature rise in the sensing beam results from the heat flow across the sample, but not its own heat generation. This helps determine the temperature rise profile along the sensor beam and enables extraction of the temperature at the cold end of the sample.

Assuming constant temperature of at the supported ends of each beam, the analytic solutions for ΔT_h and k_c in terms of the measured power and temperature rises are

$$\Delta T_h(x) = -\frac{q_h}{2k_c}x^2 + \left(\frac{2L_h+\Delta y}{L_h(L_h+\Delta y)}\cdot\left(\frac{V_h}{\alpha_h I_h R_{h,0}} - \frac{1}{\alpha_h}\right) + \frac{q_h L_h}{6k_c}\cdot\frac{2L_h+3\Delta y}{L_h+\Delta y}\right)\cdot x \text{, and} \tag{2.18}$$

$$k_c = \frac{\frac{q_h L_h}{6}\frac{4L_h+3\Delta y_h}{L_h+\Delta y_h}}{\left(\frac{V_h}{\alpha_h I_h R_{h,0}} - \frac{1}{\alpha_h}\right)\frac{2L_h+\Delta y_h}{L_h(L_h+\Delta y_h)} + \left(\frac{V_s}{\alpha_s I_s R_{s,0}} - \frac{1}{\alpha_s}\right)\frac{2L_s+\Delta y_s}{L_s(L_s+\Delta y_s)}}. \tag{2.19}$$

To extract thermal conductivity of the sample, an energy balance related to heat flow through the sample is computed as

$$I_h^2 R_h = k_c A_c \left.\frac{d\Delta T_h}{dx}\right|_{x=0} + kA\frac{\Delta T_{h,L_h} - 2\overline{\Delta T_s}}{L}. \tag{2.20}$$

Therefore, the thermal conductivity is calculated from the measured power generation and temperature rises as

$$k = \frac{L}{A}\frac{I_h^2 R_h - \left(\frac{2L_h+\Delta y}{L_h(L_h+\Delta y)}\cdot\left(\frac{V_h}{\alpha_h I_h R_{h,0}} - \frac{1}{\alpha_h}\right) + \frac{q_h L_h}{6k_c}\cdot\frac{2L_h+3\Delta y}{L_h+\Delta y}\right)\cdot k_c A_c}{-\frac{q_h L_h^2}{6k_c}\cdot\frac{L_h}{L_h+\Delta y} + \frac{2L_h+\Delta y}{L_h+\Delta y}\cdot\left(\frac{V_h}{\alpha_h I_h R_{h,0}} - \frac{1}{\alpha_h}\right) - \left(\frac{V_s}{\alpha_s I_s R_{s,0}} - \frac{1}{\alpha_s}\right)\cdot\frac{2L_s+\Delta y_s}{L_s+\Delta y_s}}. \tag{2.21}$$

To investigate the strain dependence of *k*, axial strain is applied to the sample based on flexible substrate. Figure 2.9 (c) shows the suspended device is bonded on a flexible substrate and stretching the substrate changes the strain of the device and sample as they are boned together using epoxy. A custom-built mechanical stage, as shown in Figure 2.9 (a), is used to apply the strain with micrometer actuators. The substrate is fixed on the stage for strain control and can be transferred to the cryostat for thermal measurements. The strain level is determined using high resolution microscopes after the measurements.

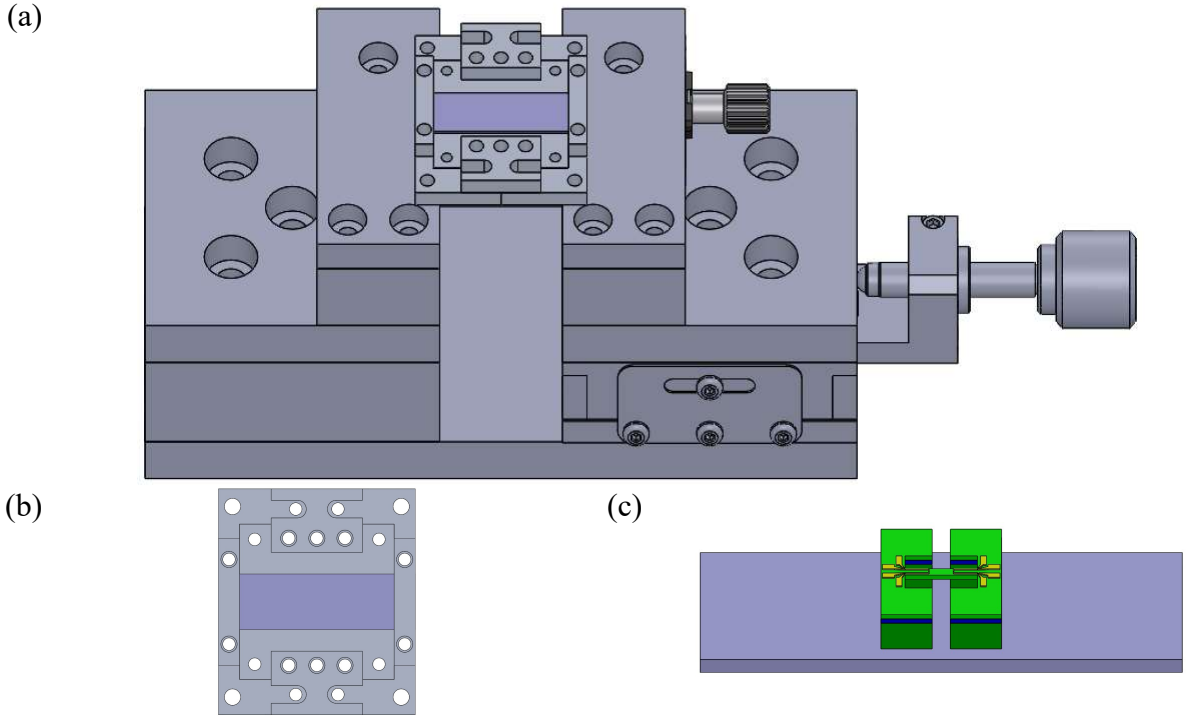

Figure 2.9: (a) Schematic of the custom-built mechanical stage for strain control, which allows stretching the flexible substrate with 10 μm resolution. (b) Top view of the sample holder detached from the microloading device with desired strain level. (c) Fully suspended devices bonded on a flexible substrate.

3. NANOSTRUCTURING FOR THERMAL CONDUCTION ANISOTROPY IN THIN FILMS[2]

3.1 Overview

For decades, the thermal conductivity (k) of nanostructured materials has been broadly studied and the measured k is generally reduced due to phonon size effects such as phonon-boundary scattering[2],[40]. However, the directional dependence of thermal conductivity has not been investigated as frequently, but is necessary for a full understanding of the thermal conductivity tensor. Moreover, thermal conduction anisotropy is promising for directing the heat flow pathways in modern applications including thermal management of electronic devices.[41]

Studies of thermal conductivity anisotropy are limited and the observed anisotropy ratio in natural materials is generally not high, even when the lattice and band structures are anisotropic, because of the diffusive nature of thermal transport. Recent thermal conductivity measurements of two dimensional (2D) materials demonstrate thermal conductivity anisotropy ratios up to ~3 for few-layer black phosphorus[13,42]. Given the demonstrated effectiveness of nanostructure engineering in tuning thermal conductivity, introducing appropriate anisotropic nanostructures should enhance thermal conduction anisotropy.

In this chapter, we introduce thickness-modulated thin films (TFs) as shown in Figure 3.1 to exploit the phonon boundary scattering and size effect in leading to anisotropic thermal conduction in the thin films. Specifically, the thin films of interest consist of alternating thick and thin strips leading to anisotropic structures not present in uniform films. We investigate the thermal anisotropy of thickness-modulated TFs of silicon, as an example material system, using full three-dimensional (3D) simulations based on the frequency-dependent Boltzmann Transport Equation (BTE). We show an enhanced thermal anisotropy ratio (>10) due to phonons scattering with the introduced anisotropic boundaries, which is not present in corresponding bulk materials.

[2] This section reproduced with permission from Y. Zeng and A. Marconnet, Phys. Rev. Applied **9**, 011001. Copyright 2018 American Physical Society

(a) (b)

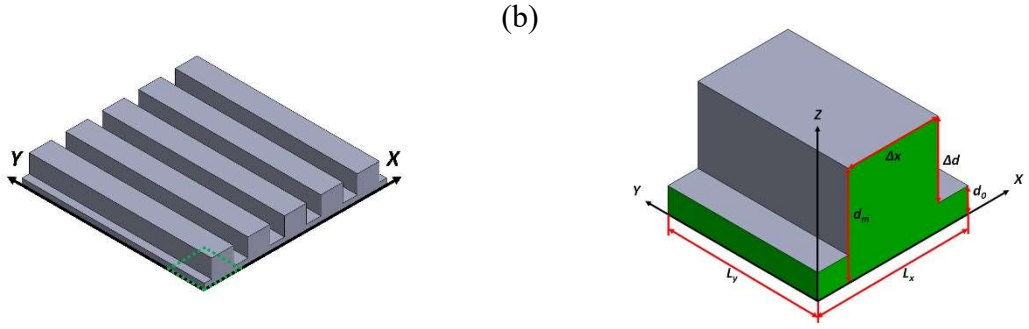

Figure 3.1: Schematic of the (a) thickness-modulated thin film and (b) unit cell for analysis. The two directions of interest are labeled as *x* and *y* directions. The region enclosed by green dashed lines in panel (a) is the unit cell used in our thermal simulations as shown in panel (b). The unit cell of size L_x x L_y x d_m is comprised of a bottom layer of size L_x x L_y x d_0 and a modulator of size Δx x L_y x Δd. The anisotropy of the unit cell is adjusted by tuning the width and thickness of the modulator. To simplify the analysis, we use $L_x = L_y = L$ and a fixed ratio $L/d_0 = 6$ in all cases, which facilitates the anisotropy study by varying the width ratio $WR = \Delta x/L_x$ and the thickness ratio $TR = d_m/d_0$. The length of the unit cell varies from 30 nm to 600 nm and the smallest unit cell is of size $L = 30$ nm and $d_0 = 5$ nm. A fixed temperature difference is applied along *x* or *y* directions and periodic boundary conditions are applied in the corresponding perpendicular in-plane direction in each simulation.

3.2 BTE & Monte Carlo Methods

The BTE for phonons can be used to characterize thermal transport in non-metallic crystals[43]. The BTE is generally simplified with relaxation-time approximation considering a balance between reliability and complexity as

$$\frac{\partial f}{\partial t} + V_g \nabla f = -\frac{f - f^{loc}}{\tau} \tag{3.1}$$

where f and f^{loc} are the distribution function and local distribution function, respectively, Vg is the phonon group velocity, ω is the phonon radial frequency, t is the time, and τ is the phonon relaxation time. As phonon follows a Bose-Einstein distribution, the equilibrium distribution at temperature T is

$$f_T^{eq} = \frac{1}{\exp(\frac{\hbar\omega}{k_b T}) - 1} \tag{3.2}$$

where $\hbar$ and k_b are Planck constant and Boltzmann constant, respectively.

The difficulty in directly solving BTE motivates the development of particle-based solution methods. Over the last decade, the development of Monte Carlo (MC) method for phonon transport has been one of significant achievements in micro- and nano- scale computational heat transfer. A major advantage of MC method is the convenient treatment of frequency dependence [44] and complicated geometries[34,45–49], which are critical for phonon transport in nanostructures. Furthermore, multiple scattering mechanisms can be included in the MC simulations independently. Therefore, the mechanisms are not lumped together via Matthiessen's rule as often used in simplified models of phonon transport. One of the first comprehensive phonon transport model for silicon thin films was presented by Mazumdar and Majumdar[50] and the impact of phonon dispersion and polarization was investigated. Later, Mittal and Majumdar[51] performed a systematic MC study of the role of various phonon modes including optical phonons on thermal conductivity prediction in silicon thin films. Since then, many researchers have investigated phonon transport using MC technique. It has been applied in simulations of phonon transport in nanowires[52–54], nanoporous structures[45,55,56], and other phonon related transport phenomena[57–59].

However, there are two main disadvantages to these traditional MC methods. First, the statistical method itself requires a large number of computational particles and a long time to attain statistical meaningful results. Thus, the traditional MC method is computationally expensive. Second, the algorithm based on phonon number distribution results in a natural conservation of the total number of phonon bundles rather than conserving the total energy. Specifically, an unphysical step involving the addition or deletion of phonons is required to achieve approximate energy conservation after resampling of the new phonon bundles with new states in the scattering step.

An energy-based variance-reduced Monte Carlo (VRMC) technique developed by Péraud and Hadjiconstantinou[60] overcame these two shortages in the traditional treatment. First, a variance-reduced formulation is introduced and only the deviation from equilibrium is simulated. The statistical uncertainty is largely reduced since only the deviation needs to be determined stochastically. Second, the energy-based formulation ensures a natural conservation of the total energy. All computational particles have the same amount of energy and thus the total energy is conserved as long as the number of particles is balanced. Moreover, the collision term in BTE can be linearized under small temperature differences and thus lead to a more efficient, decoupled

algorithm[61].

In section 3.2.1, the traditional Monte Carlo method is briefly described. Then in the following section (3.2.2), the variance reduced method is introduced and subsequently used for analysis of the modulated thin film structures.

3.2.1 Traditional MC methods

A traditional MC algorithm[50] starts from the initialization of phonons and repeats steps of emission, advection, and scattering of phonon samples until equilibrium. Specifically, the first step is to initialize the states of phonon bundles, which represent an appropriate number of particles. The accuracy of MC results can be improved as more phonon bundles are simulated and thus the computational cost increases accordingly. The number of phonon bundles is determined as a balance between the accuracy and computational cost. The phonon bundles are moved in each time step and its positions are updated. In this step, phonon colliding with boundaries should be considered, which can be specularly or diffusively reflected. The temperature and pseudo temperature are calculated in each subcell after this step. The next step is to decide scattered phonons according to its scattering probability and assign new states to scattered phonons based on the calculated distribution in the local cell. Besides, an emission step is necessary to maintain phonon flow through the unit cell. Phonon bundles can be emitted before the movement or after scattering step. These steps are repeated until statistically meaningful results attain.

(1) Initialization

This step is to set the initial states of phonon bundles, including its position, frequency, polarization, and velocity. The number of phonon is calculated using the Bose-Einstein statistics:

$$N = V \int_0^{\omega_c} \sum_p D(\omega, p) f_T^{eq}(\omega) d\omega \,, \tag{3.3}$$

where w_c is the cutoff frequency for a specific branch, V is the volume of a given system, and $D(w,p)$ is the density of states and is given by

$$D(\omega, p) = \frac{1}{8\pi^3} \int_{BZ} \delta(\omega(k, p) - \omega) d^3k \,. \tag{3.4}$$

Assuming an isotropic Brillouin zone and isotropic dispersion relation, the density of states is generally simplified as

$$D(\omega, p) = \frac{k^2}{2\pi^2 V_g}, \tag{3.5}$$

where the group velocity $V_g = \nabla_k \omega(k, p)$. Once the number of phonon bundles N_p is determined, the number of phonons in a phonon bundle is N/N_p. Phonon bundles are sampled based on corresponding probability density functions. For example, the probability of emitting a phonon bundle with frequency between w_0 and $w_0+\Delta w$ is given by

$$\frac{\Delta N}{N} = \frac{\int_{\omega_0}^{\omega_0+\Delta\omega} \sum_p D(\omega, p) f_T^{eq}(\omega) d\omega}{\int_0^{\omega_c} \sum_p D(\omega, p) f_T^{eq}(\omega) d\omega}. \tag{3.6}$$

(2) Movement

Phonons move with assigned velocities in this time step and the position is updated as

$$r_i(t+\Delta t) = r_i(t) + V_{g,i} \Delta t. \tag{3.7}$$

The time step Δt is selected to ensure the travel distance in one Δt smaller than the length of subcell. In other words, phonon bundles can only travel subcell by subcell, without skipping any subcells. This guarantees the physical meaning of the following statistical calculation. Phonons may collide with the domain boundaries during the travel. These boundaries can be emission boundaries, imaginary periodic boundaries, or realistic surfaces/interfaces. Various types of boundary conditions have been used to process phonon-boundary scatterings[44,50,60,62]. These will be discussed in the subsequent sections. After the travel step, the temperature of each subcell is determined based on its phonon energy density, which is the total phonon energy in a given volume ΔV divided by the volume as

$$\frac{E}{\Delta V} = \frac{N_{eff}}{\Delta V} \sum_{i,\Delta V} \hbar \omega_i = \int_0^{\omega_c} \sum_p \hbar \omega D(\omega, p) f_T^{eq}(\omega) d\omega, \tag{3.8}$$

and the temperature is calculated by inverting the energy density. Similarly, the pseudo temperature T_{loc} can be calculated by inverting the pseudoenergy density as

$$\frac{\widetilde{E}}{\triangle V}=\frac{N_{eff}}{\triangle V}\sum_{i,\triangle V}\frac{\hbar\omega_i}{\tau_i(\omega_i,p_i,T)}=\int_0^{\omega_c}\sum_p\frac{\hbar\omega D(\omega,p)}{\tau_i(\omega_i,p_i,T)}f_{T_{loc}}^{eq}(\omega)d\omega\,, \tag{3.9}$$

where $\tilde{E}$ is the pseudoenergy derived from the solution of BTE[44].

(3) Scattering

In this step, the scattering probability of each phonon is calculated as

$$P_i=1-\exp(-\frac{\triangle t}{\tau(\omega_i,p_i,T)})\,, \tag{3.10}$$

and the phonon is scattered once the calculated probability is greater than the sampled random number. Then, new frequencies, polarizations, and velocities are assigned for scattered phonons from the pseudo distribution f/τ, which agrees with the BTE solution[44]. An additional substep adding or deleting phonons is required since the energy is not naturally conserved due to the randomly drawn frequencies of scattered phonons. This above process is limited to internal scatterings such as phonon-phonon scattering and impurity scattering.

As for boundary scattering, it can be added as an extra term via the Mathiessen's rule. But this simple treatment is believed to be inaccurate since boundary scattering occurs at the surfaces while internal scatterings are volumetric processes[63]. Instead, phonon-boundary scattering is typically analyzed based on the geometry and specularity parameter, which is the probability that a phonon is specularly reflected at the surface. The specularity p is generally calculated using an analytical equation by Ziman[43]

$$p=\exp(-4\eta^2k^2\cos^2\theta)\,, \tag{3.11}$$

where η is the root mean square surface roughness and θ is the angle of incidence. Compared to a random number, the phonon is specularly reflected if the random number is less than the calculated specularity or the phonon is diffusely reflected. When reflected, only the traveling direction is modified due to the reflection, while other states maintain the same.

(4) Emission

The hot and cold ends of the geometry emit phonons to maintain the temperature difference and phonon flow. The emission wall is generally analogous to a black surface for photon radiation. A periodic emission boundary condition with constant virtual temperature, developed by Hao *et al.*[44], enables the simulation using only one unit cell.

3.2.2 VRMC Methods

The algorithm of VRMC is similar to the traditional MC algorithm, but with distributions in different formulations[60,61]. Multiplying the BTE by $\hbar w$, the energy-based BTE is obtained:

$$\frac{\partial e}{\partial t}+V_g\nabla e=-\frac{e-e^{loc}}{\tau}, \tag{3.12}$$

where $e = \hbar wf$ and $e_{loc} = \hbar wf_{loc}$. As phonons follow the Bose-Einstein distribution, an equilibrium state can be calculated by $e^{eq}_{T_{eq}}(\omega)=\hbar\omega f^{eq}_{T_{eq}}$. With a determined nearby equilibrium state, the energy-based deviational formulation of BTE is

$$\frac{\partial e^d}{\partial t}+V_g\nabla e^d=\frac{(e^{loc}-e^{eq}_{T_{eq}})-e^d}{\tau}, \tag{3.13}$$

where $e^d = e - e^{eq}_{T_{eq}}$. The variance-reduced algorithm, developed by Péraud and Hadjiconstantinou[60], is used to solve the deviational form of the BTE. Significant computational savings are achieved as only the energy deviation distribution needs to be determined stochastically rather than the whole energy distribution. A simplified collision operator reduces the computational cost further. The collision operator can be linearized as $e^{loc}-e^{eq}_{T_{eq}}\approx(T_{loc}-T_{eq})\frac{de^{eq}_{T_{eq}}}{dT}$ when $T_{loc} - T_{eq}$ is sufficiently small, which can be modified by setting the temperature difference across the simulation domain. With the linearized collision operator, the sampling process of scattered phonons based on $(e^{loc}-e^{eq}_{T_{eq}})/\tau$ is greatly simplified as the probability to resample a computational particle with frequency between w_0 and $w_0+\Delta w$ becomes

$$\frac{\int_{\omega_0}^{\omega_0+\Delta\omega}\sum_p D(\omega,p)\frac{(e^{loc}-e^{eq}_{T_{eq}})}{\tau}d\omega}{\int_0^{\omega_c}\sum_p D(\omega,p)\frac{(e^{loc}-e^{eq}_{T_{eq}})}{\tau}d\omega}\approx\frac{\int_{\omega_0}^{\omega_0+\Delta\omega}\sum_p D(\omega,p)\frac{de^{eq}_{T_{eq}}}{\tau dT}d\omega}{\int_0^{\omega_c}\sum_p D(\omega,p)\frac{de^{eq}_{T_{eq}}}{\tau dT}d\omega}, \tag{3.14}$$

where T_{loc} is decoupled from the probability function in the scattering step. This speeds up the computation considering the huge cost to calculate T_{loc} inversely.

3.3 Results & Discussion

Previous BTE based simulations have demonstrated a decrease in the thermal conductivity of diameter-modulated nanowires and width-modulated nanoribbons.[53,64,65] In such structures, the thermal conductivity is reduced due to enhanced phonon scattering with boundaries. As these are one-dimensional structures, only thermal transport perpendicular to the modulation was investigated. However, in the thickness-modulated nanofilms, two directions can be evaluated: parallel to the modulation features (or "modulators") and perpendicular to the modulation features, and little is known about phonon transport parallel to the modulators. Given that the phonon size effect dominates in the nanoscale, anisotropic boundaries imply anisotropic phonon boundary scattering rates and, hence, the possibility to enhance the thermal anisotropy in modulated nanofilms. A full study of thermal transport along both directions sheds light on the thermal anisotropy induced by anisotropic boundaries.

We perform full 3D simulations of the modulated structure considering a unit cell (L_x x L_y x d_m) with a continuous bottom layer (L_x x L_y x d_0) and a modulator (Δx x L_y x Δd) on top, as shown in Fig. 3.1. The anisotropy of the unit cell is controlled by tuning the width and thickness of the modulator. Corresponding aspect ratios are defined as $WR = \Delta x/L_x$ and $TR = d_m/d_0$. We use $L_x = L_y = L$ and a fixed ratio $L/d_0 = 6$ in all cases without loss of generality as the impact of varying L and d_0 is evaluated as we vary WR and TR, respectively. In addition, we investigate the size effects of the unit cell by adjusting L from 30 nm to 600 nm.

Note that in the y direction, the cross-sectional area for heat conduction is constant (L_x x $d_o + \Delta x$ x Δd), but for conduction in the x direction, the cross-sectional area alternates between L_y x d_o and L_y x d_m as the thickness varies. Thus, here, the nominal thermal conductivity is defined based on the cross-sectional area of the unit cell at the center of the unit cell (*e.g.*, the full height d_m). Specifically, when extracting the thermal conductivity along x direction from the temperature gradient and heat flow rates, the nominal area for heat conduction is defined as L_y x d_m. To avoid confusion in the varying areas when evaluating the anisotropy ratio, we define the thermal conduction anisotropy ratio based on the ratio of the heat fluxes required to maintain a given temperature gradient in that direction:

$$\gamma = \frac{q_x}{q_y} = \frac{(kA)_{eff,x}}{(kA)_{eff,y}} = \frac{k_x L_x}{k_y L_y} \tag{3.15}$$

where $(kA)_{eff}$ and k are the effective thermal conductance and the nominal thermal conductivity, respectively. In all cases, $\gamma=q_x/q_y=k_x/k_y$ as $L_x=L_y=L$ is defined for all unit cells. And the equivalence of thermal anisotropy ratios based on the nominal thermal conductivity and the effective thermal conductance avoids confusion in the thermal anisotropy study.

To compute the direction-dependent thermal conductivity, an efficient energy-based variance-reduced Monte Carlo (MC) algorithm adapted from the work of Péraud and Hadjiconstantinou[60] solves the BTE directly in the 3D unit cell. Periodic boundary conditions at appropriate faces allow thermal transport simulations using a single periodic unit cell[44]. In MC-based techniques, the BTE is solved by stochastically simulating phonon samples, which represent an ensemble of phonons. The standard algorithm starts from the initialization of phonons and repeats steps of emission, advection, and scattering of phonon samples until equilibrium. The computational cost is significantly reduced by solving the energy-based variance-reduced BTE[60]:

$$\frac{\partial e^d}{\partial t} + V_g \cdot e^d = \frac{(e^{loc} - e^{eq}_{T_{eq}}) - e^d}{\tau} \tag{3.16}$$

where e^d is the energy-based deviation distribution from a deterministic nearby equilibrium, $(e^{loc} - e^{eq}_{T_{eq}})$ is the local deviation distribution, V_g is the phonon group velocity, t is the time, and τ is the phonon relaxation time. Additional computational efficiency is achieved by solving the linearized BTE with small temperature differences and the energy deviation from a deterministic nearby equilibrium[61]. In this work, only acoustic phonons are considered and the phonon dispersion relationship is approximated using a fourth-order polynomial fit to the dispersion along the [001] direction[32]. We use the same relaxation times for (acoustic) phonon-phonon scattering as in Minnich *et al.*[66], and the impurity scattering rate is determined by fitting to the bulk thermal conductivity for a nearly pure silicon sample. With this approach, the calculated thermal conductivity for bulk Si at 300 K is 156.4 $Wm^{-1}K^{-1}$ using an impurity scattering rate of $\tau^{-1} = 3 \times 10^{-45}\omega^4\ s^{-1}$, which agrees well with the experimental value of k = 155 $Wm^{-1}K^{-1}$.[67,68] Further, to validate our simulations accuracy in capturing the effect of phonon boundary scattering, we calculate thermal conductivities of silicon TFs across a wide-range of thicknesses (5 nm to 5000 nm) using diffusive boundary conditions, which is reasonable for phonon transport in Si TFs at 300 K. Figure 3.2 illustrates the good agreement between the calculated thermal conductivity using our BTE model and recent experimental data for thickness-dependent silicon TFs[23,24].

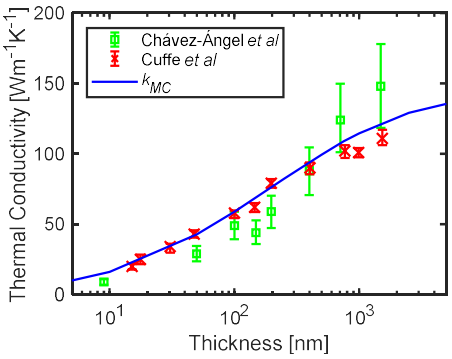

Figure 3.2: Thickness-dependent thermal conductivity of silicon TFs across a wide range of thicknesses. The calculated thermal conductivity, k_{MC}, from our simulations agrees well with recent experimental data by Chávez-Ángel *et al*[23] and Cuffe *et al*[24], indicating that our model accurately captures the phonon boundary scattering effect.

To understand how the modulations impact the thermal conduction anisotropy, we perform thermal transport simulations over unit cells with varying L, WR, and TR. Periodic boundary conditions are applied at the pseudo boundaries along the periodic directions, while all other boundaries are assumed to be diffusive. As a comparison, we compute the directional-dependent thermal conductivity of the unit cells based on heat diffusion equation (with no consideration of the phonon size effects) using a 3D COMSOL model for unit cells of the same geometry. As thermal conductivity is a material property in bulk systems, the calculated thermal anisotropy ratio is independent of the size of the unit cell. In contrast, as a result of the phonon size effects at the nanoscale, the thermal anisotropy ratio increases as the size of the unit cell shrinks from L = 600 nm to L = 30 nm and the ratio approaches the corresponding bulk value as L increases, as shown in Figure 3.3 (a) and (b). This result highlights the importance of phonon size effects for enhancing thermal anisotropy, while the thermal anisotropy present in bulk scale is limited due to its single contribution from the different cross-sectional areas to conduct heat along x and y directions. Note that the anisotropy ratio can be as high as ~10 for a unit cell of size L = 150 nm and d_0 = 30 nm, which is experimentally feasible in current nanofabrication using a standard silicon-on-insulator wafer.

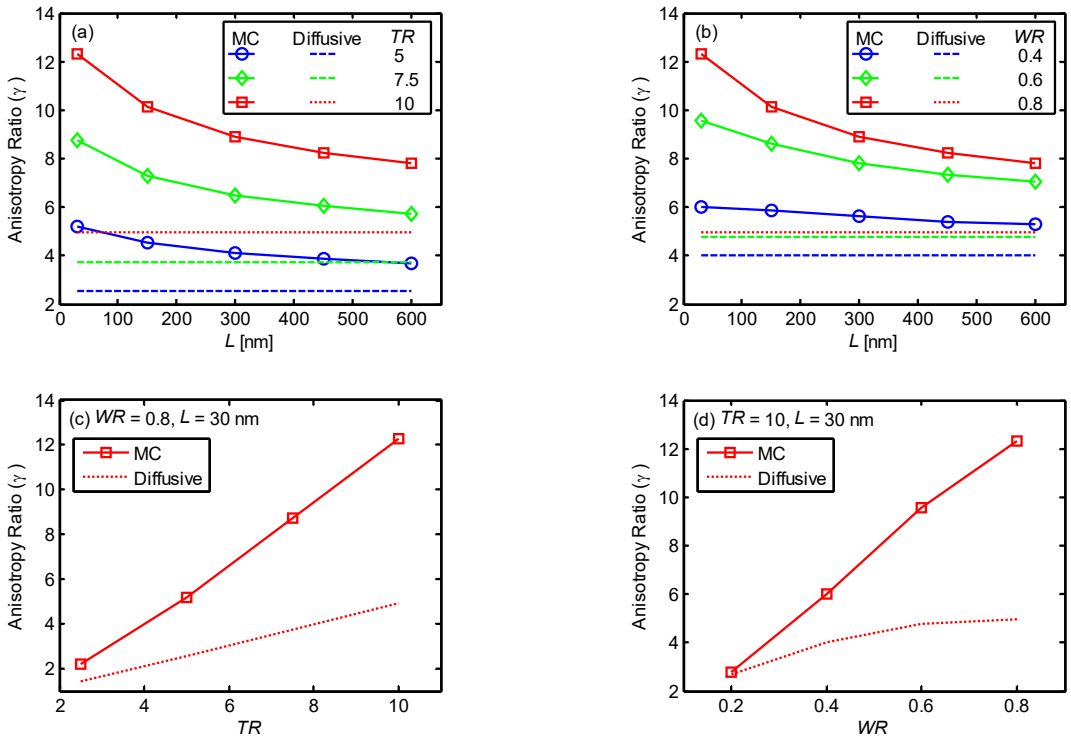

Figure 3.3: Thermal anisotropy as a function of system size (L) and (a) thickness ratio (TR) for a fixed width ratio (WR = 0.8) and (b) width ratio for a fixed thickness ratio (TR = 10) using our Monte Carlo (MC) simulations (solid lines) compared to a fully diffusive finite element model (dashed lines). Note that the anisotropy ratio decreases as the unit cell size increases and trends towards the diffusive result as L increases past the dominant phonon mean free paths. (c) Thermal anisotropy ratio as a function of TR for the unit cells with WR =0.8 and L = 30 nm. (d) Thermal anisotropy ratio as a function of WR for the unit cells with TR = 10 and L = 30 nm. Adjusting either the WR or the TR can achieve tuning thermal anisotropy ratio across an order of magnitude and tuning both parameters enables significant anisotropy with nanoscale feature sizes.

The anisotropy ratio increases with TR for all length scales (see Figure 3.3 (a) and (c)) including the diffusive regime. For the unit cell of L = 30 nm and WR = 0.8, the ratio is tuned from ~2 to ~12 as TR varies from 2.5 to 10. A similar trend is observed for the effect of WR, as shown in Figure 3.3 (b) and (d). Note that either tuning WR or TR under appropriate conditions can adjust the thermal anisotropy ratio over an order of magnitude. For the direction parallel to the modulator, the y direction in this scheme, the reflected phonons have random y-direction velocity components. However, in the direction perpendicular to the modulator, though diffusive boundary scattering randomizes the phonon velocity, the updated velocity component along x direction are flipped for phonons reflected by the perpendicular boundaries. That indicates the modulator as a more

effective structure to confine phonons traveling perpendicular to the modulator. As the characteristic length of the modulator increases, suppression of phonons traveling parallel to the modulator is greatly reduced as the characteristic length of the modulator increases with the width and thickness, while our simulations show no significant reduction of the phonon suppression along *x* direction with increased characteristic length. As a consequence, the increase of thermal conductance along *x* direction with *WR* and *TR* is very limited when compared to the increase along *y* direction, as shown in Figure 3.4, which explains the observed high anisotropy ratio (> 10).

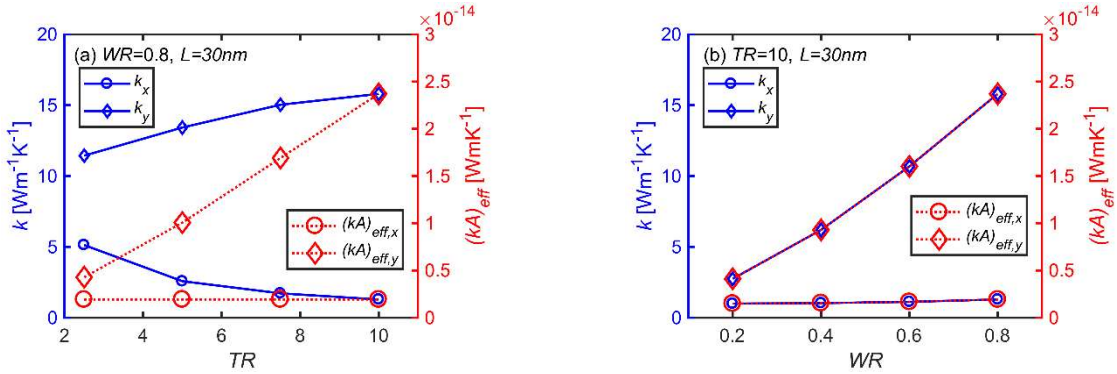

Figure 3.4: (a) Nominal thermal conductivity k and effective thermal conductance $(kA)_{eff}$ as a function of *TR* for the unit cells with *WR* =0.8 and L = 30 nm. (b) Nominal thermal conductivity k and effective thermal conductance $(kA)_{eff}$ as a function of *WR* for the unit cells with *TR* =10 and L = 30 nm. Note that both k_y and $(kA)_{eff,y}$ increase significantly with *TR* and *WR*, though no similar increase along *x* direction. That explains the high anisotropy ratio observed in the unit cells with large *WR* and *TR*.

In general, these structures are achievable using existing nanofabrication tools, but there are some limitations. Considering silicon as an example, achieving the desired thermal anisotropy with the increased *TR* requires a high aspect-ratio etch of silicon thin films. High anisotropic etching of silicon is practical given the reported etch aspect ratio up to 107 using deep reactive ion etch technique[69]. Another limitation is the size of the modulation features. Electron-beam lithography can define the pattern of the modulator as the unit cell shrinks to nanoscale, but is limited to ~ 10 nm resolution[70]. A conservative estimate demonstrates the experimental feasibility of fabricating the proposed structure of the unit cell of size L = 150 nm and d_0 = 30 nm, which is predicted to achieve a thermal anisotropy ratio greater than 10.

Romano and Kolpak[71] recently proposed nanoporous materials with anisotropic pore lattices with anisotropy ratio of > 10. Both their structure and our structure yield enhanced thermal

anisotropy ratios of > 10 by introducing anisotropic nanostructures. Our 3D structures offer additional flexibility of modulating the anisotropy due to the extra thickness modulation not available in 2D structures, which contributes to a relatively higher thermal anisotropy in our structures at relatively larger scales (L > 100 nm). In addition, our structures, based on continuous solid membranes, are more mechanically robust compared to porous films, which is a potential advantage for future applications in devices. In addition, the full 3D simulations using the MC method used in this report capture all boundary effects, which are critical for accurate predictions in nanoscale due to the correlation between phonon scattering with the boundaries.

In summary, we investigate the possibility of controlling the thermal conduction anisotropy using thickness-modulated thin films. We solve directly the phonon frequency-dependent BTE in 3D geometries of interest using an efficient MC algorithm. Our simulations capturing all phonon boundary scatterings demonstrate an increase in the thermal conduction anisotropy of an order of magnitude. The high thermal anisotropy, not naturally available in corresponding bulk materials, is promising for directing the heat flow pathways in thermal management related applications. Moreover, the proposed structure is experimental feasible with current nanofabrication technology and is advantageous for future applications in devices due to its mechanical robustness.

4. REEVALUATING THE SUPPRESSION FUNCTION FOR PHONON TRANSPORT IN NANOSTRUCTURES BY MONTE CARLO TECHNIQUES

Thermal conductivity integral models including a suppression function to account for boundary scattering have had considerable success in explaining and predicting the thermal conductivity of nanostructures. However, the suppression function is analytically defined only for some simple structures, *e.g.*, thin films and nanowires. For arbitrary nanostructures, Monte Carlo (MC) -based methods have been developed to calculate the suppression function. Here, we focus on two main types of MC-based methods: path sampling methods and ray tracing simulations. For the path sampling method, a more computationally efficient sampling algorithm is proposed based on the analytical solution of the average distance phonons can travel before a collision. The physical meaning of the path sampling method is rigorously given for the first time by comparing to the analytical solution of the BTE for symmetric structures. Several limitations of the path sampling method are discussed based on assumptions in the derivation. Ray tracing simulations are well defined when a converged boundary mean free path (MFP) can be found. However, convergence is not guaranteed for arbitrary structures. More generally, we propose a modified formula to approximate the full-range suppression function with a characteristic length, which is determined by fitting to the calculated suppression function at selected MFPs. Ultimately the accuracy of each calculated suppression function is evaluated by comparing the calculated thermal conductivity accumulation function for nanostructures including thin films, nanowires, and anisotropic modulated nanostructures. Our results provide guidance for selecting the appropriate techniques for calculating the suppression function and thereby predicting the thermal conductivity of nanostructures.

4.1 Introduction

Thermal transport in nanostructured materials is critical for many applications including modern electronics, thermoelectrics, and thermal management.[1,72,73] Phonons are dominant heat carriers in semiconducting and insulating materials.[43] For decades, phonon transport in nanostructures has been both experimentally and numerically investigated.[2,74–77] Previous experiments demonstrated the reduced thermal conductivity (k) of thin films (TFs),[19,40,78]

nanowires (NWs),[79–81] and nanoporous structures.[3,35,82–84] Numerous models based on the Boltzmann Transport Equation (BTE) have been developed to understand the reduction of *k*.[50,52,85–91] The general form for the BTE in the relaxation time approximation is

$$\frac{\partial f}{\partial t} + \mathbf{v} \cdot \nabla_{\mathbf{r}} f = -\frac{f_{DE}}{\tau} \tag{4.1}$$

where f is the distribution function, t is the time, $\boldsymbol{v}$ is the phonon group velocity, $\boldsymbol{r}$ is the position, τ is the relaxation time, and $f_{DE} = f - f_{BE}$ is the small departure from the Bose-Einstein distribution f_{BE}. Assuming isotropic dispersion, a simplified solution of the BTE is generally used to calculate the thermal conductivity of a nanostructure as[92]

$$k = \frac{1}{3}\sum_j \int C v_j S(\overline{\Lambda}_{bulk,j}, L_c)\overline{\Lambda}_{bulk,j} d\omega \tag{4.2}$$

where C is the volumetric specific heat capacity per unit frequency, v_j is the group velocity, $\overline{\Lambda}_{bulk,j}$ is the bulk phonon mean free path (MFP), L_c is the characteristic length, S is the suppression function of thermal conductivity contribution by each mode, and j represents the phonon branches.

The thermal conductivity integral model based on the suppression function has had considerable success in explaining the decreased k in nanostructures. However, the suppression function is analytically defined only for some simple structures (*e.g.*, TFs and NWs). For arbitrary nanostructures, Monte Carlo (MC) -based methods have been developed to determine the nanostructure-dependent MFP, $\overline{\Lambda}_{nano,j}$, including the effect of phonon-boundary scattering, which can be used for calculating the nanostructure thermal conductivity as

$$k = \frac{1}{3}\sum_j \int C v_j \overline{\Lambda}_{nano,j} d\omega \tag{4.3}$$

McGaughey and Jain[91] developed a free path sampling method and applied it to the thermal conductivity calculation of a polycrystalline bulk material and a thin film. Marconnet *et al.*[5] developed a similar random path sampling technique to investigate phonon transport in periodically porous silicon nanowires. The path sampling technique simulates phonon propagation from a random position until a scattering event, while ray tracing simulations by Hori *et al.*[87] calculated the boundary scattering MFP based on a transmission model and determined the

effective MFP using Matthiessen's rule.[93] Further, Lee *et al.*[84] investigated phonon backscattering in silicon nanomeshes using the ray tracing method. Recently, Parrish *et al.*[94] compared calculations of k for silicon nanowires and nanoporous films by the MC-based methods highlighting the difference in the calculated phonon MFP-dependent k accumulation. However, in addition to discussions based on simulations of specific structures, there is a need to investigate the physical significance of the MC-based MFP calculation methods and understand the basic difference of these models in calculating thermal conductivity.

Here, we focus on two main types of MC-based methods for calculating the suppression function: the path sampling method and ray tracing simulations. First, we propose a more efficient sampling method based on the analytical solution of the average distance phonons can travel before a collision. To evaluate the applicability of the path sampling method, we interrogate the physical meaning by comparing to the analytical solution of the BTE for symmetric structures. Next, the ray tracing simulation method is evaluated and we propose a modified analytical formula to approximate the full-range suppression function with a characteristic length, which is determined by fitting to the calculated suppression function at selective MFPs. Further, we compare the calculated suppression function and thermal conductivity accumulation in silicon nanostructures including TFs, NWs, and anisotropic modulated nanostructures. To facilitate the discussion of the suppression due to phonon-boundary scattering alone, isotropic bulk phonon properties are assumed in the calculations and nanostructures large enough of bulk-like phonon properties are considered.[95,96] For the calculation of thermal conductivity accumulation, we use the MFP dependent thermal conductivity contribution by first principle calculations of bulk silicon at 300 K from Esfarjani *et al.*,[97] except for the thickness modulated TFs where the same input as our previous work[98] is used for a consistent comparison. The calculations are verified by comparing to analytical solutions for simple structures[36,37,99] and to published BTE-based simulations for complex nanostructures.[71,98] The results shed light on the appropriate MC methods for the accurate calculation of thermal conductivity of nanostructures.

4.2 Approach

4.2.1 The Effective Mean Free Path

When working with nano- and microstructures, there are two common methods of incorporating boundary effects into the mean free path: Matthiessen's Rule and the Suppression Function. Matthiessen's rule assumes scattering events are independent and incorporates boundary scattering along with intrinsic scattering processes as $\overline{\Lambda}_{nano,j} = 1/(\overline{\Lambda}_{bulk,j}^{-1} + \overline{\Lambda}_{B}^{-1})$ to find an average distance between collisions, where $\overline{\Lambda}_{B}$ is the boundary scattering MFP. In contrast, the suppression function essentially reduces the bulk MFP by a size-dependent parameter *S*: $\overline{\Lambda}_{nano,j} = S\overline{\Lambda}_{bulk,j}$. Here, for the path sampling simulation, we focus on the definition based on the suppression function as the nanostructure MFP is determined by the bulk MFP and the nanostructure geometry. For the ray tracing method, an analogy is made between the two approaches.

Further, note that the definition of "mean" is important to the understanding and use of the thermal conductivity integrals. Specifically, Eqn. (4.3) is not necessarily equivalent to Eqn. (4.2) if the $\overline{\Lambda}_{nano,j}$ follows the general definition of MFP, *i.e.*, the average distance traveled by a phonon between successive collisions over all directions. For example, the thermal conductivity of thin films is anisotropic with different values in the in-plane and the cross-plane direction, while the MFP calculated by modeling the phonons as particles is an average over all directions. To capture the directional variations in *k* using Eqn. (4.3), the MFP in these models should be an average of the distance traveled by phonons weighted by the directional thermal conductivity contribution. In this work, we define the effective MFP, $\overline{\Lambda}_{eff,j}$, to avoid confusion with the definition of MFP in isotropic mediums. The $\overline{\Lambda}_{eff,j}$ can be expressed as

$$\overline{\Lambda}_{eff,j} = \mathbf{S}(\overline{\Lambda}_{bulk,j}, L_c) \cdot \overline{\Lambda}_{bulk,j} \tag{4.4}$$

where $\boldsymbol{S}$ now becomes a suppression function vector along with the directionality. Using this terminology, the $\overline{\Lambda}_{nano,j}$ is an equally-weighted average of the travel distance over all directions, while the $\overline{\Lambda}_{eff,j}$ is an average weighted by each phonon's directional thermal conductivity

contribution. The difference in $\overline{\Lambda}_{nano,j}$ and $\overline{\Lambda}_{eff,j}$ highlights the importance of including the directional contribution for accurate prediction of thermal conductivity.

Additionally, an implicit assumption in the treatment is that phonon modes are nearly independent, and thus the suppression of each mode can be calculated separately. This assumption has to do with the calculation of temperature based on equilibrium or local equilibrium conditions of all phonon modes.[100] For diffusive heat conduction, the temperature distribution can be known via Fourier's law, *e.g.*, a linear temperature gradient for heat conduction across symmetric structures. The mode-dependent suppression by a separate treatment of each phonon mode combined with the predicted temperature distribution easily yields the suppressed thermal conductivity contribution. In contrast, to calculate the mode-dependent thermal conductivity contribution in ballistic transport, the temperature must be calculated by solving the mode-dependent BTE, which is not resolved in both the MC methods discussed here. Without the temperature calculated by all modes, the suppressed thermal conductivity cannot be determined from the suppression of each individual mode alone. Thus, treating different phonon modes separately in the ballistic regime is not sufficient for calculating the mode-dependent thermal conductivity. Further, the separate treatment implies inconsistent physics for ballistic phonon transport. A separate treatment of small-MFP phonons indicates diffusive transport for these modes similar to Fourier's law, while the treatment of long-MFP phonons suggests ballistic transport.

4.2.2 Path Sampling Method

The random path sampling method is based on simulations of a single scattering event (phonon-boundary scattering or intrinsic phonon-phonon scattering) for phonons randomly sampled within a structure. Briefly, the free path sampled from the distribution of bulk MFPs is truncated by the travel distance from the origin to the nearest scattering point, *i.e.* the potential point of collision with boundaries. For each nanostructure, the MFP is an average of the free paths generated by the sampling process. In previous work, at least 1000 free paths need to be sampled to give the effective MFP for each bulk MFP.[91]

Rather than sampling free paths from a Poisson distribution for each MFP as in past work,[91,94] we propose a more computationally efficient sampling method using the analytically determined mean distance that a phonon can travel without a collision from the origin point *O* to

the nearest point *P* on the surface. For diffusive phonon-boundary scattering, the MFP for a phonon traveled along the direction ***OP*** can be calculated as $\overline{\Lambda}_{bulk}(1-e^{-\overline{OP}/\overline{\Lambda}_{bulk}})$.[99] This treatment significantly speeds up computation compared to the previous procedure that repeated the sampling step many times to give the converged nanostructure MFP.[91] Figure 4.1(a) demonstrates the difference between these two sampling algorithms. Obviously, the computational efficiency is greatly improved as the nanostructure free path is analytically determined in the proposed sampling algorithm.

More importantly, we interrogate the applicability of the path sampling method by giving a physical understanding to this method. Basically, this method originates from an intuitive understanding of phonon MFP without a rigorous derivation. To understand the physics, we compare the path sampling method to a particular solution of the BTE in symmetric structures, *e.g.*, TFs and NWs, where some knowledge of the temperature distribution can be determined directly from the symmetry.[43] The BTE in steady state can be expanded as

$$v_x\frac{\partial f_{BE}}{\partial x}+v_y\frac{\partial f_{BE}}{\partial y}+v_z\frac{\partial f_{BE}}{\partial z}+v_x\frac{\partial f_{DE}}{\partial x}+v_y\frac{\partial f_{DE}}{\partial y}+v_z\frac{\partial f_{DE}}{\partial z}=-\frac{f_{DE}}{\tau} \tag{4.5}$$

where v_x, v_y, and v_z are the phonon group velocity components along the *x*, *y*, and *z* direction, respectively. Consider 1D heat conduction along the *x* direction, the BTE can be simplified to a first-order differential equation with the assumed temperature distribution[99] if

$$\frac{\partial}{\partial x}\left(v_y\frac{\partial f_{BE}}{\partial y}+v_z\frac{\partial f_{BE}}{\partial z}\right)=0 \tag{4.6}$$

This condition is easily satisfied for a 1D temperature gradient applied along a symmetric structure, *e.g.*, a long film or wire of uniform cross-sections, as each cross-section perpendicular to the prescribed heat flow direction must have the same temperature and thus the same equilibrium distribution. From the simplified BTE, particular solutions have been obtained for phonon transport in thin films[36,37] and nanowires. The suppression function for symmetric structures with a cross-sectional area A_c as derived by Chambers[99] is

$$S(\overline{\Lambda}_{bulk,j})=\frac{3}{4\pi A_c}\iint(1-e^{-\overline{OP}/\overline{\Lambda}_{bulk,j}})\cos^2\theta d\Omega dA_c \tag{4.7}$$

where $\overline{OP}$ is the distance from a point O on the cross-section to a point P on the surface, $d\Omega$ is an element of solid angle along $\overline{OP}$, and θ is the angle between $\overline{OP}$ and the thermal gradient. The $\overline{\Lambda}_{eff,j}$ calculated using Eqn. (4.4) and Eqn. (4.7) is

$$\overline{\Lambda}_{eff,j} = \frac{3}{4\pi A_c} \iint \overline{\Lambda}_{bulk,j} \left(1 - e^{-\overline{OP}/\overline{\Lambda}_{bulk,j}}\right) \cos^2\theta \, d\Omega \, dA_c \tag{4.8}$$

A comparison of this derived formula and the path sampling method demonstrates the equivalence between the method and the solution of Eqn. (4.8). Note that Eqns. (4.7) and (4.8) are not derived from the general solution of the BTE, but from a specific solution for the simplified BTE when the condition described by Eqn. (4.6) is met.[99] In other words, Eqn. (4.8) has nothing to do with the BTE if Eqn. (4.6) is not satisfied. Equivalently, the path sampling method is meaningless in this situation. Therefore, the applicability of the path sampling method can be judged by Eqn. (4.6). Here, this condition is referred to as the symmetry condition since the condition in Eqn. (4.6) depends on symmetry of the structures, *i.e.*, all the cross-sections along a specific direction can be planes of symmetry and the equilibrium distribution varies in the only direction.

(a)

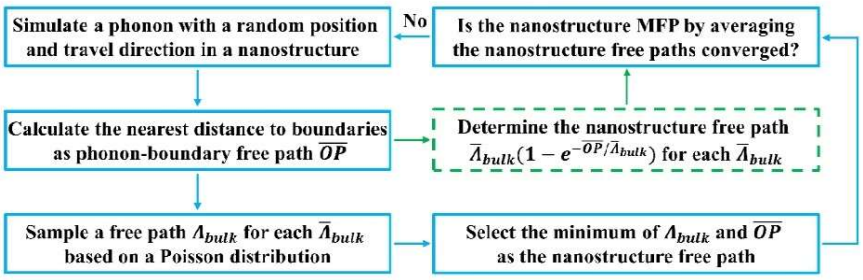

(b)

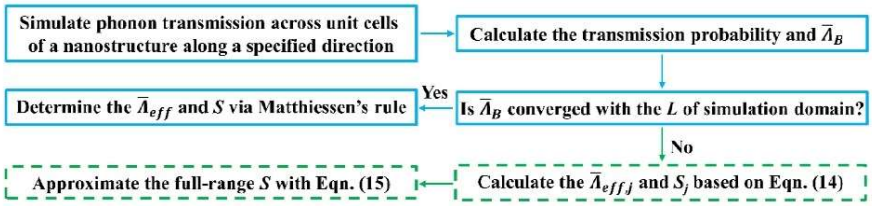

Figure 4.1: Process flow for (a) the path sampling method and (b) ray tracing simulations. Steps used in previous algorithms are outlined in blue, while the extensions applied in this paper are outlined with green dashed lines. For the path sampling method, compared to sampling free

paths from a Poisson distribution for each MFP, the computational efficiency is greatly improved using the analytically determined nanostructure free paths. For the ray tracing approach, with the proposed approximation, the method can be applied to more arbitrary structures where no converged boundary MFP can be found.

The suppression function calculated by the modified path sampling method is discussed in Section III for various nanostructures. The applicability of the path sampling method is predicted by Eqn. (4.6). The accuracy of the calculated suppression function and the prediction is determined by comparing to the analytical solutions or published BTE-based simulation results. Such a comparison reveals the limitation of the path sampling method when applied in certain structures, and the symmetry condition can be used to judge whether this method is appropriate in specific structures.

4.2.3 Ray Tracing Method

The ray tracing method calculates a geometry-dependent phonon-boundary scattering MFP based on ballistic transmission. When only ballistic transport is considered, the mode-dependent thermal conductivity is

$$k_j = \frac{1}{3} C v_j \overline{\Lambda}_B \tag{4.9}$$

and the thermal conductivity can be derived from the Landauer formula as[100]

$$k_j = fL \cdot \frac{1}{2} C v_j \int_0^{\pi/2} \tau_{12}(\theta) \cos\theta \sin\theta d\theta \tag{4.10}$$

where f is the geometry correction factor, L is the length of the nanostructure, θ is the incidence angle, and τ_{12} is the phonon transmission probability. Note that the f is generally calculated using Fourier's law, which is strictly valid for diffusive transport only. From Eqn. (4.9) and (4.10), the $\overline{\Lambda}_B$ can be expressed as[87]

$$\overline{\Lambda}_B = \frac{3}{2} fL \int_0^{\pi/2} \tau_{12}(\theta) \cos\theta \sin\theta d\theta \tag{4.11}$$

Assuming independent intrinsic and boundary scatterings, the effective MFP is determined via Matthiessen's rule:[93]

$$\overline{\Lambda}_{eff,j}^{-1} = \overline{\Lambda}_{bulk,j}^{-1} + \overline{\Lambda}_B^{-1} \tag{4.12}$$

The calculation of $\overline{\Lambda}_{eff}$ and $\overline{\Lambda}_B$ is meaningful when it converges with the length of the nanostructures, which is the case when boundary scattering is dominant over other scattering mechanisms. The suppression function can be written with the geometry-dependent $\overline{\Lambda}_B$ for all modes as

$$S_j(\overline{\Lambda}_{bulk,j}) = \frac{1}{1+\overline{\Lambda}_{bulk,j}/\overline{\Lambda}_B} \tag{4.13}$$

However, convergence is not guaranteed for phonon transport in arbitrary nanostructures, *e.g.*, in-plane transport in thin films. A more general method is to calculate the transmission probability considering the intrinsic phonon scattering, and the $\overline{\Lambda}_{eff,j}$ corresponding to $\overline{\Lambda}_{bulk,j}$ is[87]

$$\overline{\Lambda}_{eff,j} = \frac{3}{2} fL \int_0^{\pi/2} \tau_{12}(\overline{\Lambda}_{bulk,j}, \theta) \cos\theta \sin\theta d\theta \tag{4.14}$$

To calculate the suppression function with fine resolution across a wide range of MFPs, ray tracing simulations need to be performed for a large number of MFPs. The mode-dependent simulation becomes much more computationally expensive compared to the mode-independent calculation of $\overline{\Lambda}_B$.

Thus, we propose that a characteristic length L_c can be determined by fitting to the calculated suppression function at several selective MFPs around the minimum confined size in nanostructures. This treatment agrees with the fact that boundary scattering MFP for nanostructures generally corresponds to the confined size, *e.g.*, thickness for TFs,[31] diameter for NWs,[99] and distance between pore boundaries for nanoporous structures.[5] Therefore, a good sensitivity to L_c can be expected by fitting to the suppression function around the confined size rather than to full range of possible MFPs to improve computational efficiency. Given that for phonons with short MFPs the suppression function does not always trend towards 1 for complex structures as reported in previous BTE-based simulations,[71,101] we approximate the suppression function as

$$S_j(\overline{\Lambda}_{bulk,j}) = \frac{S_j(\overline{\Lambda}_{bulk,j} \to 0)}{1+\overline{\Lambda}_{bulk,j}/L_c} \tag{4.15}$$

The suppression function approximated by Eqn. (4.15) has a similar form as Eqn. (4.13). It can be regarded as an extension of Eqn. (4.13) with a corrected $S_j(\overline{\Lambda}_{bulk,j} \to 0)$ when $S_j(\overline{\Lambda}_{bulk,j} \to 0) \neq 1$. The same physics remain in this approximation, *i.e.*, intrinsic and boundary scatterings are still treated independently as shown in the denominator of Eqn. (4.15). Mathematically, the correction of $S_j(\overline{\Lambda}_{bulk,j} \to 0)$ allows a better fitting of the calculated suppression functions compared to Eqn. (4.13). With this approximation, the ray tracing method can be applied to more arbitrary structures. Figure 4.1(b) outlines the modified algorithm with the additional steps that extend its applicability compared to the previous ray tracing simulations.

In this case study, we calculate the suppression function by ray tracing simulations for various nanostructures. The $\overline{\Lambda}_B$ is determined from Eqn. (4.11) for nanostructures with a converged boundary scattering MFP, otherwise the characteristic length L_c is calculated by fitting with Eqn. (4.15). The calculation results are compared to the analytical solutions or published BTE-based simulation results. The question to be answered is whether the mode-independent boundary MFP or characteristic length is sufficient to obtain the accurate mode-dependent suppression function and thereby accurate thermal conductivity predictions.

4.3 Case Study: Phonon Transport in Si Nanostructures

4.3.1 Thin Films and Nanowires

In- and cross-plane phonon transport in thin films have been extensively investigated based on the BTE. Here, we consider phonon conduction suppressed due to the decreased thickness of TFs, while the lengths in other dimensions are assumed to be infinite. For the in-plane transport, the Fuchs-Sondheimer (F-S) solution[36,37] or the Chambers solution[99] can be used to analytically determine the suppression function. We compare the suppression function calculated by the MC techniques to the analytical solution. Figure 4.2(a) shows an excellent agreement between the analytical solution and the suppression function by the proposed path sampling method, while a converged $\overline{\Lambda}_B$ by the ray tracing method cannot be found from Eqn. (4.11). The suppression function calculated at selective MFPs based on Eqn. (4.14) agrees well with the F-S solution. Thus, although the $\overline{\Lambda}_B$ does not converge with the length of simulation domain, fitting

the ray tracing results at several selective MFPs to Eqn. (4.15) gives $L_c / d = 2.33$, where d is the film thickness. A reasonable agreement is observed for all phonon MFPs between the analytical solution and the suppression function calculated using $L_c / d = 2.33$. This term corresponds to the so-called boundary scattering term in literature, which has generally been used as a fitting parameter to match the temperature-dependent thermal conductivity experimental data. This ultimately depends on the accuracy of the experimental results and other parameters in the fitting model. Here, we show that a well-defined L_c can be determined by fitting to the suppression function, and its accuracy in calculating in-plane k of TFs is shown in Figure 4.2(b).

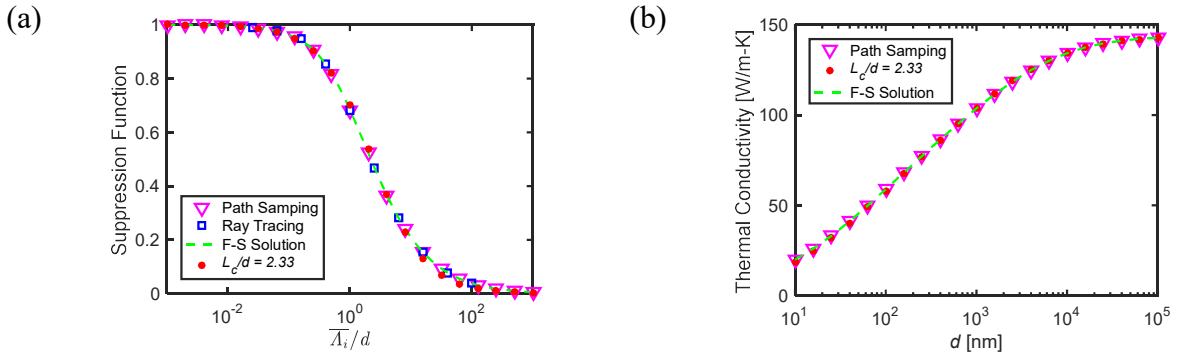

Figure 4.2: (a) Suppression function for in-plane phonon transport in TFs. The suppression function calculated by the MC techniques agrees well with the Fuchs-Sondheimer (F-S) solution. Though a converged $\overline{\Lambda}_B$ does not exist, a reasonable agreement is observed for all phonon MFPs between the analytical solution and the suppression function calculated using L_c / d =2.33. (b) Thickness-dependent in-plane thermal conductivity of silicon TFs. With the suppression function, we calculate the k using the MFP-dependent thermal conductivity contribution by Esfarjani et al.[97] A good agreement is observed for in-plane k of TFs across a range of thicknesses, which verifies the accuracy of the suppression function approximated using the characteristic length.

As for the cross-plane transport, Figure 4.3(a) shows a comparison between the semi-analytical BTE solution[102] and the suppression function by the MC methods. Both the MC methods gives the same well-known limit[103] $S = \overline{\Lambda}_B / d = 3/4$ for long phonon MFPs. The suppression function calculated by the MC methods agrees well with the solution for long mean free paths ($\overline{\Lambda}_i / d$ >1). The deviation for short mean free paths ($\overline{\Lambda}_i / d$ <1) is due to the separate treatment of each mode, which means the impact of ballistic effect on phonons of small MFPs is not considered in the MC techniques. This is unphysical as temperature is defined based on equilibrium or local equilibrium conditions of all phonon modes.[100] Fourier's law itself cannot

capture the temperature slip at the boundaries and the nonlinear temperature profile across the film. The impact of the deviation for $\overline{\Lambda}_i / d < 1$ on calculating the k of extremely thin films is negligible as little heat is conducted by the modes of such small MFPs. For relatively thick films, the deviation has a larger impact on the calculation of k, *e.g.*, cross-plane thermal conductivity of silicon TFs as shown in Figure 4.3(b), which is critical for predicting the onset of size effect in thermal conductivity of TFs.

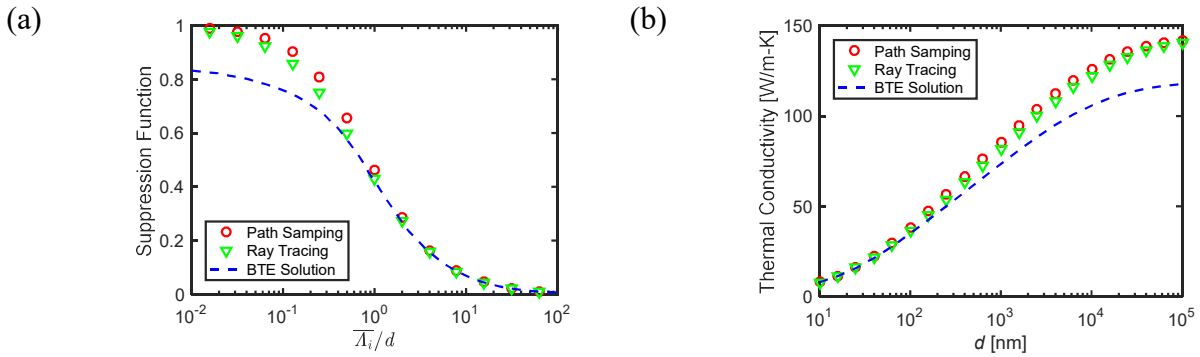

Figure 4.3: (a) Suppression function for cross-plane phonon transport in TFs. The suppression function calculated by the MC methods agrees well with the published BTE-based solution[102] for $\overline{\Lambda}_i / d > 1$, and the deviation for $\overline{\Lambda}_i / d < 1$ is due to the separate treatment of each mode. (b) Thickness-dependent cross-plane thermal conductivity of silicon TFs. With the suppression function, we calculate the k using the MFP-dependent thermal conductivity contribution by Esfarjani *et al.*[97] The deviation of the suppression function for $\overline{\Lambda}_i / d > 1$ causes the deviation of k for relatively thick films.

Next, the suppression function for square nanowires is calculated using the MC methods as shown in Figure 4.4(a). Similarly, we consider sufficiently long nanowires where axial heat conduction is in the diffusive regime. The good agreement is not surprising considering the symmetry and the converged $\overline{\Lambda}_B$. Both the MC techniques give the same boundary scattering MFP as the Casimir limit:[104] $\overline{\Lambda}_B / D = 1.12$, where D is the side width of the square nanowire. Further, Figure 4.4(b) demonstrates the k of silicon NWs calculated using the suppression function across a range of side widths.

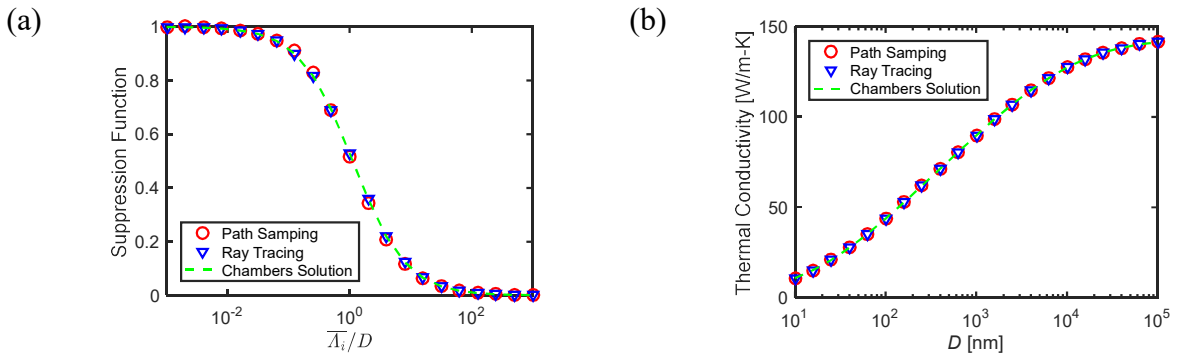

Figure 4.4: (a) Suppression function for axial phonon transport in NWs. A good agreement is observed between the MC techniques, and both the MC calculations give the same boundary scattering MFP as the Casimir limit $\overline{\Lambda}_B / D$ =1.12. (b) Side width-dependent thermal conductivity of silicon NWs. With the suppression function, we calculate the *k* using the MFP-dependent thermal conductivity contribution by Esfarjani *et al*.[97]

4.3.2 Nanostructured Thin Films

Phonon transport in nanostructured thin films has been one of the major topics of nanoscale heat transfer in past two decades. There have been discussions whether the coherent phonon transport causes the significantly reduced thermal conductivity.[2,3,5,35,55,84,94,105] Recently, more experimental and simulation results[83,84,94] supported that the particle-based model only can explain the decrease of thermal conductivity in silicon nanostructures, which implies that coherent transport is not dominant in the measurement regime. Here, we investigate the suppression function for phonon transport in thickness-modulated thin films[98] and nanoporous thin films[71] by the MC methods. Note that for these complex nanostructures the symmetry condition is not naturally satisfied. Therefore, the particular solution of the BTE equivalent to the path sampling method may not exist due to the lack of symmetry.

Figure 4.5(b) presents the suppression function along the *x* and *y* direction for thickness modulated TFs (see Figure 4.5(a)). The suppression function by the ray tracing simulation using Eqn. (4.14) agrees well with the suppression function calculated in our previous work by solving the BTE.[98] As for the path sampling method, a good agreement is observed for the suppression function along the *y* direction where the cross-section is uniform along that direction, while the suppression function along the *x* direction with the modulated thicknesses deviates from the BTE result. The calculation results can be understood by examining the symmetry condition. This condition is satisfied for heat conduction along the *y* direction due to the same cross-section extruded along the y-direction. Therefore, the particular solution of the BTE can be solved by the

path sampling method. However, the symmetry condition is not met in the x direction due to the nonuniform cross-sections, and thus the path sampling method is devoid of physical significance. Figure 4.5 (c) and (d) demonstrate the thermal conductivity accumulation calculated using the different suppression functions. As a converged $\overline{\Lambda}_B$ cannot be found in the structure, we approximate the calculated suppression function with Eqn. (4.15) for calculating the full-range suppression function. A reasonable agreement is observed between the k accumulation function calculated using the approximation and the BTE-based simulation. As for the path sampling method, the agreement to the BTE result depends on whether the symmetry condition is satisfied in the specified direction, *e.g.*, a large deviation along the x direction and a good agreement in the y direction.

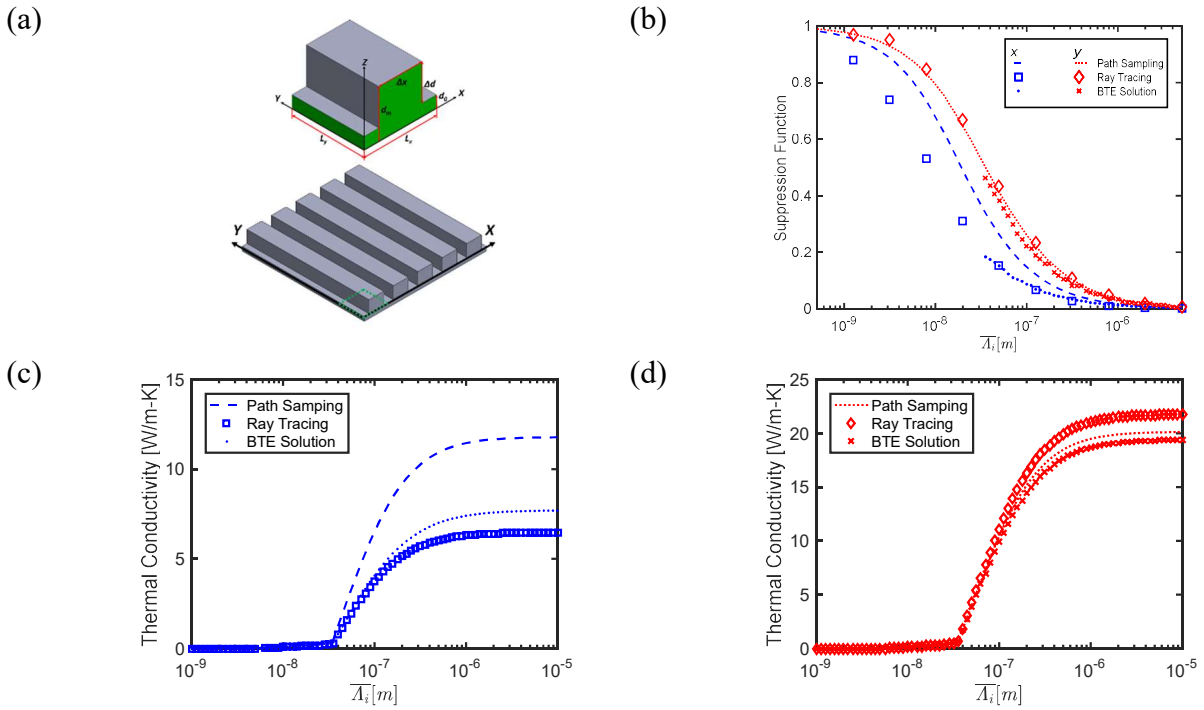

Figure 4.5: (a) Schematic of the thickness modulated TFs and a unit cell of size L_x=L_y=30 nm, Δx=24 nm, d_0=5 nm, and d_m=50 nm. (b) Suppression function along the x and y direction for the thickness modulated TF. The suppression function along the x and y direction by ray tracing simulation agrees well with the published BTE-based simulation.[98] As for the path sampling method, the good agreement is observed in the y direction only, while there are large deviations for the values along the x direction. The impact of the suppression on calculating the thermal conductivity contribution is shown in (c) and (d) for the x and y direction, respectively. For a consistent comparison, the same input as our previous work[98] is used for the calculation of the k contribution, and the thermal conductivity is corrected with geometry factors calculated using COMSOL. Panel (a) reproduced and modified from our previous work with permission.

In 2D nanoporous thin films with anisotropic pores[71] as shown in Figure 4.6(a), symmetry does not exist in the *x* or *y* direction. Figure 4.6(b) displays the comparison between the suppression function calculated by the MC techniques and the published BTE result.[71] It is not surprising to observe the deviation between the suppression function calculated by the path sampling method and the BTE result as the particular solution equivalent to the path sampling method does not exist due to the loss of symmetry. In contrast, a reasonable agreement is observed between the suppression function calculated by the ray tracing method and the BTE result. Similarly, a characteristic length is determined using Eqn. (4.15) for calculating the full-range suppression as a converged $\overline{\Lambda}_B$ cannot be found for this system. Note that the *x*-direction suppression function calculated by the ray tracing simulation deviates from the BTE result for phonons of $\overline{\Lambda}_{bulk} < 50$ nm, which can cause a large deviation of thermal conductivity for materials with most heat conducted by phonons of $\overline{\Lambda}_{bulk}$ around or smaller than this critical value. As phonon MFPs in silicon are around 1 μm, the deviation will not cause much errors in calculating thermal conductivity accumulation for silicon nanostructures as shown in Figure 4.6 (c) and (d). As for the path sampling method, the *k* accumulation along the *x* direction deviates from the BTE result. The deviation of the *k* accumulation along the *y* direction is relatively small due to the reasonable agreement of the suppression function for long MFPs.

(a)

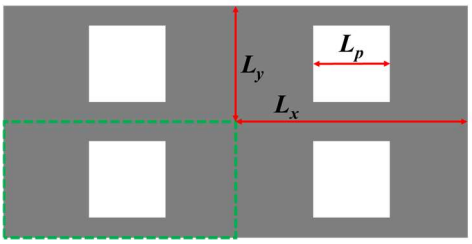

(b)

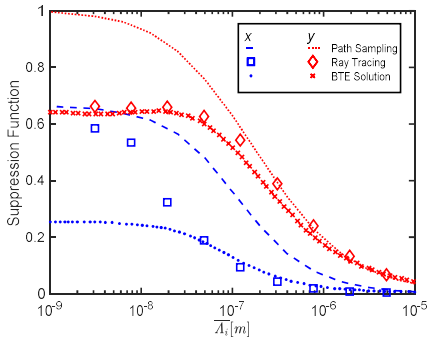

(c)

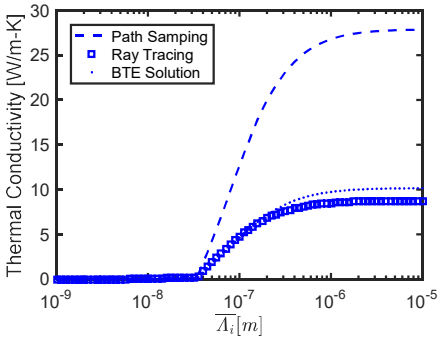

(d)

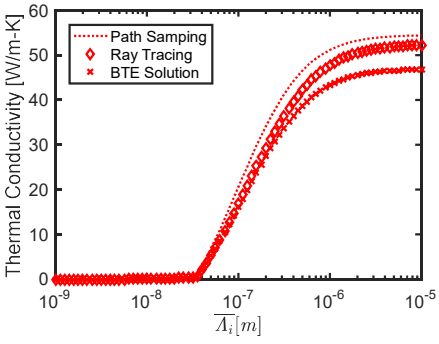

Figure 4.6: (a) Schematic of the 2D nanoporous thin film with anisotropic pores and a unit cell of size L_x= 173.205 nm, L_y=57.735 nm and L_p=50 nm. (b) Suppression function along the x and y direction for the 2D anisotropic porous TF. The suppression function along the x and y direction by ray tracing simulation agrees well with the published BTE-based simulation.[71] For the path sampling method, a large deviation along both the x and y direction is observed as the particular solution equivalent to the path sampling method does not exist in the asymmetric structure. The impact of the suppression on calculating the thermal conductivity contribution is shown in (c) and (d) for the x and y direction, respectively. We calculate the k contribution using the MFP-dependent thermal conductivity contribution by Esfarjani *et al*,[97] and the thermal conductivity is corrected with geometry factors calculated with COMSOL.

4.4 Summary

Two main types of MC techniques, path sampling method and ray tracing simulation, are evaluated for calculating the suppression function and thermal conductivity accumulation for various nanostructures. The physical meaning of the path sampling method is elucidated by comparing to the analytical solution of the BTE for symmetric structures. An efficient sampling method, based on the analytical solution of the average distance phonons can travel before a collision, is used to calculate the effective mean free path. However, the particular solution of the BTE may not exist as required conditions on the temperature gradient within the cross-section are not satisfied in complex nanostructures, which suggests the limitation of the path sampling method in complex structures. Ray tracing simulations are more general due to the nature of transmission. The directional contribution is considered by counting the transmitted phonons. Though a converged boundary MFP does not always exist, we propose a modified analytical model to approximate the full-range suppression function with a single characteristic length. The characteristic length is determined by fitting to the calculated suppression function and a reasonable agreement to the BTE result is observed in the case study of several common nanostructures. In addition, it should be noted that both the MC techniques treat each mode separately, and thus the impact of ballistic effect on phonons of small MFPs cannot be incorporated in these models, *e.g.*, phonon transport in cross-plane TFs and anisotropic porous TFs. Ultimately, this work provides insight into the suppression function of phonon transport in nanostructures by MC techniques, which is instructive for the choice of MC methods in calculating thermal conductivity of different nanostructures.

5. STRAIN ENGINEERING THERMAL CONDUCTION

Beginning around the 1960s, much theoretical and experimental work on stress/strain dependent thermal conductivity of bulk semiconductors was conducted at low temperatures [106,107]. This prior work focused on the impact of stress/strain on electron-phonon interaction in doped semiconductors and its impact on thermal conductivity. Recently, strain engineering of thermal transport has renewed interest with the increasing importance of MEMS technologies and other novel optical and electronic devices which leverage strain-controlled films for functionality. Experimental data on the impact of strain on thermal transport in thin films is limited and sometimes conflicting. In part this is due to challenges in simultaneous measurement of thermal conductivity and control of mechanical strain at the length scales relevant to MEMS applications and modern devices. A systematic study of strain-dependent thermal conductivity is needed to shed light on thermal transport in strained thin films. Understanding thermal transport in strained micro/nanostructured materials is critical for applications related to flexible electronics and other devices with significant thermomechanical stresses. This chapter explores strain engineering of the thermal conductivity of polymer-supported metal films and multi-layer graphene films. Suspended samples on a flexible substrate combined with a custom-built mechanical stage enables strain dependent thermal conductivity characterization using the electrothermal method. Characterization of the strain-dependent thermal conductivity of materials enables us to probe the underlying thermal transport physics.

5.1 Thermal Conductivity of Extremely Strained Au-on-Polyimide Films

Flexible electronic devices typically contain inorganic films on a polymer substrate and it of significant practical and theoretical interest to investigate various properties of such structures. Indeed, the mechanical properties of polymer-supported metal films have been extensively investigated, *e.g.*, characterizing the fracture strain. Supported metal films can be stretched beyond a strain of 20-50 %, while the fracture strain of free-standing metal films is only ~1%.[108–111] In the supported structure, the strain in the metal film is delocalized and thus it can be stretched to greater lengths. Though the mechanical properties are well characterized, the thermal conductivity of extremely strained metal-on-polymer structures has been scarcely investigated.

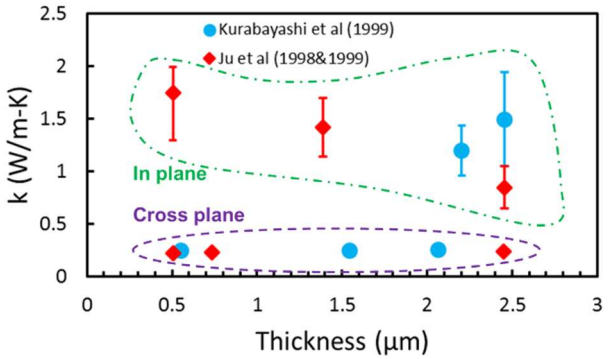

Figure 5.1: In-plane and cross-plane thermal conductivity of polyimide thin films from the literature. [112,113] The thermal conductivity anisotropy is attributed to the alignment of the polymer chains.

Previous thermal conductivity measurements for strain-free polyimide films demonstrated a thermal conductivity anisotropy when comparing the in-plane k to the cross-plane k. Figure 5.1 shows the in-plane k is 1-2 W/m-K and the cross-plane k is ~0.2 W/m-K. The thermal conductivity anisotropy is typically attributed to the orientation of the polymer chains.[112,113] Here, we perform an experimental study of thermal conductivity in extremely strained polyimide-supported Au nanofilms (100 nm Au on 25.4 μm polyimide). The 25.4 μm polyimide film (Kapton by DuPont) is ultrasonically cleaned with toluene, acetone, and methanol. Then, 100 nm Au layer and 5 nm Cr adhesion layer are deposited on the polyimide using an E-beam evaporator. The Au-on-polyimide composite film is cut into strips with desired length-to-width ratios for the mechanical stage (see Figure 5.2(a)). The electrothermal measurement is performed in a vacuum chamber to minimize convection losses. Figure 5.2 (b) and (c) shows the calibrated electrical resistance *vs.* temperature and an example of resistance variation *vs.* square of current, respectively. The measured in-plane thermal conductivity of the polyimide free of strain by this method is k_0 = 1.9 ± 0.1 W/m-K, which agrees well with the prior results.

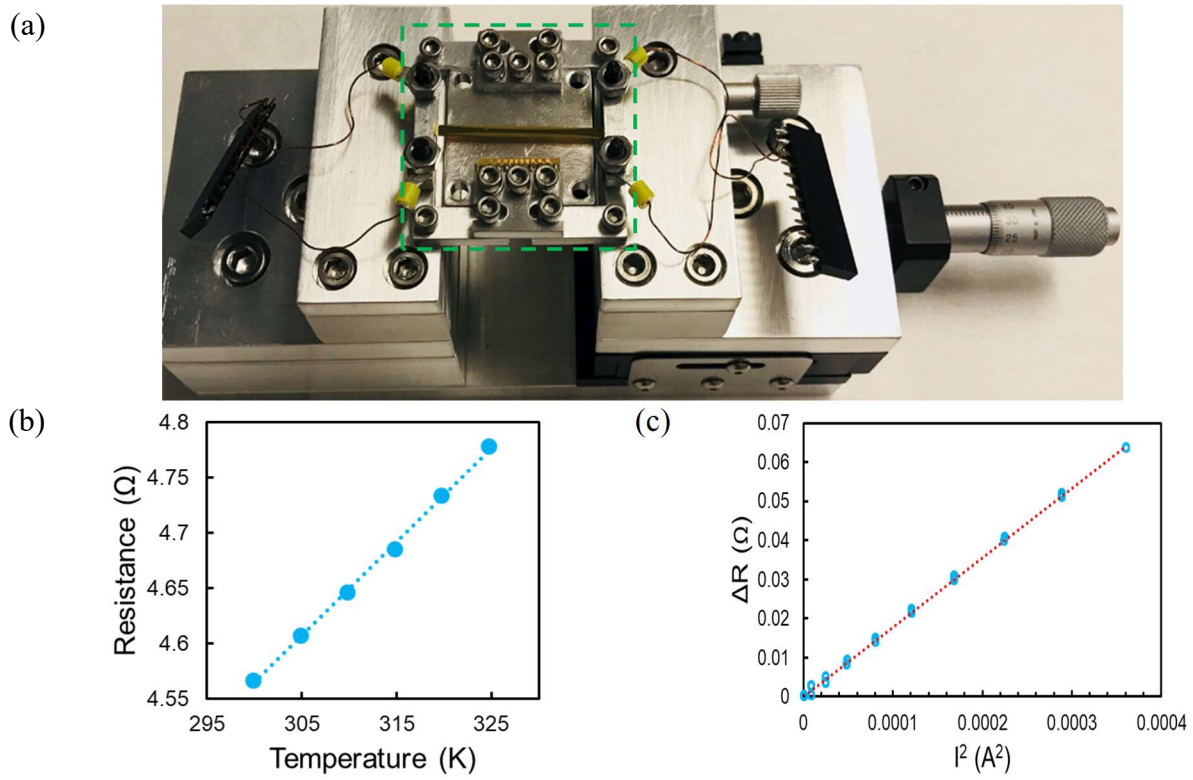

Figure 5.2: (a) The Au-on-polyimide strip with appropriate length-to-width ratios on the mechanical stage. A micrometer is used to control the strain of the strip. After strain is applied, the portion outlined in green detaches from the micrometer stage and is attached to the cryostat cold finger for temperature-controlled measurements. (b) The calibrated electrical resistance as a function of temperature for the free-strain Au-on-polyimide strip. (c) The electrothermal response, resistance variation as a function of square of current, for the free-strain Au-on-polyimide strip.

Further, we systemically investigate the impact of strain on the electrical resistance, temperature coefficient of resistance (TCR), and thermal conductivity. Figure 5.3(a) demonstrates the increased electrical resistance with the tensile strain. Quantitatively, the electrical resistance varies with the deformation as $(L/L_0)^2$, which agrees with the calculated electrical resistance assuming a constant volume of the metal layer during the deformation. The variation indicates that microcracks in the metal layer is not appreciable, or the variation will deviate from $R/R_0 = (L/L_0)^2$. Figure 5.3(b) shows that the TCR decreases in a certain strain range and a plateau is reached at larger strains. This variation is attributed to the structure change of the nanocrystalline metal layer, but the physics is still unclear. Note that the change of TCR is important for metal-based flexible temperature sensors. Specifically, the variation of TCR with the strain needs to be considered when the flexible temperature sensor is stretched. Next, the thermal conductivity of strained Au-on-

polyimide films is investigated. To extract the thermal conductivity of the polyimide, the thermal conductivity of the metal layer is estimated with Wiedemann-Franz law assuming ±15% uncertainty. The in-plane thermal conductivity of the polyimide increases with the tensile strain, *e.g.*, a 60% enhancement is observed when the film is stretched beyond 25% (see Figure 5.3(c)). When the film is stretched, polymer chains tend to align along the tensile strain direction. The thermal conductivity along this direction increases due to the more organized polymer chains. Therefore, a significant increase can be expected for extremely strained polyimide due to realignment of the polymer chains.

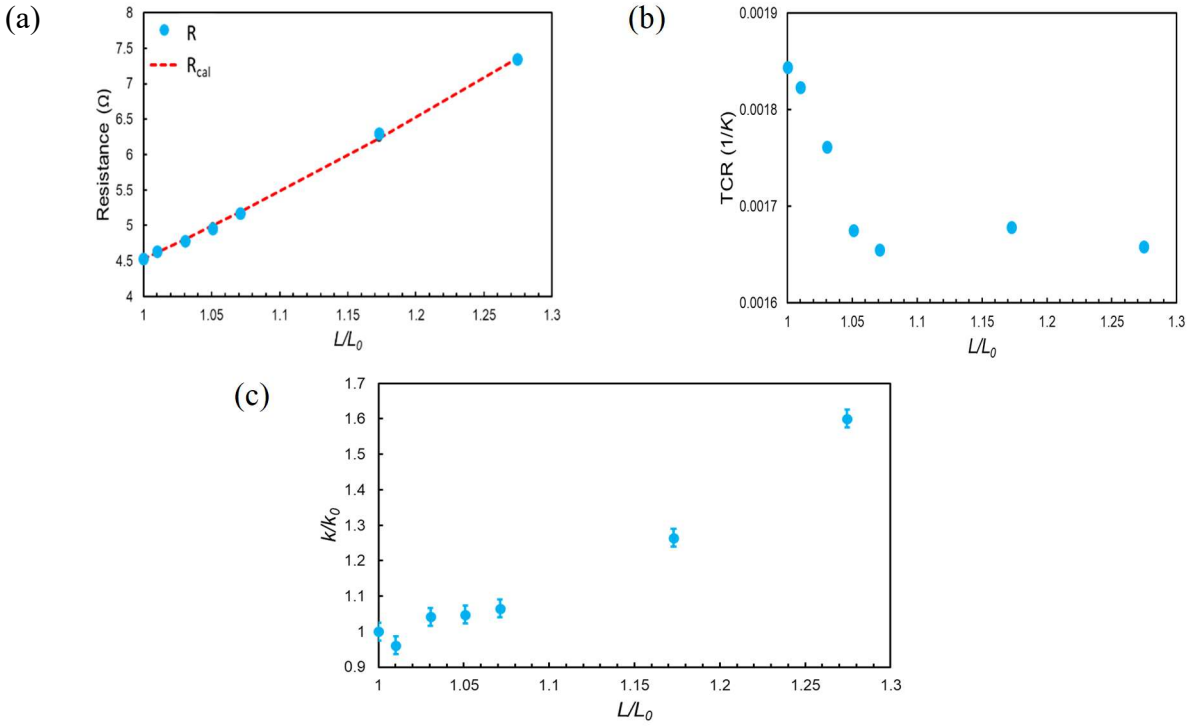

Figure 5.3 Experimental evaluation of a Au-on-polyimide strip. (a) The electrical resistance varies with the deformation as $(L/L_0)^2$. (b) The TCR decreases with the tensile strain. (c) The in-plane thermal conductivity increases with the tensile strain. A significant increase can be expected for extremely strained polyimide due to realignment of the polymer chains.

5.2 Thermal Transport in Graphene and Strain Engineering

Graphene has been extensively studied for both fundamental science and commercial applications due to its unique mechanical, electrical, and thermal properties since graphene was first exfoliated from highly oriented pyrolytic graphite [114]. For commercial applications, mass

production of high quality graphene is critical as the size of exfoliated graphene flakes is generally in the order of 10 μm. Many methods have been developed to obtain relatively large-scale, high-crystallinity graphene including chemical vapor deposition [115–117] (CVD) on a metal catalyst such as Cu or Ni. Properties of exfoliated and CVD graphene have been broadly investigated in the past decade, which enables new understanding of transport phenomena in low-dimensional materials.

Thermal transport in graphene has attracted significant interest. Its superior thermal conductivity, reported in the first experimental study of suspended graphene [8], demonstrates that graphene as a potential solution for thermal management in modern electronics. Further, layer-dependent thermal conductivity measurements were performed to understand the inter-layer interaction. However, measurements based on electrothermal methods [15,118] revealed the thermal conductivity increases with number of layers, approaching the value of bulk graphite, which is opposite to the trend observed in Raman-based measurements [119]. It is unclear whether the conflict in the measurements is due to sample-to-sample variations (exfoliated and CVD graphene) or measurement techniques (Raman-based and electrothermal measurement). Later, more experimental studies, based on electrothermal measurements, focused on thermal conductivity of on-substrate graphene prepared by exfoliation and CVD method. A thermal conductivity reduction was observed in supported graphene compared to that of suspended graphene [10,120,121]. Molecular dynamics (MD) simulations attributed the reduction to a strong interaction between the substrate and graphene and thus a suppression of phonon transport [122].

While thermal conductivity of graphene has been intensively investigated, experimental study of tuning the thermal conductivity is limited [123], especially when compared to tuning electronic properties such as band-gap opening via strain [124–127]. By analogy with strain engineering of electronic properties, a natural question is how the phonon band structure, phonon scattering, and the thermal conductivity are impacted by strain. For supported graphene, it is of significant interest to reveal the impact of strain on the interfacial bonding between the graphene and substrate and the effective thermal conductivity.

Although many computational studies have been performed, no experimental efforts, to our knowledge, have directly measured the impact of strain on thermal transport in graphene. But the simulation results are not consistent between models. For single layer graphene, Wei *et al.* [128] predicted that small tensile and compressive strains both decrease the thermal conductivity, but

other researchers demonstrate that tensile strain can largely enhance thermal conductivity [129–131], which is promising for the thermal management in microelectronics. For multi-layer graphene, Kuang *et al.* [131] predicted that the competition of increasing phonon lifetime and decreasing mode capacity leads an initial increase then decrease in thermal conductivity with increasing tensile strain and this response is dependent on the number of layers in the stack.

Here, we perform a strain-dependent experimental study of thermal conductivity in supported graphene. The strain is transferred to the suspended sample by stretching the substrate. As for the on-substrate measurement, graphene on epoxy is selected due to its strong adhesion and broad applications in MEMS [132–138]. For the study of supported graphene, an epoxy (SU 8) is selected as a substrate due to its uniformity obtained via spin coating. Compared to the amorphous support layer such as silicon dioxide (SiO_2), the epoxy can be elongated greater than 10% [139] while the SiO_2 layer breaks around ~1.0% tensile strain [140]. Further, the low thermal conductivity [141] of the selected epoxy is beneficial here, as it ensures more heat is conducted through the graphene which is good for extracting the thermal conductivity of supported graphene. Another advantage is its high surface energy and good adhesion with graphene, which is not attainable with many other polymer-based substrates. As suggested in prior work [122], the polymer and amorphous substrate may scatter phonons in graphene similarly, so this measurement can be of broad interest for the study of strain dependence of the thermal conductivity of supported graphene.

The thermal conductivity measurement is adapted from the electrothermal measurement method with strain control described in detail in chapter 2. We prepare ~10 nm multilayer graphene (MLG) films on copper (Cu) foils using a plasma enhanced chemical vapor deposition method [142,143]. Figure 5.4(a) shows the Raman spectral of MLG films transferred to SiO2/Si substrate. A 2 μm thick epoxy (SU 8) layer is spin coated on the MLG films. Then, the ultraviolet-exposed SU 8 is fully dried by a hard bake at 150 ˚C. Next, the Cu foil with MLG films is cut into strips with appropriate sizes. The MLG film on SU 8 is peeled off from the Cu foil. This method allows a dry and clean transfer of graphene and gives a large-scale continuous graphene films. The peel-off MLG film on SU 8 is suspended over the electrodes on a flexible substrate for the electrothermal measurement (see Figure 5.4 (b)). Silver paste is used to provide a stable electrical contact and a reliable mechanical connection. Figure 5.4 (c) and (d) demonstrates the calibrated

electrical resistance as a function oftemperature and an example of resistance variation *vs.* square of current, respectively.

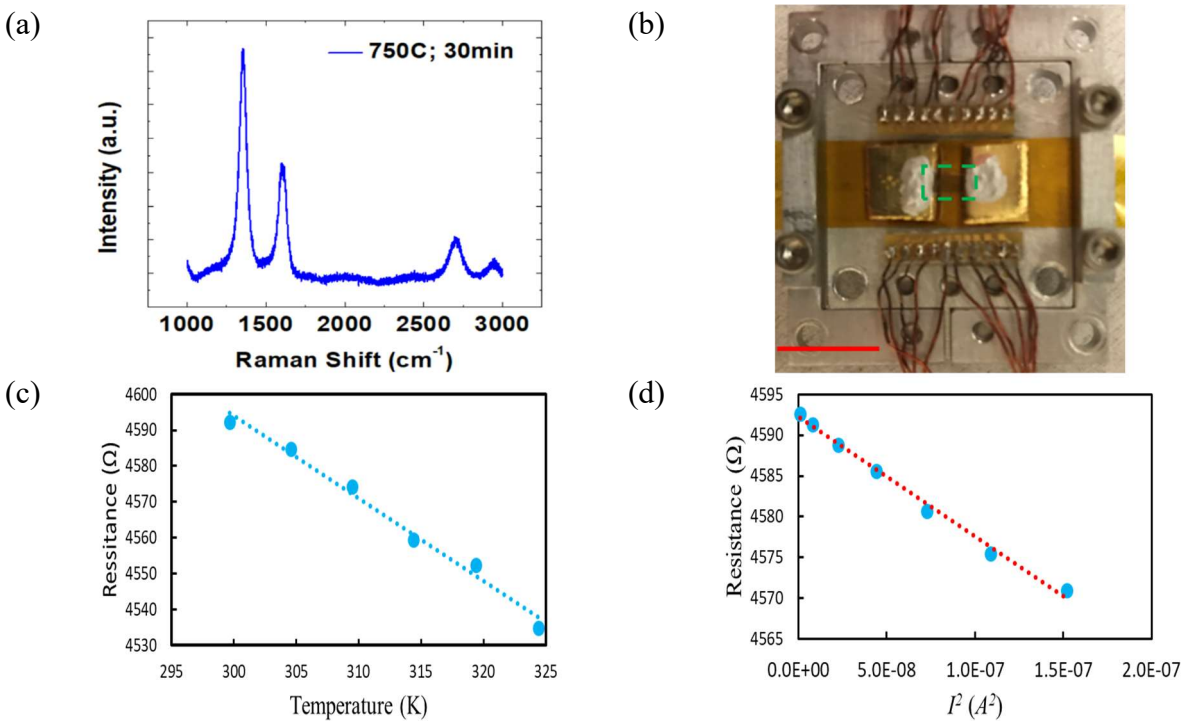

Figure 5.4: (a) Raman spectral of MLG films transferred to SiO2/Si substrate. (b) The MLG films on SU 8, encircled by the green dashed lines, suspended over the electrodes on a flexible substrate. The strain of the sample is controlled by stretching the substrate. The scale bar is 1 cm. (c) The calibrated electrical resistance as a function of temperature for the supported MLG films. (d) An example electrothermal response, resistance variation with the square of current, for the free-strain MLG films.

To extract the thermal conductivity of graphene from the composite layer, we use the reported thermal conductivity 0.2-0.3 W/m-K for the SU 8 layer [144]. Given the high thermal conductivity of the MLG layer, the fraction of heat carried by the SU 8 layer is smaller than 5%. The thickness of the MLG layer is assumed to be 10 ± 0.5 nm, which is an estimation based on previous work by the same group [142,143]. Figure 5.5 (a) shows the temperature-dependent thermal conductivity of supported MLG films stretched by 0, 0.5%, and 1.0%. Thermal conductivity of the free-strain MLG film increases with the temperature from 300 K to 320 K, while no clear temperature dependence of thermal conductivity is observed for strained MLG films in such a small temperature range. A decrease of the thermal conductivity from 1090.2 ± 54.6

W/m-K to 789.2 ± 39.6 W/m-K is observed when the free-strain MLG layer is stretched 1%, as shown in Figure 5.5 (b).

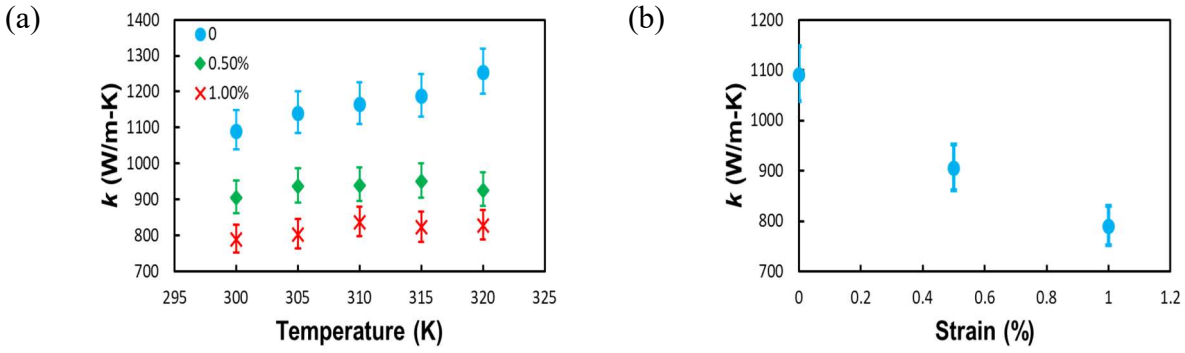

Figure 5.5: (a) Temperature-dependent thermal conductivity of supported MLG films stretched by 0, 0.5%, and 1.0%. (b) Thermal conductivity of supported MLG films at 300 K decreases with the tensile strain. A decrease of the thermal conductivity from 1090.2 ± 54.6 W/m-K to 789.2 ± 39.6 W/m-K is observed when the free-strain MLG layer is stretched 1%.

The decrease is understood using a simplified expression of thermal conductivity $k = \frac{1}{3} C v \Lambda_{eff}$, where $\Lambda_{eff}^{-1} = \Lambda_i^{-1} + \Lambda_{def}^{-1} + \Lambda_{GB}^{-1}$. Λ_i , Λ_{def} , and Λ_{GB} are the phonon mean free path due to intrinsic phonon-phonon scattering, phonon-defect scattering, and phonon-grain boundary scattering, respectively. Based on the previous simulations of single crystalline graphene, the phonon band structure does not vary much with 1% tensile strain, and thus the significant decrease observed in our measurement of polycrystalline MLG films is not likely due to the change of phonon band structure [128–131]. Therefore, we attribute the decrease to the impact of tensile strain on the probability of specular phonon transmission (p_{tr}) across the grain boundaries, which relates the grain size l_g to $\Lambda_{GB} = l_g \left(\frac{1 + p_{tr}}{1 - p_{tr}} \right)$ [145].The decrease of thermal conductivity with tensile strain indicates the reduced specular transmission probability and thus the decreased effective phonon mean free path.

5.3 Summary

This chapter characterizes strain-dependent thermal conductivity study of Au-on-polyimide films and supported MLG films. Suspended samples on a flexible substrate combined with a custom-built mechanical stage enables strain-dependent thermal conductivity characterization using the

electrothermal method. For the Au-on-polyimide film, the impact of strain on the electrical resistance, TCR, and thermal conductivity is investigated, which provides useful information for flexible electronics and flexible temperature sensors. A decrease of thermal conductivity with the tensile strain is observed for the supported MLG films. Based on a simple model, the decrease is attributed to the impact of tensile strain on the phonon transmission probability in polycrystalline MLG films. A more complete model needs to be built in the future to understand the strain effects on thermal transport in 2D materials. Further, the thermal metrology developed in chapter 2 enables an accurate strain-dependent thermal conductivity measurement of microscale samples. Future work based on this will help illustrate the role of strain in thermal conductivity of 2D materials.

6. TUNING THERMAL CONDUCTIVITY OF REDUCED GRAPHENE OXIDE FILMS VIA ANNEALING[3]

6.1 Introduction

Carbon based nanostructures (*e.g.*, graphene) exhibit unique mechanical, electrical, and thermal properties.[8,146,147] Graphene has shown promise as a material for thermal management, flexible electronics, and numerous sensors.[148–150] However, it is still challenging to produce a large-scale graphene film with high quality for commercial applications. Inspired by the excellent properties of nanostructures including graphene films, researchers are attempting to produce macroscale materials with nanoscale features. Often, this is a two-step procedure: first, mass production of the material (generally with relatively poor properties) and then processing to enhance the properties. For example, graphene oxide (GO) films can be mass produced from graphite using Hummer's method.[151,152] Although these films have excellent mechanical properties, the electrical and thermal conductivity are typically very poor due to the disorder, defects, and impurities. Reducing these graphene oxide films via chemical, thermal and other methods significantly improves the electrical and thermal conductivity.[9–21] In particular, reduced graphene oxide (RGO) films have been investigated as fast temperature sensors for the temperature range from ~80K to ~550K due to the significant temperature dependence of the electrical conductivity.[166–168]

The electrical and thermal properties of the RGO films are critical to their application in systems such as flexible electronics, energy storage, and thermal management.[156,159,160] The four-probe method and the laser flash technique have previously been used to measure the electrical and thermal conductivity, respectively.[154,155,158,161–164,169,170] Although relatively consistent results are observed for the electrical conductivity data (> 1000 S/cm), existing thermal conductivity data for the RGO films shows large variations from 30 W/m-K to 2600 W/m-K.[154,155,158,161–164,169,170] In addition to the sample-to-sample variation, the validity and accuracy of the thermal conductivity measurement technique needs to be considered. Unlike the widely applicable four-probe electrical conductivity technique, the validity of the laser

[3] This section reproduced from a paper with UMD and UC-Berkeley collaborators: *Nature Energy* **3**, pages148–156 (2018).

flash technique for measuring is questionable for high thermal conductivity thin films. Specifically, the method is accurate when the laser pulse is sufficiently short compared to the characteristic time of diffusion through the sample: $t_c=L^2/(k/\rho C_p)$, where L is the sample thickness, k is the thermal conductivity, ρ is the density, and C_p is the heat capacity.[171–173] Considering the short t_c of the measured RGO films (0.00003-0.12 μs for the reported RGO films with thickness L =10-50 μm, thermal conductivity k = 30-2600 W/m-K, density ρ = 1-2 g/cm^3, and specific heat capacity C_p ~= 0.72 J/g-K)[154,155,158,161–164,169,170] and the typical pulse width (20-1200 μs) of the commercial laser flash systems,[174] the accuracy of the thermal conductivity of RGO films in prior work by the flash method is uncertain. In addition, low-temperature thermal conductivity data is critical for understanding thermal transport mechanisms in RGO films, and previous work focused on measuring k above room temperature only. Therefore, there is a clear need to perform a temperature-dependent study of thermal transport in RGO films.

In this work, a self-heating and –sensing electrothermal method is used to measure the in-plane thermal conductivity of RGO films annealed at 1000 K, 2000 K and 3000 K (called "RGO 1000K", "RGO 2000K", and "RGO 3000K", respectively) in the temperature range from 10 K to 300 K. The thermal conductivity increases substantially from 46.1 W/m-K to 118.7 W/m-K with increasing annealing temperature from 1000 K to 3000 K with a corresponding increase in electrical conductivity from 5.2 S/cm to 1481.0 S/cm. Further, the electrical and thermal conductivity at temperatures above 300 K are measured for specific applications. We report the electrical resistivity from 10 K to 3000 K to highlight the application of RGO films reduced at 3000 K for sensing extreme temperatures. Compared to conventional temperature sensors, the RGO-based temperature sensors are unique due to its wide temperature range, high temperature sensitivity, and flexibility. With the measured thermal conductivity and the power-law temperature dependence assumption, the potential application of RGO films for high temperature thermoelectrics is investigated.

6.2 GO Films Preparing & Annealing

An aqueous GO solution is prepared with an improved Hummer's method[151,152] and 3D printed to form uniform films. A two-step annealing process reduces the GO films to RGO films.[160,165,175] First, the GO films are annealed at 1000 K in a tube furnace under argon

atmosphere and obtain good uniformity and electrical conductivity. Then, they are Joule heated to further thermally reduce the GO leveraging the high melting point of carbon-based materials.

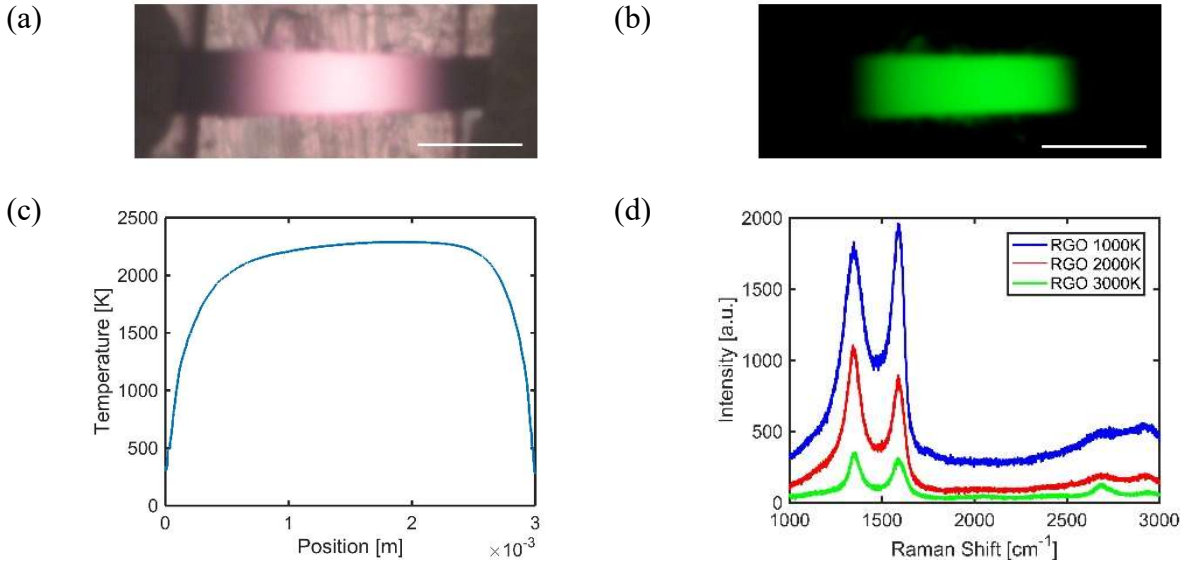

Figure 6.1: (a) Optical photograph and (b) thermal image taken with a 550 nm bandpass filter of a free-standing GO film while being reduced by Joule heating at 2300 K in vacuum. Note that the GO films can be Joule-heated to even higher temperatures with increasing electrical input. (c) The local temperature of the film as determined by fitting the measured emission spectrum, collected by a fiber-coupled spectrometer, to the Planck function. (d) Raman spectra of the RGO films reduced at 1000 K, 2000 K, 3000 K, respectively. For RGO films reduced at 3000 K, the clear 2D peak at 2700 cm^{-1} indicates the increased crystallinity. The scale bar is 1 mm in panel (a) and (b).

Specifically, they are gradually Joule-heated to 2000 K or 3000 K for this work, and even higher temperatures are possible with increasing electrical input. An example of a free-standing electrically heated GO film at 2300 K in vacuum is shown in Figure 6.1(a-c). The temperature during Joule heating is determined by fitting the emitted radiation spectrum to the Planck distribution $I_\lambda(\lambda,T)=\frac{2hc^2}{\lambda^5\exp(hc/(\lambda k_B T-1))}$, where h, c, k_B, and λ are the Planck constant, speed of light in vacuum, Boltzmann constant, and wavelength, respectively. The emission intensity of the Joule heated RGO films is measured by a fiber-coupled spectrometer (Ocean Optics. Inc.). Although the ends of the sample are significantly colder, a large portion near the center of the sample achieves the desired annealing temperature. Figure 6.1(d) shows the Raman spectra of RGO films reduced at 1000 K, 2000 K, and 3000 K, respectively. For RGO films reduced at 3000 K, the clear 2D peak at 2700 cm^{-1} indicates the increased crystallinity. Scanning electron

micrographs (SEMs) of the RGO films (see Figure 6.2) demonstrate the surface of the RGO films reduced at higher temperatures becomes smoother.

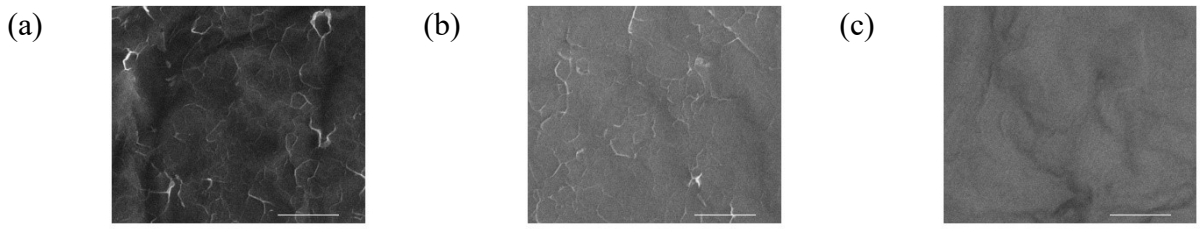

Figure 6.2: SEM images of RGO films reduced at (a) 1000 K, (b) 2000 K, and (c) 3000 K. The surface of the RGO films becomes smoother with higher reduction temperatures. The scale bar is 10 μm in the figures.

6.3 Thermal Characterization

Rectangular RGO strips with appropriate length-to-width ratios are prepared for one-dimensional heat transfer analysis. The thermal conductivity of RGO films is investigated using both infrared (IR) thermal microscopy -based measurement and electrothermal measurement. In both measurements, current is applied in the suspended RGO films to generate heat and the total power generation is determined with a standard four-probe measurement. In the IR microscopy based measurement, the temperature profile along the RGO strip is obtained and the thermal conductivity is calculated by fitting to the temperature profile[176]. For the electrothermal measurement, with the calibrated temperature-dependent electrical resistivity, the thermal conductivity is measured at a wider temperature range (10K – 650K) with RGO films serving as both heater and thermometer.

6.3.1 Infrared Microscopy

Infrared (IR) thermal microscopy is a noncontact technique to obtain surface temperature mapping utilizing infrared radiation emitted from the surface. RGO films suspended over a trench, as shown in Figure 6.3 (a), are joule heated with applied current and the power is determined with an electrical four-probe measurement. Heat generated in the sample is transferred to the air via convection and to the substrate via heat conduction. Heat transfer along the sample can be described using 1D heat diffusion equation as

$$kA\frac{d^2T(x)}{dx^2}+\frac{I^2R_0}{L}[1+\alpha(T(x)-T_0)]-hP(T(x)-T_a)=0 \quad \text{and} \tag{6.1}$$

$$T(x = \pm\frac{L_f}{2}) = T_f, \tag{6.2}$$

where A, P, and L are the cross-sectional area, perimeter, length of the suspended sample, L_f is the length of the region for heat transfer fitting analysis, and k and α are the thermal conductivity and temperature coefficient of resistance of the sample, respectively. $T(x)$ is the temperature profile along the sample and T_0, T_a, and T_f are the temperatures of the substrate, air, and the boundary of the fitting region, respectively. I and R_0 are the applied current and the electrical resistance of the sample at T_0 without Joule heating, respectively. Assuming a uniform convection heat loss coefficient (h = constant), the analytic solution of the diffusion equation is

$$T(x) = T_a + (T_f - T_a)\frac{\cosh(mx)}{\cosh(mL_f/2)} - \frac{g + \alpha g(T_a - T_0)}{hP - \alpha g}\left(\frac{\cosh(mx)}{\cosh(mL_f/2)} - 1\right), \tag{6.3}$$

where $g = I^2R_0/L$ and $m^2 = (hP-\alpha g)/kA$ when $hP-\alpha g > 0$. Note the constant h assumption is only valid when the temperature rise of the sample is small compared to the substrate temperature. An example temperature profile along the sample and an example fitting are shown in Figure 6.3 (a) and (b), respectively. It is clear that the temperature profile is nearly 1D verifying the effectiveness of 1D solution. Figure 6.3 (c) shows the temperature dependent thermal conductivity of RGO films and the thermal conductivity increases with temperature in the investigated temperature range (293K – 373K).

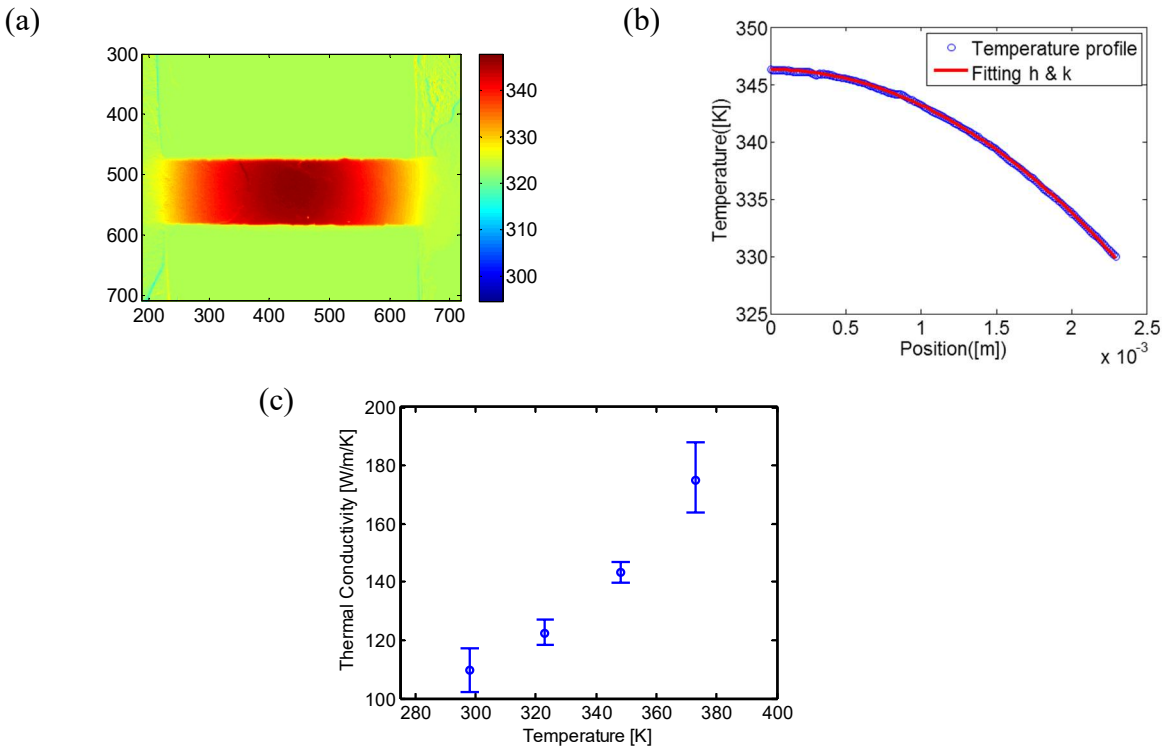

Figure 6.3: (a) Temperature mapping of the RGO film suspended over a trench. The suspended sample is joule heated with applied current. Self-heat generation results in a parabolic temperature profile. (b) Thermal conductivity extraction by fitting to the temperature profile using the 1D solution. (c) Temperature-dependent thermal conductivity from 293K to 373 K.

6.3.2 Electrothermal measurement

The electrical conductivity of the RGO film varies linearly with temperature in a specific range, as illustrated by the linear trend in *1/R(T) vs T* from 300 K to 630 K(see Figure 6.4 (a)). Figure 6.4 (b) demonstrates the temperature dependence of the electrical resistance from 10 K to 300 K. Therefore, the RGO film can serve as both heater and thermometer for the thermal measurement in this temperature range. The four-probe electrothermal measurement of the suspended RGO film is performed in a high temperature probe station (see Figure 6.4 (b)) and a cryostat, respectively. Heat generated by Joule heating with an applied current is conducted through the RGO film to the substrate. Assuming negligible convective and radiative heat loss, the governing equation for one-dimensional heat conduction in the suspended RGO film is

$$kA\frac{d^2T}{dx^2}+I^2\frac{R}{L}=0, \text{ where} \tag{6.4}$$

$$T(x = \pm L/2) = T_0 \tag{6.5}$$

and k is the thermal conductivity of the RGO film, I is the applied electrical current, R is the electrical resistance, T_0 is the set temperature of the stage, A is the cross-section area, and L is the length of the suspended RGO film. The equation can be solved analytically, and the temperature profile is

$$\Delta T(x) = T(x) - T_0 = -\frac{I^2 R}{2kAL}x^2 + \frac{I^2 RL}{8kA} \tag{6.6}$$

which describes the relation between the temperature profile and the thermal conductivity of the RGO film. The average temperature rise along the film is given by

$$\Delta\bar{T} = \int_{-L/2}^{L/2} \Delta T(x)dx / L = \frac{I^2 RL}{12kA} \tag{6.7}$$

Here, the average temperature rise is decided with the calibrated temperature-dependent electrical resistance (see Figure 6.4 (a) and (b)). Note that the simple solution is obtained by assuming constant electrical resistance during the heating, which is valid only when the variation is small compared to the electrical resistance at the reference temperature T_0.[176] Therefore, the solution of the thermal conductivity is

$$k = \frac{I^2 RL}{12A\Delta\bar{T}} \tag{6.8}$$

The thermal conductivity is extracted by fitting to the electrothermal response ΔR *vs* I^2(see Figure 6.4 (c) and (d)). The uncertainty due to the simplified solution is analyzed by calculating the thermal conductivity with R from $R(T_0)$ to $R(\bar{T})$. The other error source comes from the assumption of negligible radiative heat loss, which is questionable at high temperatures and needs to be investigated in future work. Thus, the measured thermal conductivity is overestimated at high temperatures, which leads to a conservative estimate of the thermoelectric performance.

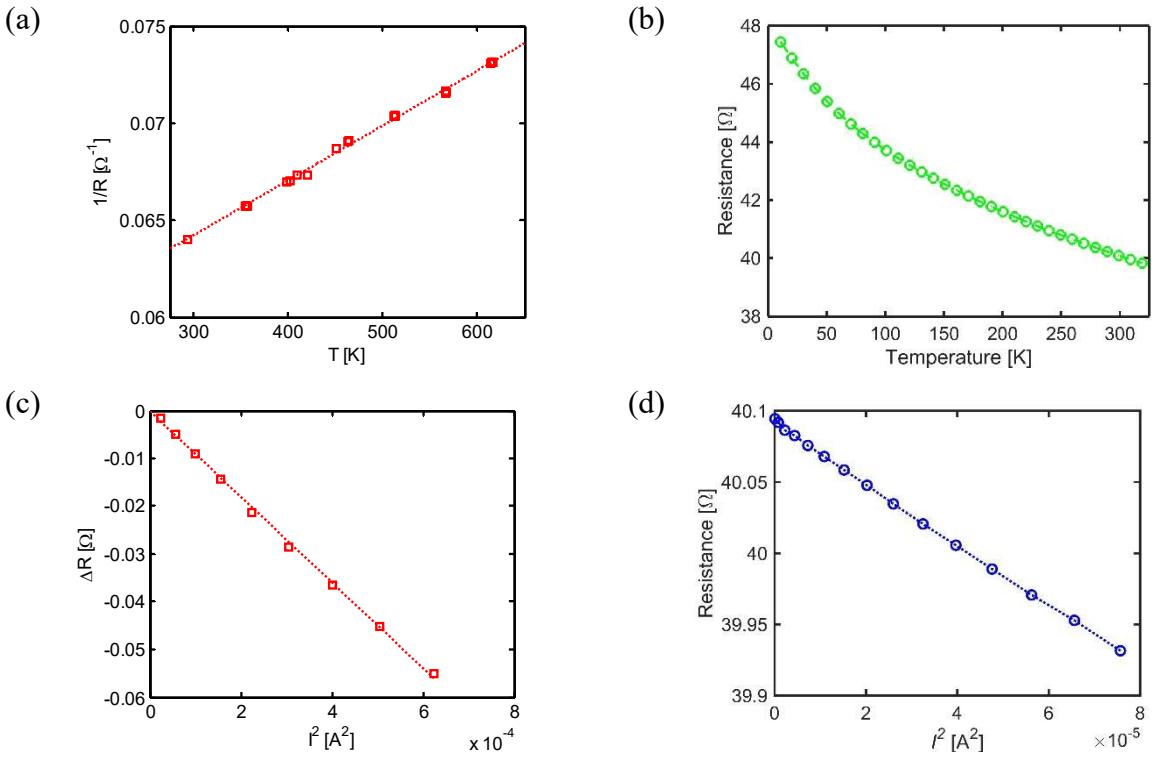

Figure 6.4: (a) Linear *1/R(T) vs. T* from 300 K to ~650 K, which reveals the RGO film can be served as both heater and thermometer. (b) Calibrated temperature-dependent electrical resistance from 10 K to 300 K using a cryostat. Unlike typical metal films, the electrical resistance decreases with increasing temperature. An example electrothermal response ΔR vs I^2 for RGO 3000 K in (c) a high temperature probe station and (d) a cryostat, respectively.

6.4 Results & Discussion

6.4.1 The Impact of Annealing Temperature on Electrical & Thermal Conductivity

Figure 6.5(a) shows the room temperature thermal and electrical conductivity for samples annealed at 1000 K, 2000 K, and 3000 K. The properties increase significantly with increasing annealing temperature. Figure 6.5(b) demonstrates the temperature-dependent electrical conductivity of RGO films reduced at 1000 K, 2000 K, and 3000 K. The electrical conductivity increases with the reduction temperature, *e.g.*, the electrical conductivity at 300 K of RGOs reduced at 1000 K, 2000 K, and 3000 K are 5.2 S/cm, 524.8 S/cm, and 1481.0 S/cm, respectively. Electrical transport in the RGO films can be understood by a three-dimensional (3D) Mott variable range hopping (Mott-VRH) model combined with thermal activation and quantum tunneling as[177]

$$G(T) = G_h \exp(-\frac{H}{T^{1/4}}) + G_a \exp(-\frac{T_a}{T}) + G_t \tag{6.9}$$

where G_h, G_a and G_t are the parameters for the contributions of Mott-VRH, thermal activation, and quantum tunneling, respectively, H is a hopping parameter, T_a is the characteristic temperature for thermal activation, and $k_B T_a$ describes the thermal energy required to thermally excite carriers to the conduction band. By fitting the measured electrical conductance to Eqn. (6.4), a comparison between RGO 1000 K and RGO 3000 K shows a decrease of the thermal energy barrier from 20.8 meV to 3.4 meV and an increase of the contribution due to quantum tunneling from 0.7 μS to 0.021 S. Therefore, the contribution of thermal activation and quantum tunneling increases with the reduction temperature due to the more crystalline structure.

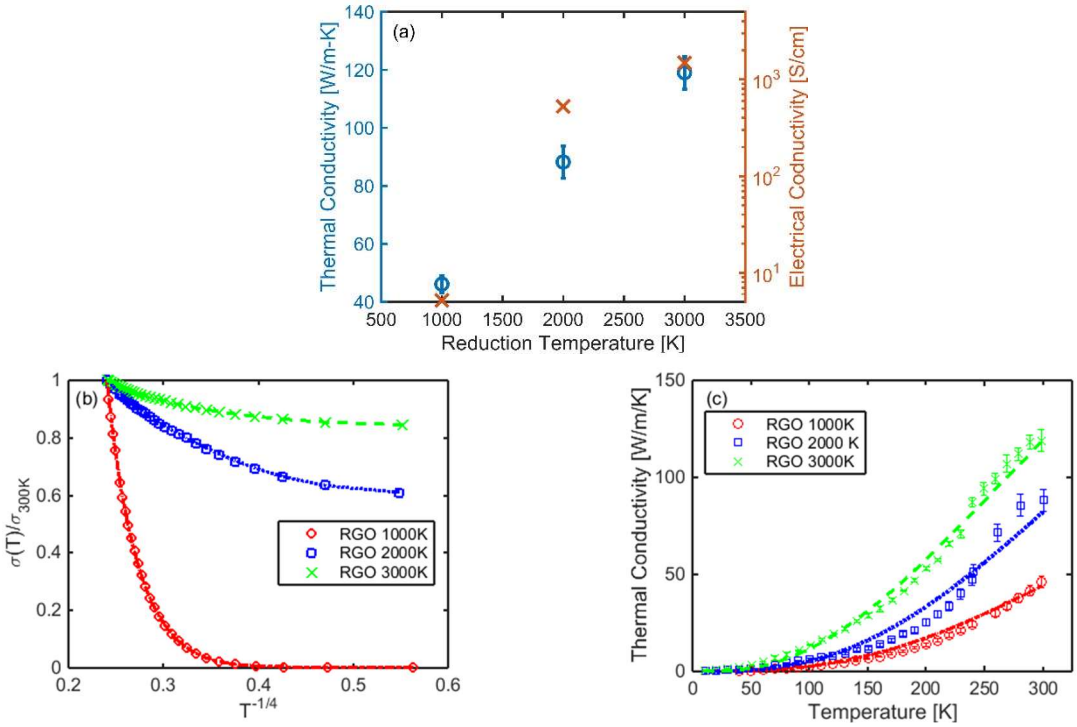

Figure 6.5: (a) Thermal conductivity and electrical conductivity at 300 K for RGO 1000 K, 2000 K, and 3000 K. (b) Normalized electrical conductivity $\sigma(T)/\sigma_{300\,K}$ of the RGO films reduced at 1000 K, 2000 K, and 3000 K versus $T^{-1/4}$. The electrical conductivity data is fitted with a 3D Mott-VRH model. (c) Thermal conductivity of RGOs from 10 K to 300 K. A thermal conductivity integral model is used to analyze the measured thermal conductivity.

Thermal conductivity of RGOs from 10 K to 300 K is shown in Figure 6.5(c). As the reduction temperature increases, Figure 6.5(a) shows the room-temperature thermal conductivity increases from 46.1 W/m-K for RGO 1000K to 118.7 W/m-K for RGO 3000K. To analyze the

measured thermal conductivity from 10 K to 300 K, we interpret the thermal conductivity using the Callaway-Holland model[30,31]

$$k = \frac{1}{6\pi^2}\sum_j \int C_j(q,T) v_j^2(q) \tau_j(q,T) q^2 dq \tag{6.10}$$

where q is the phonon wave vector, T is the temperature, and $C_j(q, T)$, $v_j(q)$, and $\tau_j(q, T)$ are the specific heat, group velocity, and relaxation time for phonon branch j, respectively. The integration is performed over three acoustic phonon branches, *i.e.*, in-plane transverse acoustic phonon, in-plane longitudinal acoustic phonon, and out-of-plane transverse acoustic phonon. For each branch, the group velocity is calculated using a quadratic fit to the full dispersion of graphite with an isotropic dispersion approximation.[178] The phonon relaxation time in RGO films is determined by the Matthiessen's rule,

$$\tau_j^{-1} = \tau_{ph,j}^{-1} + \tau_B^{-1} + \tau_{other}^{-1} \tag{6.11}$$

where $\tau_{ph,j} = \frac{M\theta_j v_{s,j}^2}{\hbar\gamma_j^2 \omega_j(q) T \exp(\theta_j / T)}$, $\tau_B = \frac{L_{eff}}{v_j(q)}$, and $\tau_{other} = \frac{4v_j(q)N}{q\Gamma S\omega_j^2(q)T^n}$ are the relaxation time due to three-phonon scattering,[159,178,179] phonon-boundary scattering, and scattering with other centers such as impurity, isotope and electron, respectively. Here, $\hbar$ is Planck's constant, $w_j(q)$ is the phonon frequency, M is the unit cell mass of graphite, Γ is the measure of the interaction strength between phonon and other scattering centers,[159] S is the cross-section area of a carbon atom, and θ_j, $v_{s,j}$, and γ_j are the branch-dependent average Debye temperature, sound velocity, and average Gruneisen parameter.[178] L_{eff} is the characteristic length for the phonon-boundary scattering term combining phonon collision with film surfaces and edges of ordered sp^2 or sp^3 clusters. Note that τ_{other} has a similar expression as that for the relaxation time of phonon-impurity scattering or phonon-isotope scattering, *i.e.*, $4v_j(q)/(q\Gamma S\omega_j^2(q))$.[159] However, with that expression, a good agreement between the calculated thermal conductivity and the temperature-dependent experimental data is not achieved (with the only fitting parameter being L_{eff}). To interpret the measured temperature dependence, we assume power-law temperature dependence T^n for the lumped relaxation time τ_{other} due to phonon scattering with the other scatters such as impurities, isotopes, and electrons. An additional fitting parameter N is used for adjusting the magnitude of τ_{other}.

These fitting parameters are determined by fitting to the temperature-dependent thermal conductivity of RGOs from 10 K to 300 K. The extracted characteristic lengths for RGOs reduced at 1000 K, 2000 K, and 3000 K are 35 nm, 60 nm, and 65 nm, respectively. The increased L_{eff} corresponds to the enlarged ordered sp^2 or sp^3 clusters with the higher reduction temperature. For the lumped scattering term, the fitting determines $N = 2.7 \times 10^6$ for RGO 1000 K, $N = 6.075 \times 10^6$ for RGO 2000 K, and $N = 2.7 \times 10^7$ for RGO 3000K. The reduced scattering rate $1/\tau_{other}$ indicates the decreased impurity or defect density for RGOs reduced at higher temperatures. The temperature dependence of the thermal conductivity is well explained with $n = 3$, which implies the lumped scattering term is temperature-dependent due to the interaction between phonons and the other scatters. With the thermal conductivity integral model, the improved thermal conductivity of RGOs is attributed to the increased L_{eff} and the reduced scattering rate $1/\tau_{other}$.

6.4.2 Electrical & Thermal Conductivity of RGO 3000 K above 300 K

In addition to electrothermal measurements from 10 K to 300 K, we measure the temperature-dependent electrical resistivity of RGOs reduced at 3000K from 300 K to ~3000 K (see Figure 6.6(a)) and discuss the application of RGO 3000 K as a temperature sensor for extreme temperature ranges. The measurement from 10 K to 3000 K is divided into three temperature ranges: 10 K to 300 K in a cryostat, 300 K to ~ 1100 K in a traditional oven, and ~1400 K to ~3000 K using a Joule heating method. Note that the error bars represent the uncertainty in terms of repeated measurements, sample-to-sample variations, and nonuniform temperature across the film. With the measured electrical resistivity from 10 K to 3000 K, the temperature dependence indicates RGO 3000 K as a potential temperature sensor with an extremely wide temperature range. The fitting to the temperature *vs.* electrical resistivity data is performed with a third-order polynomial for $T = 10$ K - 300 K, a linear equation for $T = 300$ K - 1400 K, and a fifth-order polynomial for $T = 1400$ K - 3000 K. The temperature sensitivity of resistance temperature detectors (RTDs) is generally evaluated by temperature coefficient of resistance (TCR) $\alpha = d\rho/(\rho_0 dT)$, where ρ is the temperature-dependent electrical resistivity and ρ_0 is the electrical resistivity at the reference temperature. The TCR is a constant when the resistivity varies linearly with the temperature, and the temperature can be easily known by solving a linear equation with the measured resistance. However, the linear variation is valid only for a small temperature range. Here, for a wide

temperature range, we use $d\rho/dT$ to describe the temperature sensitivity of RGO 3000 K as the temperature is ultimately determined by the resistance change. Figure 6.6(b) displays $d\rho/dT$ of RGO 3000 K from 10 K to 3000 K. Platinum is known as the best metal for RTDs with $d\rho/dT$ = 0.041552 μΩ·cm/K at room temperature, while that of RGO 3000 K is higher than this value over the wide temperature range. A comparison with the traditional Platinum RTDs demonstrates the excellent temperature sensitivity of RGO 3000 K from 10 K to 3000 K.

Besides the temperature sensitivity, the wide applicable temperature range of the RGO film is unique. Though not directly measured, the ρ-T trend suggests that the electrical resistivity would keep increasing as the temperature decreases below 10 K, while a constant value (the residual resistivity) is reached for metals at a similar low temperatures. For the high temperature limit, the carbon-based RGO film can survive at such temperatures due to its extremely high melting point (> 3000 K). Further, compared to fragile RTD elements, the RGO film is mechanically robust and flexible. The flexibility of printable RGO-based temperature sensors extends its capability for temperature measurements where optical detection is inaccessible

Figure 6.6(c) shows a good agreement between the thermal conductivity of 3000K RGO measured with electrothermal method and IR microscope -based technique. Good agreement in thermal conductivity further verifies the accuracy of the measurement techniques. We assume power-law temperature dependence for thermal conductivity at temperatures above 630 K, and the high-temperature thermal conductivity is estimated with measured thermal conductivity from 300 K to 630 K. With the measured power factor and estimated thermal conductivity at high temperature, we demonstrate the RGO films as a promising candidate for high temperature thermoelectrics.

(a)

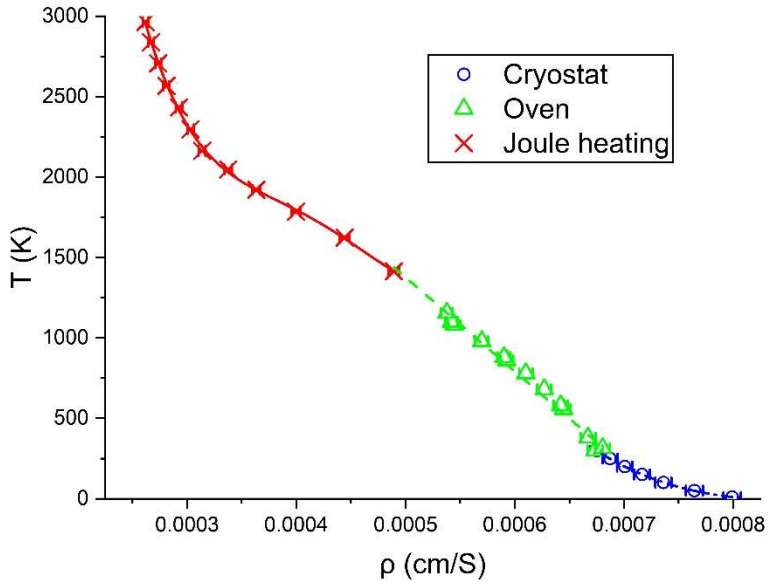

(b)

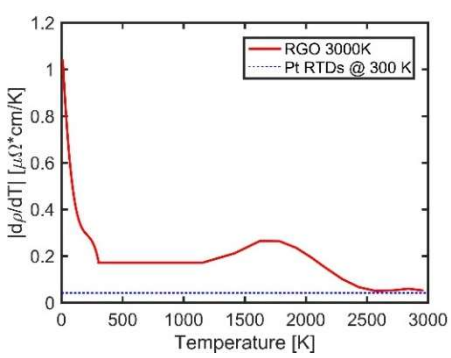

(c)

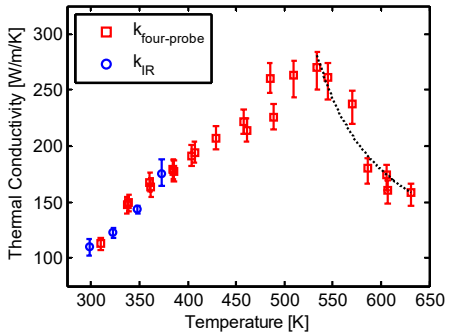

Figure 6.6: (a) Temperature vs. electrical resistivity for RGO 3000 K. The fitting is performed with a third-order polynomial for T = 10-300 K, a linear equation for T = 300-1400 K, and a fifth-order polynomial for T = 1400-3000 K. (b) Temperature sensitivity $d\rho/dT$ of RGO 3000K from 10 K to 3000 K compared to that of platinum RTDs at room temperature. (c) Temperature-dependent thermal conductivity of RGO films using electrothermal measurements. The thermal conductivity at high temperatures follows a $(1/T^n)$ decreasing trend.

6.5 Summary

In conclusion, we report electrothermal measurements of in-plane thermal transport and electrical transport in RGO films reduced at 1000 K, 2000 K, and 3000 K in the temperature range between 10 K and 300 K. We observe a substantial increase of thermal conductivity at 300 K from 46.1 W/m-K to 118.7 W/m-K when comparing RGO 1000K to RGO 3000K, and the corresponding increase of electrical conductivity is from 5.2 S/cm to 1481.0 S/cm. The impact of the reduction temperature on electrical and thermal transport is analyzed by a three-dimensional

(3D) Mott variable range hopping (Mott-VRH) model and a thermal conductivity integral model, respectively. Further, the RGO films reduced at 3000 K are demonstrated to be an effective extremely wide-range temperature sensor for the first time with several advantages over conventional temperature sensors. With the measured thermal conductivity above 300 K, the application of the RGO films for high temperature thermoelectrics is discussed.

7. SUMMARY

This dissertation is devoted to a systematic research of tuning thermal conduction in thin films (TFs) by structuring, strain engineering and extremely high temperature annealing. The motivation is to modulate the thermal conductivity for various applications. For directing the heat flow pathways in modern applications, thickness modulated TFs with an in-plane thermal anisotropy ratio > 10 are proposed according to the Boltzmann Transport Equation (BTE) -based simulations. For the devices operated under stain, strain-dependent thermal conductivity of Au-on-polyimide films and supported multi-layer graphene (MLG) films are critical to these applications. In addition, the electrical and thermal conductivity of reduced graphene oxide (RGO) films are important for applications such as thermoelectrics and temperature sensing.

Prior work on phonon size effects focused on the reduced thermal conductivity due to nanostructuring, but little work has looked at thermal anisotropy within the in plane directions of thin films. Thickness modulated TFs are proposed to structurally impact the thermal conduction anisotropy. Simulations based on the BTE demonstrate a tunable in-plane thermal anisotropy ratio across an order of magnitude via modulating the thickness of the thin films. To predict the thermal conductivity of nanostructures, solving the full BTE can be computationally expensive. Simplified Monte Carlo methods have been developed for calculating the thermal conductivity of nanostructures. Two main types of simplified Monte Carlo methods are reevaluated. Especially, the applicability of these methods is evaluated based on the physical meaning of the methods.

Beyond structural engineering, strain engineering of the thermal conductivity of polymer-supported metal films and multi-layer graphene films is explored. Suspended samples on a flexible substrate combined with a custom-built mechanical stage enables strain dependent thermal conductivity characterization using the electrothermal method. Characterization of the strain-dependent thermal conductivity of materials enables us to probe the underlying thermal transport physics. The thermal conductivity of the polyimide layer increases with the tensile strain due to the alignment of polymer chains. For strained MLG films, a decrease of thermal conductivity with tensile strain is observed.

For a promising electrical and thermal conductivity, annealing is used to effectively reduce the RGO films and thus enhance the electrical and thermal conductivity. A unique two-step annealing process is applied to reduce the graphene oxide films. A considerable increase of

electrical and thermal conductivity is observed for RGO films as the reduction temperature increases. The measured electrical and thermal conductivity are analyzed with a 3D Mott variable range hopping model and a thermal conductivity integral model, respectively. With the measured electrical and thermal conductivity, the RGO film demonstrates as a promising candidate for high temperature thermoelectrics and extreme temperature sensing.

In addition, this dissertation presents advances of thermal metrology. A simple, direct differential method based on electrothermal metrology is developed for measuring thermal conductivity of thin films by extending conventional electrothermal approaches. The new method allows accurate thermal conductivity measurements with minimal assumptions. The accuracy of conventional electrothermal approaches for extracting thermal conductivity is investigated by comparing to this new method. Further, a thermo-mechanical metrology platform is developed for studying strain dependent thermal transport taking advantage of strain control through flexible substrate. This platform provides a widely applicable method for measuring strain-dependent thermal conductivity of semiconductor TFs, 2D materials, and other materials of interest.

REFERENCES

[1] D.G. Cahill, K. Goodson, and A. Majumdar, "Thermometry and Thermal Transport in Micro/Nanoscale Solid-State Devices and Structures," *Journal of Heat Transfer*, vol. 124, 2002, p. 223.

[2] A.M. Marconnet, M. Asheghi, and K.E. Goodson, "From the Casimir Limit to Phononic Crystals: 20 Years of Phonon Transport Studies Using Silicon-on-Insulator Technology," *Journal of Heat Transfer*, vol. 135, May. 2013, p. 061601.

[3] J.-K. Yu, S. Mitrovic, D. Tham, J. Varghese, and J.R. Heath, "Reduction of thermal conductivity in phononic nanomesh structures," *Nature Nanotechnology*, vol. 5, Oct. 2010, pp. 718–721.

[4] J. Lee, J. Lim, and P. Yang, "Ballistic Phonon Transport in Holey Silicon," *Nano Letters*, vol. 15, May. 2015, pp. 3273–3279.

[5] A.M. Marconnet, T. Kodama, M. Asheghi, and K.E. Goodson, "Phonon Conduction in Periodically Porous Silicon Nanobridges," *Nanoscale and Microscale Thermophysical Engineering*, vol. 16, Dec. 2012, pp. 199–219.

[6] J. Tang, H.-T. Wang, D.H. Lee, M. Fardy, Z. Huo, T.P. Russell, and P. Yang, "Holey Silicon as an Efficient Thermoelectric Material," *Nano Letters*, vol. 10, Oct. 2010, pp. 4279–4283.

[7] S. Berber, Y.-K. Kwon, and D. Tománek, "Unusually High Thermal Conductivity of Carbon Nanotubes," *Physical Review Letters*, vol. 84, May. 2000, pp. 4613–4616.

[8] A.A. Balandin, S. Ghosh, W. Bao, I. Calizo, D. Teweldebrhan, F. Miao, and C.N. Lau, "Superior Thermal Conductivity of Single-Layer Graphene," *Nano Letters*, vol. 8, Mar. 2008, pp. 902–907.

[9] L. Shi, D. Li, C. Yu, W. Jang, D. Kim, Z. Yao, P. Kim, and A. Majumdar, "Measuring Thermal and Thermoelectric Properties of One-Dimensional Nanostructures Using a Microfabricated Device," *Journal of Heat Transfer*, vol. 125, 2003, p. 881.

[10] J.H. Seol, I. Jo, A.L. Moore, L. Lindsay, Z.H. Aitken, M.T. Pettes, X. Li, Z. Yao, R. Huang, D. Broido, N. Mingo, R.S. Ruoff, and L. Shi, "Two-dimensional phonon transport in supported graphene.," *Science (New York, N.Y.)*, vol. 328, Apr. 2010, pp. 213–6.

[11] D.G. Cahill, "Analysis of heat flow in layered structures for time-domain thermoreflectance," *Review of Scientific Instruments*, vol. 75, Dec. 2004, pp. 5119–5122.

[12] K. Kang, Y.K. Koh, C. Chiritescu, X. Zheng, and D.G. Cahill, "Two-tint pump-probe measurements using a femtosecond laser oscillator and sharp-edged optical filters," *Review of Scientific Instruments*, vol. 79, Nov. 2008, p. 114901.

[13] Z. Luo, J. Maassen, Y. Deng, Y. Du, R.P. Garrelts, M.S. Lundstrom, P.D. Ye, and X. Xu, "Anisotropic in-plane thermal conductivity observed in few-layer black phosphorus," *Nature Communications*, vol. 6, Oct. 2015, p. 8572.

[14] J. Kim, E. Ou, D.P. Sellan, and L. Shi, "A four-probe thermal transport measurement method for nanostructures," *Review of Scientific Instruments*, vol. 86, Apr. 2015, p. 044901.

[15] I. Jo, M.T. Pettes, L. Lindsay, E. Ou, A. Weathers, A.L. Moore, Z. Yao, and L. Shi, "Reexamination of basal plane thermal conductivity of suspended graphene samples measured by electro-thermal micro-bridge methods," *AIP Advances*, vol. 5, May. 2015, p. 053206.

[16] M. Asheghi, M.N. Touzelbaev, K.E. Goodson, Y.K. Leung, and S.S. Wong, "Temperature-Dependent Thermal Conductivity of Single-Crystal Silicon Layers in SOI Substrates," *Journal of Heat Transfer*, vol. 120, 1998, p. 30.

[17] M.S. Aubain and P.R. Bandaru, "In-plane thermal conductivity determination through thermoreflectance analysis and measurements," *Journal of Applied Physics*, vol. 110, Oct. 2011, p. 084313.

[18] M.S. Aubain and P.R. Bandaru, "Determination of diminished thermal conductivity in silicon thin films using scanning thermoreflectance thermometry," *Applied Physics Letters*, vol. 97, Dec. 2010, p. 253102.

[19] W. Liu and M. Asheghi, "Phonon–boundary scattering in ultrathin single-crystal silicon layers," *Applied Physics Letters*, vol. 84, May. 2004, pp. 3819–3821.

[20] Y.S. Ju, "Phonon heat transport in silicon nanostructures," *Applied Physics Letters*, vol. 87, Oct. 2005, p. 153106.

[21] W. Liu and M. Asheghi, "Thermal Conductivity Measurements of Ultra-Thin Single Crystal Silicon Layers," *Journal of Heat Transfer*, vol. 128, 2006, p. 75.

[22] A. Weathers, K. Bi, M.T. Pettes, and L. Shi, "Reexamination of thermal transport measurements of a low-thermal conductance nanowire with a suspended micro-device," *Review of Scientific Instruments*, vol. 84, Aug. 2013, p. 084903.

[23] E. Chávez-Ángel, J.S. Reparaz, J. Gomis-Bresco, M.R. Wagner, J. Cuffe, B. Graczykowski, A. Shchepetov, H. Jiang, M. Prunnila, J. Ahopelto, F. Alzina, and C.M. Sotomayor Torres, "Reduction of the thermal conductivity in free-standing silicon nano-membranes investigated by non-invasive Raman thermometry," *APL Materials*, vol. 2, Jan. 2014, p. 012113.

[24] J. Cuffe, J.K. Eliason, A.A. Maznev, K.C. Collins, J.A. Johnson, A. Shchepetov, M. Prunnila, J. Ahopelto, C.M. Sotomayor Torres, G. Chen, and K.A. Nelson, "Reconstructing phonon mean-free-path contributions to thermal conductivity using nanoscale membranes," *Physical Review B*, vol. 91, Jun. 2015, p. 245423.

[25] C. Dames, S. Chen, C.T. Harris, J.Y. Huang, Z.F. Ren, M.S. Dresselhaus, and G. Chen, "A hot-wire probe for thermal measurements of nanowires and nanotubes inside a transmission electron microscope," *Review of Scientific Instruments*, vol. 78, Oct. 2007, p. 104903.

[26] M. Fujii, X. Zhang, H. Xie, H. Ago, K. Takahashi, T. Ikuta, H. Abe, and T. Shimizu, "Measuring the Thermal Conductivity of a Single Carbon Nanotube," *Physical Review Letters*, vol. 95, Aug. 2005, p. 065502.

[27] *Lake Shore Model 325 Temperature Controller User's Manual*, 2013.

[28] Z. Luo, H. Liu, B.T. Spann, Y. Feng, P. Ye, Y.P. Chen, and X. Xu, "Measurement of In-Plane Thermal Conductivity of Ultrathin Films Using Micro-Raman Spectroscopy," *Nanoscale and Microscale Thermophysical Engineering*, vol. 18, Apr. 2014, pp. 183–193.

[29] M. Asheghi, Y.K. Leung, S.S. Wong, and K.E. Goodson, "Phonon-boundary scattering in thin silicon layers," *Applied Physics Letters*, vol. 71, Sep. 1997, pp. 1798–1800.

[30] J. Callaway, "Model for Lattice Thermal Conductivity at Low Temperatures," *Physical Review*, vol. 113, Feb. 1959, pp. 1046–1051.

[31] M.G. Holland, "Analysis of Lattice Thermal Conductivity," *Physical Review*, vol. 132, Dec. 1963, pp. 2461–2471.

[32] W. Weber, "Adiabatic bond charge model for the phonons in diamond, Si, Ge, and α-Sn," *Physical Review B*, vol. 15, May. 1977, pp. 4789–4803.

[33] C.Y. Ho, R.W. Powell, and P.E. Liley, “Thermal Conductivity of the Elements,” *Journal of Physical and Chemical Reference Data*, vol. 1, Apr. 1972, pp. 279–421.

[34] P.E. Hopkins, P.T. Rakich, R.H. Olsson, I.F. El-kady, and L.M. Phinney, “Origin of reduction in phonon thermal conductivity of microporous solids,” *Applied Physics Letters*, vol. 95, Oct. 2009, p. 161902.

[35] P.E. Hopkins, C.M. Reinke, M.F. Su, R.H. Olsson, E.A. Shaner, Z.C. Leseman, J.R. Serrano, L.M. Phinney, and I. El-Kady, “Reduction in the Thermal Conductivity of Single Crystalline Silicon by Phononic Crystal Patterning,” *Nano Letters*, vol. 11, Jan. 2011, pp. 107–112.

[36] K. Fuchs and N.F. Mott, “The conductivity of thin metallic films according to the electron theory of metals,” *Mathematical Proceedings of the Cambridge Philosophical Society*, vol. 34, Jan. 1938, p. 100.

[37] E.H. Sondheimer, “The mean free path of electrons in metals,” *Advances in Physics*, vol. 1, Jan. 1952, pp. 1–42.

[38] D.G. Cahill, “Thermal conductivity measurement from 30 to 750 K: the 3ω method,” *Review of Scientific Instruments*, vol. 61, Feb. 1990, pp. 802–808.

[39] H.T. Kaibe, Y. Noda, Y. Isoda, and I.A. Nishida, “Temperature dependence of thermal conductivity for Mg,Sii-xGex,” *ASME 2008 First International Conference on Micro/Nanoscale Heat Transfer*, vol. 718, 2014, pp. 279–282.

[40] Y. Zeng and A. Marconnet, “A direct differential method for measuring thermal conductivity of thin films,” *Review of Scientific Instruments*, vol. 88, Apr. 2017, p. 044901.

[41] A.L. Moore and L. Shi, “Emerging challenges and materials for thermal management of electronics,” *Materials Today*, vol. 17, 2014, pp. 163–174.[42] B. Smith, B. Vermeersch, J. Carrete, E. Ou, J. Kim, N. Mingo, D. Akinwande, and L. Shi, “Temperature and Thickness Dependences of the Anisotropic In-Plane Thermal Conductivity of Black Phosphorus,” *Advanced Materials*, vol. 29, Feb. 2017, p. 1603756.

[43] J.M. Ziman, *Electrons and phonons*, 2006.

[44] Q. Hao, G. Chen, and M.S. Jeng, “Frequency-dependent Monte Carlo simulations of phonon transport in two-dimensional porous silicon with aligned pores,” *Journal of Applied Physics*, vol. 106, 2009.

[45] J. Randrianalisoa and D. Baillis, “Monte Carlo simulation of cross-plane thermal conductivity of nanostructured porous silicon films,” *Journal of Applied Physics*, vol. 103, 2008, p. 053502.

[46] P.E. Hopkins, L.M. Phinney, P.T. Rakich, R.H. Olsson, and I. El-Kady, “Phonon considerations in the reduction of thermal conductivity in phononic crystals,” *Applied Physics A*, vol. 103, Dec. 2010, pp. 575–579.

[47] E. Dechaumphai and R. Chen, “Thermal transport in phononic crystals: The role of zone folding effect,” *Journal of Applied Physics*, vol. 111, 2012, p. 073508.

[48] G.H. Tang, C. Bi, and B. Fu, “Thermal conduction in nano-porous silicon thin film,” *Journal of Applied Physics*, vol. 114, 2013, p. 184302.

[49] A. Jain, Y.J. Yu, and A.J.H. McGaughey, “Phonon transport in periodic silicon nanoporous films with feature sizes greater than 100 nm,” *Physical Review B - Condensed Matter and Materials Physics*, vol. 87, 2013, pp. 1–8.

[50] S. Mazumder and A. Majumdar, “Monte Carlo Study of Phonon Transport in Solid Thin Films Including Dispersion and Polarization,” *Journal of Heat Transfer*, vol. 123, 2001, pp. 749–759.

[51] A. Mittal and S. Mazumder, “Monte Carlo Study of Phonon Heat Conduction in Silicon Thin Films Including Contributions of Optical Phonons,” *Journal of Heat Transfer*, vol. 132, 2010, p. 052402.

[52] K. Kukita, I.N. Adisusilo, and Y. Kamakura, “Monte Carlo simulation of thermal conduction in silicon nanowires including realistic phonon dispersion relation,” *Japanese Journal of Applied Physics*, vol. 53, Jan. 2014, p. 015001.

[53] X. Zianni, V. Jean, K. Termentzidis, and D. Lacroix, “Scaling behavior of the thermal conductivity of width-modulated nanowires and nanofilms for heat transfer control at the nanoscale.,” *Nanotechnology*, vol. 25, 2014, p. 465402.

[54] Y. Chen, D. Li, J.R. Lukes, and A. Majumdar, “Monte Carlo Simulation of Silicon Nanowire Thermal Conductivity,” *Journal of Heat Transfer*, vol. 127, 2005, pp. 1129–1137.

[55] N.K. Ravichandran and A.J. Minnich, “Coherent and incoherent thermal transport in nanomeshes,” *Physical Review B*, vol. 89, May. 2014, p. 205432.

[56] B. Fu, C. Bi, and G.H. Tang, “Study of Thermal Conductivity in Nanoporous Thin Film and Nanocomposites,” 2014, pp. 1–12.

[57] A. Akkerman and M. Murat, “Electron–phonon interactions in silicon: Mean free paths, related distributions and transport characteristics,” *Nuclear Instruments and Methods in Physics Research Section B: Beam Interactions with Materials and Atoms*, vol. 350, 2015, pp. 49–54.

[58] K.T. Regner, A. J.H. McGaughey, and J. A. Malen, “Analytical interpretation of nondiffusive phonon transport in thermoreflectance thermal conductivity measurements,” *Physical Review B*, vol. 90, 2014, p. 064302.

[59] C. Dames, “Thermal materials: Pulling together to control heat flow.,” *Nature nanotechnology*, vol. 7, Feb. 2012, pp. 82–3.

[60] J.-P.M. Péraud and N.G. Hadjiconstantinou, “Efficient simulation of multidimensional phonon transport using energy-based variance-reduced Monte Carlo formulations,” *Physical Review B*, vol. 84, Nov. 2011, p. 205331.

[61] J.-P.M. Péraud and N.G. Hadjiconstantinou, “An alternative approach to efficient simulation of micro/nanoscale phonon transport,” *Applied Physics Letters*, vol. 101, 2012, p. 153114.

[62] K. Kukita and Y. Kamakura, “Monte Carlo simulation of phonon transport in silicon including a realistic dispersion relation,” *Journal of Applied Physics*, vol. 114, 2013, p. 154312.

[63] G. Chen, D. Borca-Tasciuc, and R.G. Yang, “Nanoscale Heat Transfer,” *Encyclopedia of Nanoscience and Nanotechnology*, vol. 7, 2004, pp. 429–459.

[64] X. Zianni and P. Chantrenne, “Thermal conductivity of diameter-modulated silicon nanowires within a frequency-dependent model for phonon boundary scattering,” *Journal of Electronic Materials*, vol. 42, Oct. 2012, pp. 1509–1513

[65] V. Jean, S. Fumeron, K. Termentzidis, X. Zianni, and D. Lacroix, “Monte Carlo simulations of phonon transport in Si nanowires with constrictions,” *International Journal of Heat and Mass Transfer*, vol. 86, 2015, pp. 648–655.

[66] A.J. Minnich, “Exploring electron and phonon transport at the nanoscale for thermoelectric energy conversion,” 2011.

[67] H.R. Shanks, P.D. Maycock, P.H. Sidles, and G.C. Danielson, “Thermal Conductivity of Silicon from 300 to 1400°K,” *Physical Review*, vol. 130, Jun. 1963, pp. 1743–1748.

[68] C.J. Glassbrenner and G.A. Slack, “Thermal Conductivity of Silicon and Germanium from 3°K to the Melting Point,” *Physical Review*, vol. 134, May. 1964, pp. A1058–A1069.

[69] F. Marty, L. Rousseau, B. Saadany, B. Mercier, O. Français, Y. Mita, and T. Bourouina, “Advanced etching of silicon based on deep reactive ion etching for silicon high aspect ratio microstructures and three-dimensional micro- and nanostructures,” *Microelectronics Journal*, vol. 36, 2005, pp. 673–677.

[70] C. Vieu, F. Carcenac, A. Pepin, Y. Chen, M. Mejias, A. Lebib, L. Manin-Ferlazzo, L. Couraud, and H. Launois, “Electron beam lithography - Resolution limits and applications,” *Applied Surface Science*, vol. 164, 2000, pp. 111–117.

[71] G. Romano and A.M. Kolpak, “Thermal anisotropy enhanced by phonon size effects in nanoporous materials,” *Applied Physics Letters*, vol. 110, Feb. 2017, p. 093104.

[72] D.G. Cahill, W.K. Ford, K.E. Goodson, G.D. Mahan, A. Majumdar, H.J. Maris, R. Merlin, and S.R. Phillpot, “Nanoscale thermal transport,” *Journal of Applied Physics*, vol. 93, Jan. 2003, pp. 793–818.

[73] A.J. Minnich, M.S. Dresselhaus, Z.F. Ren, and G. Chen, “Bulk nanostructured thermoelectric materials: current research and future prospects,” *Energy & Environmental Science*, vol. 2, 2009, p. 466.

[74] D. Zhao, X. Qian, X. Gu, S.A. Jajja, and R. Yang, “Measurement Techniques for Thermal Conductivity and Interfacial Thermal Conductance of Bulk and Thin Film Materials,” *Journal of Electronic Packaging*, vol. 138, Oct. 2016, p. 040802.

[75] L. Zeng, K.C. Collins, Y. Hu, M.N. Luckyanova, A.A. Maznev, S. Huberman, V. Chiloyan, J. Zhou, X. Huang, K.A. Nelson, and G. Chen, “Measuring Phonon Mean Free Path Distributions by Probing Quasiballistic Phonon Transport in Grating Nanostructures,” *Scientific Reports*, vol. 5, Dec. 2015, p. 17131.

[76] A.J. Minnich, J.A. Johnson, A.J. Schmidt, K. Esfarjani, M.S. Dresselhaus, K.A. Nelson, and G. Chen, “Thermal Conductivity Spectroscopy Technique to Measure Phonon Mean Free Paths,” *Physical Review Letters*, vol. 107, Aug. 2011, p. 095901.

[77] Y. Hu, L. Zeng, A.J. Minnich, M.S. Dresselhaus, and G. Chen, “Spectral mapping of thermal conductivity through nanoscale ballistic transport,” *Nature Nanotechnology*, vol. 10, Aug. 2015, pp. 701–706.

[78] Y.S. Ju and K.E. Goodson, “Phonon scattering in silicon films with thickness of order 100 nm,” *Applied Physics Letters*, vol. 74, May. 1999, pp. 3005–3007.

[79] A.I. Hochbaum, R. Chen, R.D. Delgado, W. Liang, E.C. Garnett, M. Najarian, A. Majumdar, and P. Yang, “Enhanced thermoelectric performance of rough silicon nanowires,” *Nature*, vol. 451, Jan. 2008, pp. 163–167.

[80] A.I. Boukai, Y. Bunimovich, J. Tahir-Kheli, J.-K. Yu, W.A. Goddard III, and J.R. Heath, “Silicon nanowires as efficient thermoelectric materials,” *Nature*, vol. 451, Jan. 2008, pp. 168–171.

[81] D. Li, Y. Wu, P. Kim, L. Shi, P. Yang, and A. Majumdar, “Thermal conductivity of individual silicon nanowires,” *Applied Physics Letters*, vol. 83, Oct. 2003, pp. 2934–2936.

[82] R. Anufriev, A. Ramiere, J. Maire, and M. Nomura, “Heat guiding and focusing using ballistic phonon transport in phononic nanostructures,” *Nature Communications*, vol. 8, May. 2017, p. 15505.

[83] R. Yanagisawa, J. Maire, A. Ramiere, R. Anufriev, and M. Nomura, “Impact of limiting dimension on thermal conductivity of one-dimensional silicon phononic crystals,” *Applied Physics Letters*, vol. 110, Mar. 2017, p. 133108.

[84] J. Lee, W. Lee, G. Wehmeyer, S. Dhuey, D.L. Olynick, S. Cabrini, C. Dames, J.J. Urban, and P. Yang, “Investigation of phonon coherence and backscattering using silicon nanomeshes,” *Nature Communications*, vol. 8, Jan. 2017, p. 14054.

[85] G. Romano and J.C. Grossman, “Heat Conduction in Nanostructured Materials Predicted by Phonon Bulk Mean Free Path Distribution,” *Journal of Heat Transfer*, vol. 137, 2015, p. 071302.

[86] V. Jean, S. Fumeron, K. Termentzidis, S. Tutashkonko, and D. Lacroix, “Monte Carlo simulations of phonon transport in nanoporous silicon and germanium,” *Journal of Applied Physics*, vol. 115, Jan. 2014, p. 024304.

[87] T. Hori, J. Shiomi, and C. Dames, “Effective phonon mean free path in polycrystalline nanostructures,” *Applied Physics Letters*, vol. 106, Apr. 2015, p. 171901.

[88] R.B. Peterson, “Direct Simulation of Phonon-Mediated Heat Transfer in a Debye Crystal,” *Journal of Heat Transfer*, vol. 116, 1994, pp. 815–822.

[89] J.E. Turney, A. J.H. McGaughey, C.H. Amon, and D.P. Sellan, "Cross-plane phonon transport in thin films," *Journal of Applied Physics*, vol. 107, 2010, p. 113524.

[90] D. Lacroix, K. Joulain, and D. Lemonnier, "Monte Carlo transient phonon transport in silicon and germanium at nanoscales," *Physical Review B*, vol. 72, Aug. 2005, p. 064305.

[91] A.J.H. McGaughey and A. Jain, "Nanostructure thermal conductivity prediction by Monte Carlo sampling of phonon free paths," *Applied Physics Letters*, vol. 100, Feb. 2012, p. 061911.

[92] F. Yang and C. Dames, "Mean free path spectra as a tool to understand thermal conductivity in bulk and nanostructures," *Physical Review B*, vol. 87, Jan. 2013, p. 035437.

[93] A. Matthiessen and C. Vogt, "On the Influence of Temperature on the Electric Conducting-Power of Alloys," *Philosophical Transactions of the Royal Society of London*, vol. 154, Jan. 1864, pp. 167–200.

[94] K.D. Parrish, J.R. Abel, A. Jain, J.A. Malen, and A.J.H. McGaughey, "Phonon-boundary scattering in nanoporous silicon films: Comparison of Monte Carlo techniques," *Journal of Applied Physics*, vol. 122, Sep. 2017, p. 125101.

[95] J. Cuffe, E. Chávez, A. Shchepetov, P.-O. Chapuis, E.H. El Boudouti, F. Alzina, T. Kehoe, J. Gomis-Bresco, D. Dudek, Y. Pennec, B. Djafari-Rouhani, M. Prunnila, J. Ahopelto, and C.M. Sotomayor Torres, "Phonons in Slow Motion: Dispersion Relations in Ultrathin Si Membranes," *Nano Letters*, vol. 12, Jul. 2012, pp. 3569–3573.

[96] E. Chávez-Ángel, J.S. Reparaz, J. Gomis-Bresco, M.R. Wagner, J. Cuffe, B. Graczykowski, A. Shchepetov, H. Jiang, M. Prunnila, J. Ahopelto, F. Alzina, and C.M. Sotomayor Torres, "Reduction of the thermal conductivity in free-standing silicon nano-membranes investigated by non-invasive Raman thermometry," *APL Materials*, vol. 2, Jan. 2014, p. 012113.

[97] K. Esfarjani, G. Chen, and H.T. Stokes, "Heat transport in silicon from first-principles calculations," *Physical Review B*, vol. 84, Aug. 2011, p. 085204.

[98] Y. Zeng and A. Marconnet, "Tuning the Anisotropy of In-Plane Thermal Conduction in Thin Films by Modulating Thickness," *Physical Review Applied*, vol. 9, Jan. 2018, p. 011001.

[99] R.G. Chambers, "The Conductivity of Thin Wires in a Magnetic Field," *Proceedings of the Royal Society A: Mathematical, Physical and Engineering Sciences*, vol. 202, Aug. 1950, pp. 378–394.

[100] G. Chen, *Nanoscale Energy Transport and Conversion: A Parallel Treatment of Electrons, Molecules, Phonons, and Photons*, 2005.

[101] G. Romano and A.M. Kolpak, "Directional Phonon Suppression Function as a Tool for the Identification of Ultralow Thermal Conductivity Materials," *Scientific Reports*, vol. 7, Mar. 2017, p. 44379.

[102] C. Hua and A.J. Minnich, "Semi-analytical solution to the frequency-dependent Boltzmann transport equation for cross-plane heat conduction in thin films," *Journal of Applied Physics*, vol. 117, May. 2015, p. 175306.

[103] A. Majumdar, "Microscale Heat Conduction in Dielectric Thin Films," *Journal of Heat Transfer*, vol. 115, 1993, p. 7.

[104] H.B.G. Casimir, "Note on the conduction of heat in crystals," *Physica*, vol. 5, Jan. 1938, pp. 495–500.

[105] Y. He, D. Donadio, J.-H. Lee, J.C. Grossman, and G. Galli, "Thermal transport in nanoporous silicon: interplay between disorder at mesoscopic and atomic scales.," *ACS nano*, vol. 5, 2011, pp. 1839–1844.

[106] G. Davies and C.M. Penchina, "The Effect of Uniaxial Stress on the GR1 Doublet in Diamond," *Proceedings of the Royal Society of London Series A*, vol. 338, 1974, pp. 359–374.

[107] K.C. Sood and M.K. Roy, "Phonon conductivity of doped germanium under uniaxial stress in the [110] direction," *Physical Review B*, vol. 46, 1992, pp. 7486–7495.

[108] T. Li, Z.Y. Huang, Z.C. Xi, S.P. Lacour, S. Wagner, and Z. Suo, "Delocalizing strain in a thin metal film on a polymer substrate," *Mechanics of Materials*, vol. 37, 2005, pp. 261–273.

[109] N. Lu, X. Wang, Z. Suo, and J. Vlassak, "Metal films on polymer substrates stretched beyond 50%," *Applied Physics Letters*, vol. 91, 2007, pp. 1–4.

[110] Y. Xiang, T. Li, Z. Suo, and J.J. Vlassak, "High ductility of a metal film adherent on a polymer substrate," *Applied Physics Letters*, vol. 87, 2005, pp. 1–3.

[111] S.P. Lacour, S. Wagner, Z. Huang, and Z. Suo, "Stretchable gold conductors on elastomeric substrates," *Applied Physics Letters*, vol. 82, Apr. 2003, pp. 2404–2406.

[112] Y.S. Ju, K. Kurabayashi, and K.E. Goodson, "Thermal characterization of anisotropic thin dielectric films using harmonic Joule heating," *Thin Solid Films*, vol. 339, 1999, pp. 160–164.

[113] K. Kurabayashi, M. Asheghi, M. Touzelbaev, and K.E. Goodson, "Measurement of the thermal conductivity anisotropy in polyimide films," *IEEE Journal of Microelectromechanical Systems*, vol. 8, 1999, pp. 180–191.

[114] K.S. Novoselov, A.K. Geim, S. V. Morozov, D. Jiang, Y. Zhang, S. V. Dubonos, I. V. Grigorieva, and A.A. Firsov, "Electric field effect in atomically thin carbon films.," *Science*, vol. 306, 2004, pp. 666–669.

[115] X. Li, W. Cai, J. An, S. Kim, J. Nah, D. Yang, R. Piner, A. Velamakanni, I. Jung, E. Tutuc, S.K. Banerjee, L. Colombo, and R.S. Ruoff, "Large-area synthesis of high-quality and uniform graphene films on copper foils.," *Science*, vol. 324, 2009, pp. 1312–1314.

[116] M. Losurdo, M.M. Giangregorio, P. Capezzuto, and G. Bruno, "Graphene CVD growth on copper and nickel: role of hydrogen in kinetics and structure," *Physical Chemistry Chemical Physics*, vol. 13, 2011, p. 20836.

[117] S. Choubak, P.L. Levesque, E. Gaufres, M. Biron, P. Desjardins, and R. Martel, "Graphene CVD: Interplay between growth and etching on morphology and stacking by hydrogen and oxidizing impurities," *Journal of Physical Chemistry C*, vol. 118, 2014, pp. 21532–21540.

[118] W. Jang, W. Bao, L. Jing, C.N. Lau, and C. Dames, "Thermal conductivity of suspended few-layer graphene by a modified T-bridge method," *Applied Physics Letters*, vol. 103, Sep. 2013, pp. 1–6.

[119] S. Ghosh, W. Bao, D.L. Nika, S. Subrina, E.P. Pokatilov, C.N. Lau, and A. A Balandin, "Dimensional crossover of thermal transport in few-layer graphene.," *Nature materials*, vol. 9, 2010, pp. 555–558.

[120] W. Jang, Z. Chen, W. Bao, C.N. Lau, and C. Dames, "Thickness-dependent thermal conductivity of encased graphene and ultrathin graphite," *Nano Letters*, vol. 10, 2010, pp. 3909–3913.

[121] J.H. Seol, A.L. Moore, L. Shi, I. Jo, and Z. Yao, "Thermal Conductivity Measurement of Graphene Exfoliated on Silicon Dioxide," *Journal of Heat Transfer*, vol. 133, 2011, p. 022403.

[122] B. Qiu and X. Ruan, "Reduction of spectral phonon relaxation times from suspended to supported graphene," *Applied Physics Letters*, vol. 100, 2012, p. 193101.

[123] W. Lee, K.D. Kihm, H.G. Kim, S. Shin, C. Lee, J.S. Park, S. Cheon, O.M. Kwon, G. Lim, and W. Lee, "In-Plane Thermal Conductivity of Polycrystalline Chemical Vapor Deposition Graphene with Controlled Grain Sizes," *Nano Letters*, vol. 17, 2017, pp. 2361–2366.

[124] Z.H. Ni, T. Yu, Y.H. Lu, Y.Y. Wang, Y.P. Feng, and Z.X. Shen, "Uniaxial Strain on Graphene : Raman," *ACS Nano*, vol. 2, 2008, pp. 2301–2305.

[125] M.I. Katsnelson and A.K. Geim, "Energy gaps and a zero-field quantum Hall effect in graphene by strain engineering," *Nature Physics*, vol. 6, 2009, pp. 30–33.

[126] S.-M. Choi, S.-H. Jhi, and Y.-W. Son, "Effects of Strain on Electronic Properties of Graphene," *Advanced Materials*, vol. 1, 2009, pp. 23–26.

[127] G. Gui, D. Morgan, J. Booske, J. Zhong, and Z. Ma, "Local strain effect on the band gap engineering of graphene by a first-principles study," *Applied Physics Letters*, vol. 106, 2015.

[128] N. Wei, L. Xu, H.-Q. Wang, and J.-C. Zheng, "Strain engineering of thermal conductivity in graphene sheets and nanoribbons: a demonstration of magic flexibility.," *Nanotechnology*, vol. 22, 2011, p. 105705.

[129] L.F.C. Pereira and D. Donadio, "Divergence of the thermal conductivity in uniaxially strained graphene," *Physical Review B - Condensed Matter and Materials Physics*, vol. 87, 2013, pp. 1–6.

[130] N. Bonini, J. Garg, and N. Marzari, "Acoustic phonon lifetimes and thermal transport in free-standing and strained graphene.," *Nano letters*, vol. 12, Jun. 2012, pp. 2673–8.

[131] Y. Kuang, L. Lindsay, and B. Huang, "Unusual Enhancement in Intrinsic Thermal Conductivity of Multilayer Graphene by Tensile Strains," *Nano Letters*, vol. 15, 2015, pp. 6121–6127.

[132] H. Lorenz, M. Despont, N. Fahrni, N. Labianca, P. Renaud, and P. Vettiger, "SU-8: a low-cost negative resist for MEMS," *J. Micromech. Microeng. J. Micromech. Microeng*, vol. 7, 1997, pp. 121–121.

[133] R. Feng and R.J. Farris, "Influence of processing conditions on the thermal and mechanical properties of SU8 negative photoresist coatings," *Journal of Micromechanics and Microengineering*, vol. 13, 2003, pp. 80–88.

[134] F.J. Blanco, M. Agirregabiria, J. Garcia, J. Berganzo, M. Tijero, M.T. Arroyo, J.M. Ruano, I. Aramburu, and K. Mayora, "Novel three-dimensional embedded SU-8 microchannels fabricated using a low temperature full wafer adhesive bonding," *Journal of Micromechanics and Microengineering*, vol. 14, 2004, pp. 1047–1056.

[135] C. Liu, "Recent developments in polymer MEMS," *Advanced Materials*, vol. 19, 2007, pp. 3783–3790.

[136] S.E. Zhu, R. Shabani, J. Rho, Y. Kim, B.H. Hong, J.H. Ahn, and H.J. Cho, "Graphene-based bimorph microactuators," *Nano Letters*, vol. 11, 2011, pp. 977–981.

[137] A.P.A. Raju, A. Lewis, B. Derby, R.J. Young, I.A. Kinloch, R. Zan, and K.S. Novoselov, "Wide-area strain sensors based upon graphene-polymer composite coatings probed by raman spectroscopy," *Advanced Functional Materials*, vol. 24, 2014, pp. 2865–2874.

[138] S. Lim, D. Son, J. Kim, Y.B. Lee, J.K. Song, S. Choi, D.J. Lee, J.H. Kim, M. Lee, T. Hyeon, and D.H. Kim, "Transparent and stretchable interactive human machine interface based on patterned graphene heterostructures," *Advanced Functional Materials*, vol. 25, 2015, pp. 375–383.

[139] R. Feng and R.J. Farris, "Characterization of the Thermal and Elastic Constants for a Negative Photoresist : SU8 Coating," *Journal of Materials Science*, vol. 7, 2002, pp. 423–424.

[140] M.T. Alam, R. A. Pulavarthy, C. Muratore, and M. A. Haque, "Mechanical Strain Dependence of Thermal Transport in Amorphous Silicon Thin Films," *Nanoscale and Microscale Thermophysical Engineering*, vol. 19, 2015, pp. 1–16.

[141] "SU-8 Permanent Photoresists SU-8 Permanent Photoresists," 2015, available at: http://www.microchem.com/pdf/SU-82000DataSheet2000_5thru2015Ver4.pdf.

[142] S. Chugh, R. Mehta, N. Lu, F.D. Dios, M.J. Kim, and Z. Chen, "Comparison of graphene growth on arbitrary non-catalytic substrates using low-temperature PECVD," *Carbon*, vol. 93, 2015, pp. 393–399.

[143] R. Mehta, S. Chugh, and Z. Chen, "Transfer-free multi-layer graphene as a diffusion barrier," *Nanoscale*, vol. 9, 2017, pp. 1827–1833.

[144] Microchem, "SU-8 2000 Permanent Epoxy Negative Photoresist," *Processing Guidelines*, 2015.

[145] A.D. McConnell and K.E. Goodson, *Thermal conduction in silicon micro-and nanostructures*, 2005.

[146] K.S. Novoselov, A.K. Geim, S. V. Morozov, Y.Z. D. Jiang, S. V. Dubonos, I. V. Grigorieva, and A.A. Firsov, "Electric Field Effect in Atomically Thin Carbon Films," Science, vol. 306, 2004, pp. 666–669.

[147] C. Lee, X. Wei, J.W. Kysar, and J. Hone, "Measurement of the Elastic Properties and Intrinsic Strength of Monolayer Graphene," *Science*, vol. 321, Jul. 2008, pp. 385–388.

[148] T. Georgiou, R. Jalil, B.D. Belle, L. Britnell, R. V. Gorbachev, S. V. Morozov, Y.-J. Kim, A. Gholinia, S.J. Haigh, O. Makarovsky, L. Eaves, L.A. Ponomarenko, A.K. Geim, K.S. Novoselov, and A. Mishchenko, "Vertical field-effect transistor based on graphene–WS2 heterostructures for flexible and transparent electronics," *Nature Nanotechnology*, vol. 8, Feb. 2013, pp. 100–103.

[149] A.A. Balandin, "Thermal properties of graphene and nanostructured carbon materials.," *Nat. Mater.*, vol. 10, Aug. 2011, p. 569.

[150] H.J. Yoon, D.H. Jun, J.H. Yang, Z. Zhou, S.S. Yang, and M.M.C. Cheng, "Carbon dioxide gas sensor using a graphene sheet," *Sensors and Actuators, B: Chemical*, vol. 157, 2011, pp. 310–313.

[151] W.S. Hummers and R.E. Offeman, "Preparation of Graphitic Oxide," *Journal of the American Chemical Society*, vol. 80, 1958, pp. 1339–1339.

[152] D.C. Marcano, D. V Kosynkin, J.M. Berlin, A. Sinitskii, Z. Sun, A. Slesarev, L.B. Alemany, W. Lu, and J.M. Tour, "Improved Synthesis of Graphene Oxide," *ACS Nano*, vol. 4, Aug. 2010, pp. 4806–4814.

[153] T. Schwamb, B.R. Burg, N.C. Schirmer, and D. Poulikakos, "An electrical method for the measurement of the thermal and electrical conductivity of reduced graphene oxide nanostructures," *Nanotechnology*, vol. 20, 2009.

[154] W. Yu, H. Xie, F. Li, J. Zhao, and Z. Zhang, "Significant thermal conductivity enhancement in graphene oxide papers modified with alkaline earth metal ions," *Applied Physics Letters*, vol. 103, 2013, pp. 1–5.

[155] B. Shen, W. Zhai, and W. Zheng, "Ultrathin flexible graphene film: An excellent thermal conducting material with efficient EMI shielding," *Advanced Functional Materials*, vol. 24, 2014, pp. 4542–4548.

[156] N.J. Song, C.M. Chen, C. Lu, Z. Liu, Q.Q. Kong, and R. Cai, "Thermally reduced graphene oxide films as flexible lateral heat spreaders," *Journal of Materials Chemistry A*, vol. 2, 2014, pp. 16563–16568.

[157] P. Kumar, F. Shahzad, S. Yu, S. Man, Y. Kim, and C. Min, "Large-area reduced graphene oxide thin film with excellent thermal conductivity and electromagnetic interference shielding effectiveness," *Carbon*, vol. 94, 2015, pp. 494–500.

[158] Y. Zhang, H. Han, N. Wang, P. Zhang, Y. Fu, M. Murugesan, M. Edwards, K. Jeppson, S. Volz, and J. Liu, "Improved Heat Spreading Performance of Functionalized Graphene in Microelectronic Device Application," *Advanced Functional Materials*, vol. 25, 2015, pp. 4430–4435.

[159] J.D. Renteria, S. Ramirez, H. Malekpour, B. Alonso, A. Centeno, A. Zurutuza, A.I. Cocemasov, D.L. Nika, and A.A. Balandin, "Strongly Anisotropic Thermal Conductivity of Free-Standing Reduced Graphene Oxide Films Annealed at High Temperature," *Advanced Functional Materials*, vol. 25, 2015, pp. 4664–4672.

[160] Y. Chen, K. Fu, S. Zhu, W. Luo, Y. Wang, Y. Li, E. Hitz, Y. Yao, J. Dai, J. Wan, V.A. Danner, T. Li, and L. Hu, "Reduced graphene oxide films with ultrahigh conductivity as Li-ion battery current collectors," *Nano Letters*, vol. 16, 2016, pp. 3616–3623.

[161] C. Teng, D. Xie, J. Wang, Z. Yang, G. Ren, and Y. Zhu, "Ultrahigh Conductive Graphene Paper Based on Ball-Milling Exfoliated Graphene," *Advanced Functional Materials*, vol. 27, 2017, pp. 1–7.

[162] J. Ding, O. Ur Rahman, H. Zhao, W. Peng, H. Dou, H. Chen, and H. Yu, "Hydroxylated graphene-based flexible carbon film with ultrahigh electrical and thermal conductivity," *Nanotechnology*, vol. 28, 2017.

[163] Y. Huang, Q. Gong, Q. Zhang, Y. Shao, J. Wang, Y. Jiang, M. Zhao, D. Zhuang, and J. Liang, "Fabrication and molecular dynamics analyses of highly thermal conductive reduced graphene oxide films at ultra-high temperatures," *Nanoscale*, vol. 9, 2017, pp. 2340–2347.

[164] L. Peng, Z. Xu, Z. Liu, Y. Guo, P. Li, and C. Gao, "Ultrahigh Thermal Conductive yet Superflexible Graphene Films," *Advanced Materials*, vol. 29, 2017, pp. 1–8.

[165] T. Li, A.D. Pickel, Y. Yao, Y. Chen, Y. Zeng, S.D. Lacey, Y. Li, Y. Wang, J. Dai, Y. Wang, B. Yang, M.S. Fuhrer, A. Marconnet, C. Dames, D.H. Drew, and L. Hu, "Thermoelectric properties and performance of flexible reduced graphene oxide films up to 3,000 K," *Nature Energy*, vol. 3, 2018, pp. 148–156.

[166] S. Sahoo, S. Barik, G. Sharma, and G. Khurana, "Reduced graphene oxide as ultra fast temperature sensor," 2012.

[167] P. Sehrawat, Abid, S.S. Islam, and P. Mishra, "Reduced graphene oxide based temperature sensor: Extraordinary performance governed by lattice dynamics assisted carrier transport," *Sensors and Actuators, B: Chemical*, vol. 258, 2018, pp. 424–435.

[168] K.K. Sadasivuni, A. Kafy, H.C. Kim, H.U. Ko, S. Mun, and J. Kim, "Reduced graphene oxide filled cellulose films for flexible temperature sensor application," *Synthetic Metals*, vol. 206, 2015, pp. 154–161.

[169] J. Liu, W. Qu, Y. Xie, B. Zhu, T. Wang, X. Bai, and X. Wang, "Thermal conductivity and annealing effect on structure of lignin-based microscale carbon fibers," *Carbon*, vol. 121, 2017, pp. 35–47.

[170] Y. Guo, C. Dun, J. Xu, J. Mu, P. Li, L. Gu, C. Hou, C.A. Hewitt, Q. Zhang, Y. Li, D.L. Carroll, and H. Wang, "Ultrathin, Washable, and Large-Area Graphene Papers for Personal Thermal Management," *Small*, vol. 13, 2017, pp. 1–9.

[171] W.J. Parker, R.J. Jenkins, C.P. Butler, and G.L. Abbott, "Flash method of determining thermal diffusivity, heat capacity, and thermal conductivity," *Journal of Applied Physics*, vol. 32, 1961, pp. 1679–1684.

[172] T. Azumi and Y. Takahashi, "Novel finite pulse-width correction in flash thermal diffusivity measurement," *Review of Scientific Instruments*, vol. 52, 1981, pp. 1411–1413.

[173] T. Baba and A. Ono, "Improvement of the laser flash method to reduced uncertainty in thermal diffusivity measurements," *Meas. Sci. Technol.*, vol. 12, 2001, pp. 2046–2057.

[174] M.E. Hill, W. Post, and S. Writer, *The Flash Method*.

[175] W. Bao, A.D. Pickel, Q. Zhang, Y. Chen, Y. Yao, J. Wan, K. Fu, Y. Wang, J. Dai, H. Zhu, D. Drew, M. Fuhrer, C. Dames, and L. Hu, "Flexible, High Temperature, Planar Lighting with Large Scale Printable Nanocarbon Paper," *Advanced Materials*, 2016, pp. 4684–4691.

[176] P. Liu, Z. Fan, A. Mikhalchan, T.Q. Tran, D. Jewell, H.M. Duong, and A.M. Marconnet, "Continuous Carbon Nanotube-Based Fibers and Films for Applications Requiring Enhanced Heat Dissipation," *ACS Applied Materials and Interfaces*, vol. 8, 2016, pp. 17461–17471.

[177] H.-J. Kim, D. Kim, S. Jung, S.N. Yi, Y.J. Yun, S.K. Chang, and D.H. Ha, "Charge Transport in Thick Reduced Graphene Oxide Film," *The Journal of Physical Chemistry C*, vol. 119, 2015, pp. 28685–28690.

[178] S. Mei, L.N. Maurer, Z. Aksamija, and I. Knezevic, "Full-dispersion Monte Carlo simulation of phonon transport in micron-sized graphene nanoribbons," *Journal of Applied Physics*, vol. 116, 2014.

[179] Z. Aksamija and I. Knezevic, "Lattice thermal conductivity of graphene nanoribbons: Anisotropy and edge roughness scattering," *Applied Physics Letters*, vol. 98, 2011, pp. 2009–2012.

VITA

Yuqiang Zeng received his B.S. degree in July 2013 from the School of Energy and Power Engineering at Huazhong University of Science and Technology (HUST) in Wuhan, Hubei, China. His undergraduate research focused on numerical studies of crystal purification processes. In August 2013, he joined in the Marconnet Thermal and Energy Conversion Laboratory directed by Prof. Amy Marconnet as a M.S. student. Then, he decided to pursue a direct Ph.D. starting from August 2014. He expects to be granted his Ph.D. in Mechanical Engineering in August 2018.